ELECTRONIC MODIFICATION OF PLATINUM AND PALLADIUM ALLOY CATALYSTS AND THE CONSEQUENCES FOR DEHYDROGENATION SELECTIVITY

by

Stephen Campbell Purdy

A Dissertation

Submitted to the Faculty of Purdue University

In Partial Fulfillment of the Requirements for the degree of

Doctor of Philosophy

Davidson School of Chemical Engineering

West Lafayette, Indiana

May 2019

THE PURDUE UNIVERSITY GRADUATE SCHOOL
STATEMENT OF COMMITTEE APPROVAL

Dr. Jeffrey T. Miller, Chair
Department of Chemical Engineering
Dr. Jeff Greeley
Department of Chemical Engineering
Dr. Michel Harris
Department of Chemical Engineering
Dr. Christina Li
Department of Chemistry
Dr. A. Jeremy Kropf
Chemical Sciences and Engineering Division, Argonne National Laboratory

Approved by:

Dr. John Morgan
Head of the Graduate Program

For my family

ACKNOWLEDGMENTS

First and foremost, I would like to thank my advisor, Jeff Miller, for his guidance and wisdom throughout my PhD. In addition to the technical knowledge he imparted to me, Jeff taught me to never lose sight of the big picture, scientifically and in life. Jeff allowed me a great deal of autonomy in research, and I feel this was responsible for helping me learn one of the most important skills good scientists need: deciding which problems are worth taking the time to answer. I will fondly remember our afternoon-long conversations which inevitably ended up as debates about electronic structure in transition metals.

I also want to thank my committee members for their valuable input into the projects I have worked on: Jeff Greeley, Christina Li, Michael Harris, and Jeremy Kropf, each of whom added an important perspective to the work that I have done and pushed me to grow into a better researcher. I would also like to thank Jeremy Kropf for his help at the advanced photon source and for building the RIXS spectrometer, which enabled much of the work in this thesis.

I would also like to thank those who I have had the privilege to work with in my time at Purdue. Claire Nimlos, David Harvey, Daniel Wilcox, Jeremiah Vue and others without whom I probably wouldn't have made it through the first semester coursework. My DFT buddies, Pushkar Ghanekar, Ranga Seemakurthi, and Brandon Bukowski, all of whom contributed the DFT calculations in this thesis. Without their contributions each study I did would have been much less impactful and interesting. I would like to thank Garrett Mitchell who took all the beautiful STEM images for me, and for being such a great friend and confidant. Similarly, Juan-Carlo Vila Vega who collected the IR spectra on the palladium alloys. I would also like to thank all the Miller group members: Evan Wegener, Zhenwei Wu, Guanghui Zhang, Ce Yang, Laryssa Cesar, Nicole Libretto, Johnny Zhuchen, and Seulgi Choi. It was a pleasure to work with you and I am excited to see what great things you all end up doing.

I would like to thank my parents who always fostered my sense of curiosity and instilled within me the mantra that I can do hard things. Lastly, I would like to thank my wife and son, who are my raison d'être. Science is fun, but family is important; you have been with me through the triumphs and failures, week long APS trips, and all the other hardships of being a graduate student family. I couldn't have done it without you.

TABLE OF CONTENTS

LIST OF TABLES 8
LIST OF FIGURES 10
ABSTRACT 14
1. INTRODUCTION 16
1.1 Industrial Importance of Light Olefins 16
1.2 Dehydrogenation and Hydrogenolysis 17
1.3 Improving Selectivity in Dehydrogenation Catalysts 20
2. THE ORIGIN OF ELECTRONIC MODIFICATION OF PLATINUM IN A PT_3V ALLOY AND THEIR CONSEQUENCES FOR PROPANE DEHYDROGENATION CATALYSIS 24
2.1 Abstract 24
2.2 Introduction 24
2.3 Experimental 28
2.3.1 Catalyst Synthesis 28
2.3.2 Electron Microscopy 30
2.3.3 Propane Dehydrogenation 30
2.3.4 X-Ray Absorption Spectroscopy 31
2.3.5 Resonant Inelastic X-Ray Scattering 33
2.3.6 X-Ray Photoelectron Spectroscopy 33
2.3.7 X-Ray Diffraction 34
2.3.8 Density Functional Theory 34
2.4 Results 36
2.4.1 Structural Characterization 36
2.4.2 Electron Characterization 47
2.4.3 Propane Dehydrogenation 50
2.4.4 DFT 53
2.5 Discussion 59
2.5.1 Structural Model 59
2.5.2 Nature of Electronic Modification 62
2.5.3 The effect of Structure on Catalytic Performance 67

2.6 Conclusion 69
2.7 Acknowledgemnets 70
3. TESTING THE PREDICTIVE POWER OF A DEHYDROGENATION SELECTIVITY DESCRIPTOR IN PALLADIUM ALLOYS CATALYSTS WITH DIFFERENT STRUCTURES AND PROMOTERS 71
3.1 Abstract 71
3.2 Introduction 71
3.3 Methods 74
3.3.1 Catalyst Synthesis 74
3.3.2 In-situ Synchrotron X-ray Diffraction (XRD) 76
3.3.3 In-situ X-ray Adsorption Spectroscopy (XAS) 77
3.3.4 Propane Dehydrogenation 78
3.3.5 STEM/EDS 79
3.3.6 DFT 80
3.4 Results 80
3.4.1 Structural Characterization 80
3.4.2 Propane Dehydrogenation 90
3.4.3 Electronic Characterization 93
3.4.4 Density Functional Theory 94
3.5 Discussion 100
3.5.1 Catalyst structure 100
3.6 Conclusion 104
3.7 Acknowledgments 105
4. INSIGHT INTO ELECTRONIC STRUCTURE OF PLATINUM ALLOYS BY RESONANT INELASTIC X-RAY SCATTERING 106
4.1 Introduction 106
4.2 Experimental 108
4.2.1 Catalyst Synthesis 108
4.2.2 Scanning Transmission Electron Microscopy (STEM) 108
4.2.3 In-Situ X-ray Absorption Spectroscopy 108
4.2.4 In-Situ Synchrotron X-ray Diffraction 109

4.2.5 Resonant Inelastic X-Ray Scattering 110
4.2.6 X-Ray Photoelectron Spectroscopy 110
4.3 Results 111
4.3.1 Characterization of Pt-Ga 111
4.3.2 Resonant Inelastic X-ray Scattering 115
4.4 Discussion 119
4.5 Conclusion 121
5. SUMMARY 123
REFERENCES 125
PUBLICATIONS 138

LIST OF TABLES

Table 1: Synthesis parameters for Pt and Pt-V catalysts 29

Table 2: XANES edge energies and EXAFS fitting parameters for 3Pt, 5Pt-5V and 2Pt-5V: coordination number (CN), bond distance (R), Debye-Waller factor (σ2), and E0 correction (E0) 39

Table 3: Average Pt-Pt and Pt-V coordination numbers and bond distances for Pt-V catalysts. . 40

Table 4: EXAFS fits and XANES edge energies for Pt-V catalysts..... 40

Table 5: EXAFS fit of 5Pt-5V after reduction at 200°C..... 42

Table 6: First shell EXAFS fits and XANES edge energies of 5Pt-5V catalysts calcined at different temperatures. 45

Table 7: Fits of the 220 reflection for 3Pt and 5Pt-5V catalysts calcined at different temperatures 47

Table 8: Pt 4f XPS fitting parameters for 3Pt and 2Pt-5V..... 48

Table 9: EXAFS fit for Pt-V difference spectra 53

Table 10: Binding energies of CO and CH_3 on Pt (111), Pt_3V-1ML, Pt_3V-2ML and Pt_3V (111). Binding energies were calculated according to equation 3 and 4. 55

Table 11: Most stable binding configurations and their corresponding binding energies for CO, C_1, C_2, and C_3 hydrocarbon fragments adsorbed on Pt (111) and Pt_3V (111) surfaces. ... 57

Table 12: H binding energy on Pt (111) and Pt3V (111) references to H2 gas. 57

Table 13: Binding energies of CO and CHx species calculated on Pt_3V (111) and Pt (111) with the lattice constant of Pt_3V. The effect of changing the lattice constant of Pt (111) is minimal on the binding energy compared to the Pt slab constructed using the equilibrium lattice constant. 58

Table 14: Work function values for the (111) face of Pt and Pt3V. 65

Table 15: Number average particle size for Pd and bimetallic catalysts 82

Table 16: EXAFS fitting parameters for Pd foil, Pd, Pd-Mn, Pd-Ga and Pd-Zn..... 84

Table 17: Reduction-Oxidation difference EXAFS fit of 1Pd-5Mn..... 86

Table 18: Pd K edge EXAFS fits of Pd and Pd alloy catalysts after room temperature air exposure 92

Table 19: Dehydrogenation rate, first order deactivation rate constants and activity loss after 90 minutes of reaction for Pd and Pd alloy catalysts 93

Table 20: Most stable binding site and binding energy (relative to gas phase propylene) for Pd and 5 Pd alloy surfaces. 95

Table 21: Most stable H binding site and corresponding binding energy (relative to gas phase H_2) for Pd and Pd alloy surfaces..... 96

Table 22: Most stable ethylidyne binding sites and binding energies for ethylidyne..... 97

Table 23: Propylene dehydrogenation activation energy barrier and calculated dehydrogenation selectivity descriptor for Pd and Pd alloys..... 98

Table 24: thermodynamic and activation energy barriers for C-C bond cleavage of propyne on Pd and Pd alloy surfaces 98

Table 25: First and second moments of the Pd d band pDOS for surface Pd atoms in monometallic Pd and Pd alloys..... 99

Table 26: Pt L3 edge EXAFS fits of Pt and Pt-Ga. 113

Table 27: Energy transfer maximum values and Pt L3 edge XANES edge energy values for Pt and Pt alloy phases..... 118

Table 28: Pt 4f7/2 fit details and calculated Pt 4f7/2 core level shifts for Pt and Pt alloys after a reduction pretreatment at 550°C in 5% H2..... 118

LIST OF FIGURES

Figure 1: Equilibrium propane dehydrogenation conversion as a function of temperature for (left) increasing propane concentration and (right) fixed propane concentration and increasing hydrogen concentration. 17

Figure 2: schematic representation of the reverse Horiuti-Polanyi mechanism of propane dehydrogenation on a Pt surface. 18

Figure 3: Schematic of the hydrogenolysis mechanism, here depicted as occurring through surface bonded propyne. 19

Figure 4: Schematic of the close packed (111) surface of a substitutional solid solution bimetallic (left) and (right) an AB3 intermetallic compound with the AuCu3 prototype phase. Arrangement of the blue impurity atoms is random in the solid solution, and periodic in the intermetallic compound. 21

Figure 5: Volume average particle size distributions and representative STEM images for 3Pt (a,b), 5Pt-5V (c,d), 2Pt-5V (e,f) 36

Figure 6: Pt-V catalyst characterization by electron microscopy. a) HAADF STEM image of 2Pt-5V. b) EDS map of 2Pt-5V with Pt in blue and V in yellow. c) EDS line scan of green boxed area in b, with Pt in blue and V in Red. 37

Figure 7: V K edge EXAFS of 5Pt-5V after reduction at 550°C in 3.5% H2. 38

Figure 8: in-situ EXAFS magnitude (solid lines) and imaginary (dashed lines) of 3Pt (Black) and 2Pt-5V (blue) catalysts. Spectra were collected at room temperature in He after a 30-minute reduction at 550°C in 3.5% H2 38

Figure 9: R space EXAFS magnitude (solid black) and imaginary (dashed black) components of 5Pt-5V reduced at 200°C in 3.5% H2. 42

Figure 10: In-Situ synchrotron XRD patterns of a) 3Pt (black), 5Pt-5V (red). Fundamental FCC lines are labeled in black, and the first five superlattice lines of Pt_3V are labeled in red. b) Expanded view of the 220 and 311 reflection for the above samples with vertical dashed lines denoting experimental peak positions. All experimental spectra were collected at 35°C in 3.5% H2 after reduction at 550°C. Simulated patterns of Pt with a lattice parameter of 3.89 Å (grey) and Pt_3V with a lattice parameter of 3.87 Å (crimson) are also shown. c) Multi component fits of the 220 XRD reflection for 5Pt-5V catalysts calcined at 250°C, 450°C, 500°C, and 600°C. Raw data is shown in black, component fits in red (Pt) and green (Pt_3V) and total fit (Pt+Pt_3V) in blue. Component fits have been offset for clarity. Spectra were collected at 35°C in 3.5% H2 after reduction in the same atmosphere at 550°C. 43

Figure 11: In-Situ Pt L3 edge EXAFS of Pt foil (black) and 5Pt-5V catalysts calcined at 600°C (magenta), 550°C (blue), 450°C (green), and 250°C (red). Scans were taken at room temperature in He after reduction at 550°C in 3.5% H2. 45

Figure 12: a) In-situ Pt L3 edge XANES of 3Pt (Black) and 2Pt-5V (blue). Spectra were collected at room temperature in He after reduction at 550°C in 3.5% H2 for 30 minutes and a subsequent purge in He at 550°C. b) High resolution Pt 4f XPS spectra of 2Pt-5V and 3Pt after a reduction treatment in 5% H2 at 550°C for 30 minutes. Black Circles: Raw data, black line: Shirley background, Red lines: component fits, Blue line: total fit. Background and components are offset for clarity. The vertical line denotes the peak position of the Pt 4f7/2 component of 3Pt and 2Pt-5V. 47

Figure 13: Pt L3-Lβ5 RIXS maps of Pt (left) and Pt3V (right). Spectra were collected after a reduction treatment at 550°C in 3.5% H2 for 30 minutes. Spectra were collected at 100°C in 3.5% H2. Horizontal dashed lines denote the maximum of the inelastic scattering peak for each sample. 49

Figure 14: Propylene selectivity and propane conversion for 3Pt (black squares), 5Pt-5V (red circles), and 2Pt-5V (blue triangles) tested without (a) and with (b) cofed H_2. Reactions were performed at 550°C at 3 PSIG with 2.5% propane balance N_2. For plot (b) the hydrogen concentration was 2.5%. Data points shown are at zero deactivation with each data point representing a separate test. 50

Figure 15: Pt EXAFS difference spectra for 2Pt-5V (a) and 5Pt-5V (b) (magnitude: solid black, imaginary: dashed black) and difference spectra fit (magnitude fit: solid blue, imaginary fit: dashed blue). A reduced scan of both 2Pt-5V and 5Pt-5V was taken at room temperature in He after reduction at 550°C in 3.5% H2, subsequently the samples were exposed to air for 30 minutes and then scanned again. 52

Figure 16: Binary compositional phase diagram for Pt-V. Red nodes are stable phases lying on convex hull. Blue nodes are the most stable phases for given Pt-V compositions which do not lie on the convex hull. 53

Figure 17: a) pDOS for Pt (gold), Pt_3V (burgundy) and two epitaxial Pt_3V on Pt structures with one (orange) and two (crimson) layers of Pt_3V on Pt with the Fermi energy marked by a vertical dashed line. The inset graph shows an expanded view of near-Fermi energy unfilled states. b) structures corresponding to each model. c) d-band center and d-band width for above structures. 54

Figure 18: Schematics of binding configurations and their corresponding binding energies (with respect to Pt (111)) for CO, C_1, C_2 and C_3 hydrocarbon fragments on Pt_3V (111) and Pt (111) surfaces. 56

Figure 19: Calculated C-H bond breaking energy for adsorbed propylene on Pt (111) (solid black) and Pt_3V (111) (solid red) referenced to gas phase propylene (dashed black). 58

Figure 20: Pt L_3 edge XANES shift (vs. Pt foil) plotted against the ratio of Pt-V to Pt-Pt coordination numbers for 3Pt and 10 Pt-V catalysts. The Pt-V to Pt-Pt ratio for the bulk Pt_3V phase is shown as a vertical dashed line. A linear fit of the data is shown in red.... 62

Figure 21: X-Y averaged electrostatic potential for Pt(111) and Pt3V (111) slab plotted along the Z-axis (perpendicular to the slab surface)..... 65

Figure 22: STEM images of Pd and bimetallic Pd catalysts: (a) 1Pd (b) 2Pd (c) STEM image of 1Pd-5Mn with overlaid EDX maps for Pd (red) and Ga (Green). (d) STEM image of 2.5Pd-2.5Ga with overlaid EDX maps for Pd (purple) and Ga (yellow)..... 81

Figure 23: R space Pd K edge EXAFS magnitude (solid lines) and imaginary (dashed) components of Pd catalysts. a) monometallic Pd catalysts: Pd foil (black) 2Pd (grey) and 1Pd (light grey) b) 2Pd-3Zn (orange) and 1Pd (black) c) 2.5Pd-2.5Ga (green) and 1Pd (black) and d) 1Pd-5Mn (magenta) and 1Pd (black). Spectra were collected at room temperature in He after reduction at 550°C in 3.5% H2..... 83

Figure 24: Reduction-Oxidation difference EXAFS of 1Pd-5Mn with the experimental difference magnitude (solid) and imaginary (dashed) shown in black and the difference fit shown in blue..... 86

Figure 25: (a) In-Situ synchrotron XRD pattern for 2.5Pd-2.5Ga (green) after a reduction treatment at 550°C in 3.5% H2 with simulated Pd_2Ga pattern (black) and (b) Simulated bulk patterns for Pd-Ga intermetallic compounds 87

Figure 26: Simulated Pd_2Ga XRD patterns with different crystallite sizes (black, grey, purple, blue, light blue) compared with experimentally measured Pd-Ga catalyst (pink)..... 88

Figure 27: (left) simulations of bulk PdZn phases and (right) experimental in-situ synchrotron XRD pattern for the Pd-Zn catalyst (orange) along with simulated pattern for the β1-PdZn phase..... 89

Figure 28: Initial propylene conversion for 2Pd-3Zn (blue circles), 2Pd-3In (purple triangles), 2.5Pd-2.5Ga (green diamonds), 1Pd-5Mn (magenta inverted triangles), 2Pd-3Fe (orange hexagons), 1Pd (open black squares), and 2Pd (filled black squares) plotted against the initial propane conversion. Tests were performed at 550°C in 2.5% H2 and 2.5% propane after pre-reducing in 550°C in 5% H2 90

Figure 29: Normalized propane conversion vs. time on stream for 1Pd (unfilled black squares), 2Pd (filled black squares), 2Pd-3Zn(blue), 3Pd-3In (purple), 2.5Pd-2.5Ga (green), 1Pd-5Mn (magenta), and 2Pd-3Fe (orange). Tests were run at 550C, 3 PSIG, with 2.5% propane and 2.5 H_2..... 91

Figure 30: XANES of 1Pd (black), 2Pd-3Zn (orange), 2.5Pd-2.5Ga (green) and 1Pd-5Mn (magenta) at the K edge (a) and L_3 edge (b) after reduction at 550°C in 3.5% H2..... 93

Figure 31: Structural model of Pd and Pd alloy catalysts. The PdIn and PdMn catalysts have alloy shells with a Pd core while the PdZn, PdGa and PdFe catalysts are pure phases. The

unit cell of each alloy structure and the lowest energy surface are pictured beneath the respective nanoparticle models. 100

Figure 32: STEM image (left) and number average particle size distribution (right) of 5Pt-2.5Ga. 111

Figure 33: XANES and EXAFS results for Pt and Pt-Ga catalysts. (a) Pt L3 edge XANES for a 3Pt (black) 5Pt-2.5Ga (red) and Pt foil (blue). (b) EXAFS of 3Pt (black) and 5Pt-2.5Ga (red). R space EXAFS fits of 5Pt-2.5Ga (c) and 3Pt. 112

Figure 34: In-situ Synchrotron XRD pattern of 5Pt-2.5Ga (red) and Pt3Ga standard simulation with a lattice parameter of 3.89 Å. Superlattice diffraction peaks are labeled in black and primary reflections are labeled in red. 114

Figure 35: RIXS plots of Pt and Pt alloy catalysts after reduction at 550°C in 3.5% H2..... 116

ABSTRACT

Author: Purdy, Stephen, C. PhD
Institution: Purdue University
Degree Received: May 2019
Title: Electronic Modification of Platinum and Palladium Alloy Catalysts and the Consequences for Dehydrogenation Selectivity
Committee Chair: Jeffrey Miller

Dehydrogenation is the catalytic process of removing hydrogen from a saturated hydrocarbon to produce an olefin. Olefins are important feedstocks for the petrochemical industry and can potentially be used to produce fuels through oligomerization. Alloys containing an active metal such as platinum and palladium and a non-catalytic metal offer improved selectivity towards the olefin. This body of work seeks to further the understanding of how heteroatomic bonds in alloys change the rate and selectivity of alloy catalysts used for dehydrogenation.

In the first study, a series of Pt-V bimetallic catalysts are synthesized, which are highly selective propane dehydrogenation catalysts. The bimetallic nature of the nanoparticles was verified by in-situ X-ray Absorption Spectroscopy (XAS) and the formation of the Pt_3V alloy phase was shown by in-situ synchrotron X-ray Diffraction (XRD). A reduction-oxidation difference XAS method was used to examine the surface stoichiometry and found that a shell layer of the alloy phase forms when the particles are platinum rich. Electronic modification of Pt was studied by Pt L_3 edge X-ray Absorption Near Edge Structure (XANES), X-ray Photoelectron Spectroscopy (XPS), Resonant Inelastic X-ray Scattering (RIXS) and Density Functional Theory (DFT). The spectral changes observed were shown to be due to changes in the energy of the filled and unfilled 5d density of states, and not due to electron transfer. The electronic modifications cause a weakening of adsorbate binding and destabilization of deeply dehydrogenated hydrocarbons, which contributes to the dehydrogenation selectivity.

In the second study, alloys between palladium and five different promoters were synthesized and tested as propane dehydrogenation catalysts. The structure of the alloy catalysts was characterized by in-situ XAS and in-situ synchrotron XRD. Zinc and indium form alloy structures with site isolated palladium, while gallium, iron and manganese do not. All of the alloys have improved propane dehydrogenation selectivity compared to monometallic palladium.

The propylene production turnover rate of the alloys increased by almost an order of magnitude compared to monometallic Pd, but among the alloys the turnover rates only varied by a factor of two despite the different structures and electronic modifications inherent to each phase. The site isolated alloys had higher propylene selectivity than those that were not site isolated. The site isolated alloys showed stronger electronic modification: both in binding strengths and in Pd projected Density of States (pDOS) by DFT than did the non-site isolated alloys. The commonly used computational selectivity descriptor for dehydrogenation, which is the difference in energy between alkene desorption and alkene C-H bond activation energy correctly predicts that the site isolated alloys will have high selectivity but shows weaker trends for alloys without site isolation. A modified selectivity descriptor, involving the C-C bond breaking barrier in the adsorbed alkyne more accurately reflects the high selectivity of the non-site isolated alloys.

In a third study, RIXS and XPS are used to examine trends in the electronic modification of platinum alloys with transition metal and post transition metal promoters. All alloys show an increase in the energy transfer maximum, showing that alloying modifies energy the filled and unfilled density of states. The increase in the energy transfer maximum in platinum alloys with 3d metals is larger for early transition metals, which by DFT show larger shifts in the d-band center. The post transition elements show significantly larger shifts than to the transition elements, partially due to the lack of orbital overlap between the valence p orbitals and Pt 5d orbitals. Platinum has the same number of valence d electrons regardless of promoter or structure, and redistribution of the 5d electron energy brought about by heteroatomic bonds leads to the observed electronic modifications. The positive binding energy shifts measured by XPS reflect these energy changes, which occur due to changes in the Fermi energy of the alloy, initial state effects and intra and extra atomic relaxation (final state effects). The calculated initial state effect shift is correlated to descriptors of the valence d band, such as the d band center.

1. INTRODUCTION

1.1 Industrial Importance of Light Olefins

The exploitation of shale gas has led to large changes in the energy industry. It is predicted that the total production of natural gas will double from the year 2000 production levels by 2050, with almost all of the new production coming from shale gas. Shale gas differs from conventional natural gas sources in that 5-20% of the gas is composed of C_2+ alkanes. These gasses, typically termed liquefied petroleum gas (LPG) are produced in excess of local demand in the United States market, and it is predicted that the United States will be a net exporter of LPG by 2020 [1]. The LPG fraction of shale gas cannot be incorporated into the existing natural gas pipeline network because they condense at the high pressures used in natural gas pipelines and materials specifications for natural gas only allow a small fraction of C2+ alkanes in the pipeline [2]. LPG is separated out from methane at a regional plant level, and either further purified for the production of purity products or condensed and shipped to further processing hubs by pipeline and rail car.

The ethane and propane fraction of shale gas are becoming the new feedstock for the chemical industry. These light alkanes are used to produce the light olefins ethylene and propylene, which are the two largest volume feedstocks for the chemical industry [3]. Light olefins are produced through dehydrogenation, where hydrogen is removed from a saturated hydrocarbon, resulting in the formation of a C-C double bond. Traditionally, light olefins are produced as a byproduct of the fluidized catalytic cracking of heavy oils and steam cracking of naptha [4]. High demand for gasoline and low oil prices have caused a decrease in the supply of light olefins from these traditional processes, particularly in steam crackers which have shifted from naptha to ethane as a feedstock. The decrease in supply of light olefins (particularly propylene and butadiene) has made on-purpose catalytic dehydrogenation an attractive technology to fill the shortfall in light olefin production. Two industrial catalytic processes are currently used for dehydrogenation of propane and butane: UOP's Oleflex process and McDermott Lummus' Catofin process. The catofin process uses a swing bed design and a chromia on alumina catalyst, and the Oleflex process uses a platinum-tin alloy catalyst on alumina which cycles through a continuous catalyst regenerator [4], [5].

1.2 Dehydrogenation and Hydrogenolysis

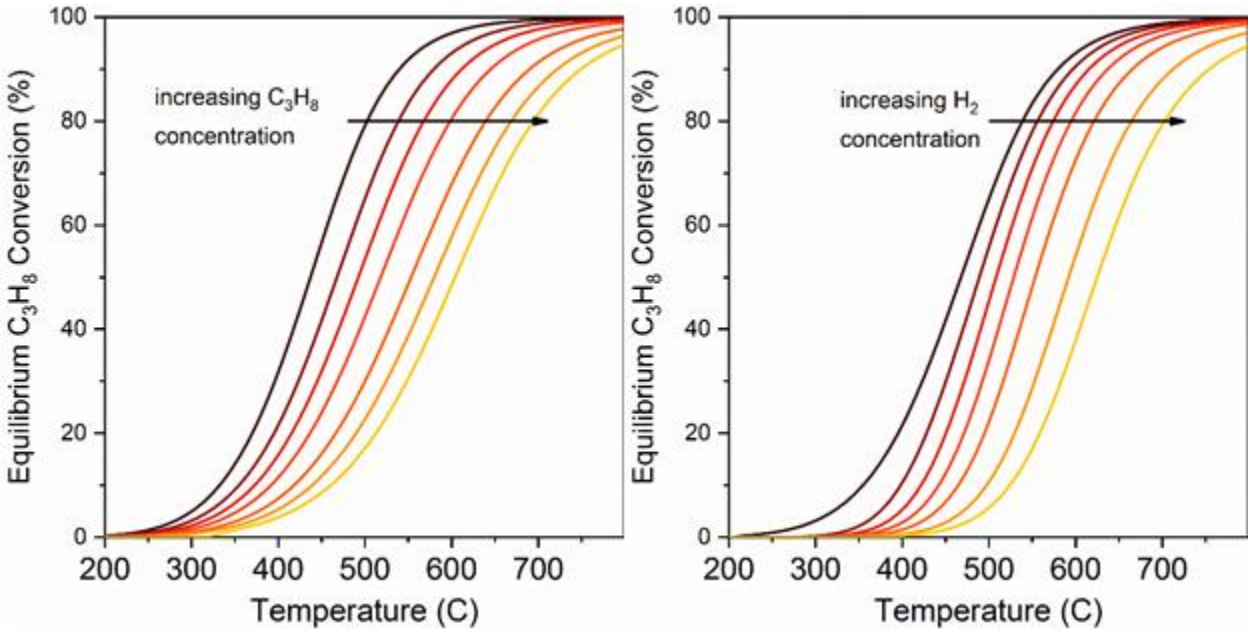

Figure 1: Equilibrium propane dehydrogenation conversion as a function of temperature for (left) increasing propane concentration and (right) fixed propane concentration and increasing hydrogen concentration.

Dehydrogenation is an endothermic reaction and becomes more so as the alkane chain length decreases. In short chain paraffins (C2-C4) dehydrogenation yields alpha olefins, whereas longer parrafins tend to undergo dehydrocycleization to form aromatics. Industrial production of olefins thus requires high temperature (typically above 500°C) to push the equilibrium conversion to reasonable levels. As shown in figure 1, the equilibrium conversion at a given temperature decreases with increasing paraffin concentration and increasing hydrogen content in the feed.

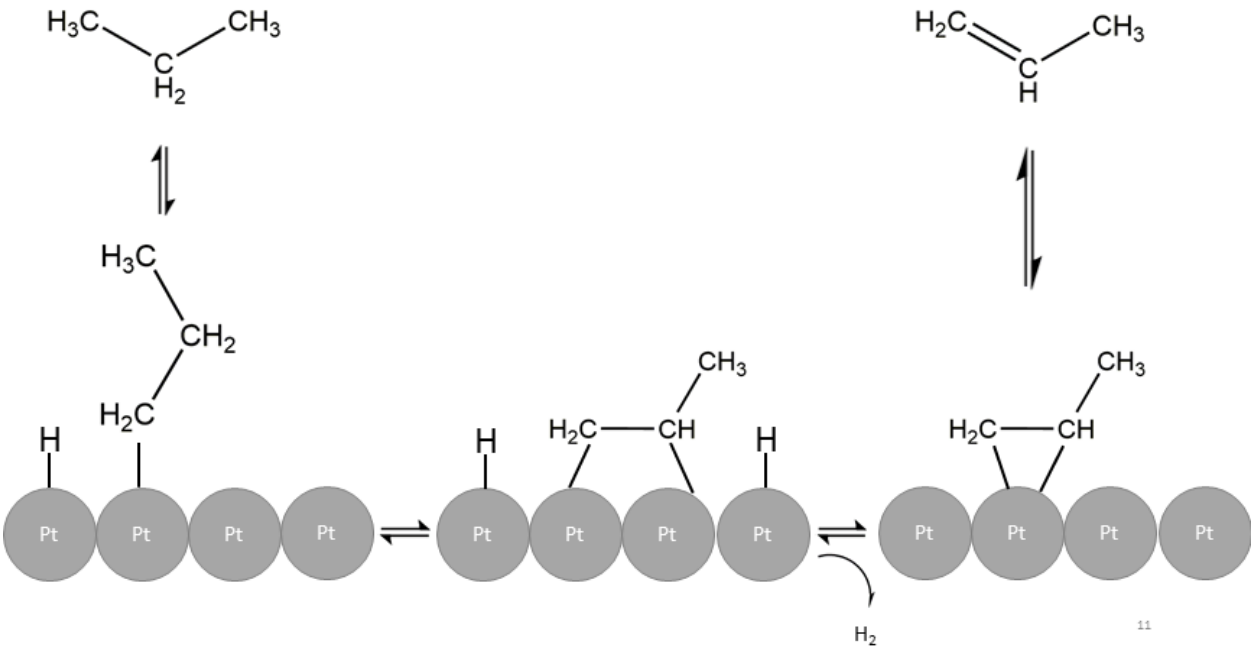

Figure 2: schematic representation of the reverse Horiuti-Polanyi mechanism of propane dehydrogenation on a Pt surface.

Dehydrogenation over metal catalysts occurs through a reverse Horiuti-Polanyi mechanism (shown in figure 2), and follows Langmuir-Hinschelwood kinetics [6], [7]. In this mechanism, an alkane dissociatively adsorbs to a metal surface to form a sigma bonded alkyl group and an adsorbed hydrogen. The dissociative adsorption is the rate limiting step of the dehydrogenation reaction. The surface alkyl group further dehydrogenates from either the alpha or beta carbon. If hydrogen is lost from the alpha carbon, the surface alkylidene moves to a bridge bonded configuration and can further dehydrogenate to from a surface alkylidyne (bonded at a 3 fold site), which has been observed spectroscopically [8], [9]. The surface alkylidyne has been suggested to be a spectator species and a precursor to coke formation [10], [11]. If hydrogen is lost from the beta carbon, the alkene can bond to the surface either through two sigma bonds or through a pi bond. Both species can desorb from the metal surface to form the alkene product, and the two bonding modes can interchange [12]. The alpha beta sigma bonded species can also further dehydrogenate and undergo hydrogenolysis.

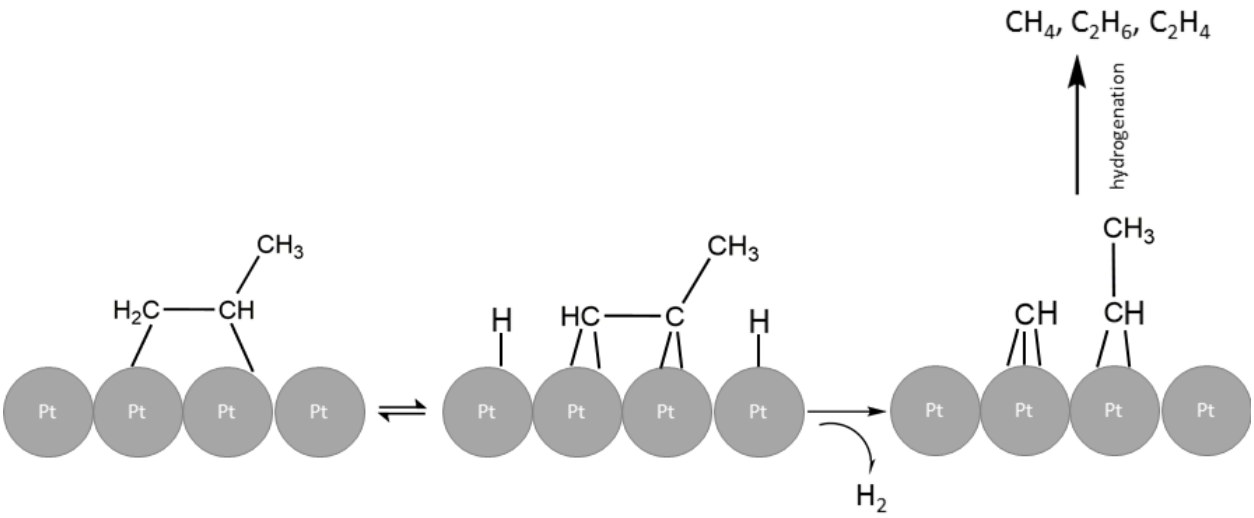

Figure 3: Schematic of the hydrogenolysis mechanism, here depicted as occurring through surface bonded propyne.

Hydrogen is typically cofed to increase catalyst stability and suppress coke formation. Unfortunately, hydrogen is also responsible for the primary side reaction in dehydrogenation: hydrogenolysis. Hydrogenolysis is the rupture of a C-C bond through the addition of hydrogen. Under the conditions of dehydrogenation, surface alkenes can undergo further dehydrogenation (termed deep dehydrogenation). As more hydrogen is removed from the hydrocarbon, the barrier for C-C bond cleavage is lowered, and hence it is thought that hydrogenolysis occurs through a deeply dehydrogenated surface species [13]. Cleaveage of the C-C bond is rate limiting, and the dehydrogenated species are quasi equilibrated with gas phase alkene [14], [15]. In small hydrocarbons, hydrogenolysis typically occurs through adjacent surface bound carbon atoms, and the transition state entropy favors hydrogenolysis of non-terminal C-C bonds in longer alkanes [16], [17]. In branched alkanes, C-C bond cleavage can occur though non-adjacent carbon atoms though an organometallacycle transition state [18].

Hydrogenolysis is weakly structure sensitive, i.e. the hydogenolysis turnover rate is weakly dependent on metal particle size. The dependence was rationalized by the difference in hydrocarbon binding strengths on close packed and stepped platinum surfaces [19]. The structure sensitivity has also been proposed due to the requirement for multiple platinum atoms to catalyze the reaction. The requirement comes from multiply bound carbon atoms formed during deep dehydrogenation. Carbon in metal bound hydrocarbons has a tetrahedral geometry, so for triply

bound carbon species like in an alkylidyne, the surface bound carbon bonds to three platinum atoms [20]. Although it is not agreed upon which deeply dehydrogenated species has the highest degree of rate control in hydrogenolysis under the conditions of dehydrogenation, all deeply dehydrogenated species are bound to the surface through multiple platinum atoms. Another demonstration of the structure sensitivity of hydrogenolysis can be seen in bimetallic catalysts, where one metal is catalytic and the other is not. As the composition of the bimetallic catalyst is changed from pure catalytic metal to almost pure inactive metal, the hydrogenolysis turnover rate drops by more than 4 orders of magnitude while the dehydrogenation turnover rate changes by less than an order of magnitude [21]. The explanation for the difference in behavior was that dehydrogenation can be catalyzed by only a single atom, whereas hydrogenolysis requires multiple atoms. As the bimetallic composition becomes rich in the inactive metal, the active metal ensembles responsible for hydrogenolysis are broken up by the inactive metal.

1.3 Improving Selectivity in Dehydrogenation Catalysts

The bimetallic work of Sinfelt illustrates a common strategy for improving selectivity in dehydrogenation catalysts. A distinction should be made between the structural arrangements in bimetallic systems. A substitutional solid solution bimetallic has the same crystal structure as the parent material, and the second metal randomly substitutes at sites within the parent metal lattice. Other bimetallics, called alloys or intermetallic compounds have narrowly defined stoicheometries and can have crystal structures different from the parent metal. Each atom in an intermetallic compound has a defined position within the unit cell, which contrasts with substitutional solid solutions where any atom within the unit cell can be occupied by either component. This is shown schematically in figure 4.

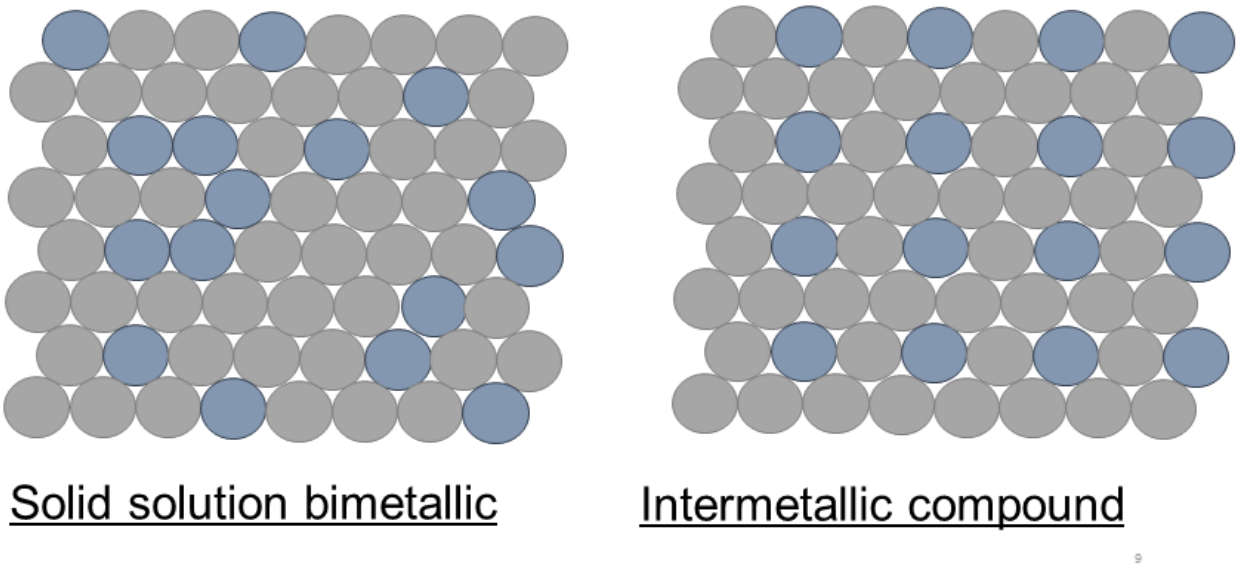

Figure 4: Schematic of the close packed (111) surface of a substitutional solid solution bimetallic (left) and (right) an AB3 intermetallic compound with the AuCu3 prototype phase. Arrangement of the blue impurity atoms is random in the solid solution, and periodic in the intermetallic compound.

The structural differences between intermetallic compound and solid solutions has implications for the two ways that alloying modifies dehydrogenation selectivity. From a geometric standpoint, the breakup of ensembles in the solid solution is random, and isolation of the active metal only occurs at very high dilutions[22]. The distribution of ensemble sizes results in the dehydrogenation selectivity of these systems increasing with composition[23]. In contrast, the ensemble size for an intermetallic compound is determined by the crystal structure and atomic plane. In some intermetallic compounds, the active metal is isolated, i.e. it has no active metal nearest neighbors. Examples of this are PtZn, β_1-PdZn and PdIn, all of which show very high propane dehydrogenation selectivity [24]–[26]. These 1:1 intermetallic compounds with site isolation are in contrast to solid solutions, which typically only show site isolation at more than 1:10 dilutions [23]. In other intermetallic compounds, the active metal is not isolated, such as in alloys with the Pt_3M ($AuCu_3$) structure. The close paced (111) face of alloys with the Pt_3M structure is composed of interconnected groups of 3 platinum atoms.

The other method by which the dehydrogenation selectivity of bimetallics is modified is through electronic modification of the active metal. The electronic modification changes the energy distribution of the filled and unfilled valence d states. The partially filled valence d

orbitals in transition metals are responsible for bonding with adsorbates, with valence s and p conduction electrons playing a much smaller role [27]. The change in energy of the d states leads to modification of adsorbate binding strengths. The correlation was established by Hammer and Nørskov, which correlated the first moment of the d band (hereafter the d band center) of pure metals to the binding strengths of adsorbates [28]. As the d band center moves further in energy from the Fermi level, the binding strength of adsorbates weakens. This is rationalized based on the relative energy of the bonding and antibonding orbitals of adsorbates. As the d band center moves further from the Fermi level, the d band moves further in energy from the adsorbates orbitals, leading to poor orbital overlap and weaker bond strengths. The model was extended to platinum bimetallics by Kitchin and Nørskov, who found that the addition of the second metal causes the d band to broaden and the d band center to shift away from the Fermi level [29].

Because the intermetallic structure of a bimetallic also determines the number of homo and heteroatomic bonds the active metal has, the structure also dictates the electronic effect, which is a result of the bonding with nearest neighbors. Thus, the two effects cannot be completely decoupled, however, considerable effort has been dedicated to determining which effect dominates in determining dehydrogenation selectivity[24], [30]–[32]. Despite the considerable effort, there is less agreement about what causes the electronic effect. Frequently the electronic effect is attributed to electron transfer between the two metals based on spectral shifts in XPS and XANES [30], [32]. The transferred electrons further fill the d band and cause the changes in the d band resulting in improved dehydrogenation selectivity. On the other hand, integrating the number of d states in Pt bimetallics shows that the number of d electrons is the same in Pt metal and Pt bimetallics [29], [33], [34]. Confusingly, charge partitioning methods generally show a net gain in electrons (less than 1 e-) in bimetallic systems [35].

The focus of this body of work is to reconcile seemingly contradictory spectroscopic observations for bimetallics with computational changes seen in the active metal d band density of states. A multi-technique spectroscopic approach is used, with the rational that any explanation for the spectroscopic changes seen by techniques sensitive to changes in the d-band density of states should have a consistent mechanistic basis for the change. In the first study on platinum vanadium alloys, the electronic effect is determined to be due to a change in the energy of the filled and unfilled d states of platinum and not due to electron transfer. The second study works to extend this to palladium intermetallic compounds and explores the predictive power of

computational selectivity descriptors in ranking the selectivity of alloys with different structures and promoters. The final study focuses on platinum alloys with the same structure and different promoters to examine trends in the electronic modification both spectroscopically and computationally.

2. THE ORIGIN OF ELECTRONIC MODIFICATION OF PLATINUM IN A PT_3V ALLOY AND THEIR CONSEQUENCES FOR PROPANE DEHYDROGENATION CATALYSIS

This chapter consists of a manuscript currently under peer review for publication in ACS catalysis

2.1 Abstract

In this paper, we demonstrate the synthesis of Pt_3V alloy and Pt/Pt_3V core/shell catalysts, which are highly selective for propane dehydrogenation. The selectivity is a result of the Pt_3V intermetallic phase, which was characterized by in-situ synchrotron XRD and XAS. Electronic characterization of the alloy phase was accomplished using DFT, XPS, XANES and RIXS, all of which show a change in the energy of the filled and unfilled 5d states resulting from Pt-V bonding rather than a transfer of electrons from the promoter to platinum. The electronic modification leads to a change in the most stable binding site of hydrocarbon fragments, which bind to V containing ensembles despite the presence of structurally equivalent platinum-only ensembles in Pt_3V. In addition, electronic modification destabilizes deeply dehydrogenated species thought to be responsible for hydrogenolysis and coke formation. Ordering of the alloy plays a role in the uniformity of electronic modification of surface platinum, and the breakup of Pt ensembles by surface V cannot be ruled out as a factor contributing to the high dehydrogenation selectivity of the alloy despite the lack of site isolation in Pt_3V.

2.2 Introduction

Propylene is an important petrochemical feedstock eclipsed in production only by ethylene and is used in the production of polymers and other chemicals [3]. Traditionally it is produced as a byproduct from the fluidized catalytic cracking (FCC) process, or steam cracking of naphtha [4]. Recently, due to steam cracking units shifting to ethane, there has been a decrease in the supply of propylene. This decrease in supply has caused on-purpose catalytic dehydrogenation of propane to propylene to become economically attractive. Propane

dehydrogenation is a strongly endothermic reaction and requires reaction temperatures above 500°C to achieve high equilibrium conversion. The two most common industrial catalysts for propane dehydrogenation are supported chromium oxide, used in the Catofin process (McDermott Lummus) and platinum tin alloys, used in UOP's Oleflex process [5], [36].

Selectivity of platinum group metals in dehydrogenation reactions is limited by hydrogenolysis and coking side reactions [15]. Hydrogenolysis, or C-C bond cleavage through the addition of hydrogen across the bond yields methane and ethane. Coking, thought to occur through deep dehydrogenation and subsequent polymerization of surface adsorbed species causes rapid loss of catalytic activity [37]. Of the group VIII metals, platinum has the least hydrogenolysis activity, and hence is the most industrially relevant [38]. To improve the catalytic behavior of platinum, several different promoters have been used which increase the selectivity, rate, and life of the catalyst. The most commonly studied promoters are post transition elements such as Sn, Zn, Ga, and In which all form intermetallic compounds with platinum[7], [24], [32], [39]–[41].

The formation of an alloy between platinum and the promoter leads to changes in the electronic and structural properties of the catalyst. The electronic effect is usually explained by extending Hammer and Nørskov's d-band theory to alloys, in which the promoter element shifts the d-band center away from the Fermi energy leading to a decrease in binding strength of adsorbates[28], [29]. Experimentally it has been observed that alloy formation with platinum causes a decrease in the heat of adsorption of alkenes, resulting in the desorption pathway becoming more favorable than deep dehydrogenation and coking [42], [43]. DFT studies on Pt and Pt-Sn surfaces have come to similar conclusions[13], [44]–[46].

While the qualitative effect of shifting electronic states with respect to the Fermi energy is generally agreed upon, other aspects of how the promoter modifies the electronic properties of alloys, such as the effect of charge transfer, are still debated. Theoretical treatments of alloys generally show a negligible change in the d-band filling in platinum alloys, which would preclude electron transfer from significantly modifying adsorbate bonding [29]. Nikolla et al. used the electron energy loss near edge structure (ELNES) and density functional theory (DFT) to show that the number of d-band holes in a Ni and NiSn alloy is the same, ruling out electron transfer as the mechanism by which the d-band is modified in alloys [34]. Similarly, Schweitzer et al. used DFT to conclude negligible charge transfer occurred in platinum alloys[33]. Instead,

the d-band modification resulted from redistribution of states within the d band brought about by alloying. Alternatively, spectroscopic changes between pure metals and alloys are often explained presupposing interatomic electron transfer [30], [32], [35]. An observed increase in the Pt L_3 edge X-ray absorption near edge structure (XANES) edge energy and decrease in the Pt 4d binding energy measured by X-ray photoelectron spectroscopy (XPS) seen in alloys have been interpreted as a donation of electron density from the promoter to platinum. The donation of electron density further fills the d-band, and the shift of the d-band center and resulting decrease in the binding strength of alkenes is cited as being responsible for the improved selectivity [30], [32].

Recently, Cybulskis et al. used resonant inelastic X-ray scattering (RIXS) spectroscopy to experimentally measure the energy separation between the filled and unfilled 5d states of platinum and a Pt_1Zn_1 (AuCu structure) alloy. They found that alloy formation with Zn leads to an upward shift in the energy of the unfilled states, and a downward shift in the energy of the filled state. DFT results showed that the d-band center in Pt_1Zn_1 in minimally shifted (~0.1 eV) relative to Pt [24]. The change in the energy of the filled and unfilled Pt 5d states was cited as responsible for observed changes in the turnover rate (TOR) while isolation of active sites by Zn was responsible for the increased selectivity.

In addition to purely electronic effects, structural effects may influence reactivity and are caused by changes in crystal structure brought about by the incorporation of a promoter into the active metal lattice. Side reactions such as hydrogenolysis, which require an ensemble of active metal atoms are inhibited due to the decrease in ensemble size brought about by incorporation of an inactive promoter [21], [47]. For a solid solution bimetallic nanoparticle, the breakup of active metal ensembles is random and high dehydrogenation selectivity is only achieved when platinum has few or no platinum neighbors [23]. In contrast, intermetallic compounds require much less promoter to achieve comparable selectivity because they form a surface layer of the alloy, which grows inward as more promoter incorporates into the nanoparticle [25]. For Pd-In alloys, high dehydrogenation selectivity was achieved after formation of continuous shell layer of the tetragonal PdIn intermetallic phase [26]. Other reported intermetallic compounds with high dehydrogenation selectivity include Pt_3In, $PtIn_2$, Pt_1Zn_1, Pd_1In_1 and β_1-PdZn [24], [26], [31], [48]. In the case of $PtIn_2$, Pt_1Zn_1, Pd_1In_1 and β_1-PdZn, the noble metal in the alloy is completely isolated from other noble metal atoms. For Pt_3In, however, the (111) surface is composed of

interconnected 3-fold hollow sites; despite these small platinum ensembles Pt_3In still shows high dehydrogenation selectivity.

Pt_3In has the same prototype phase ($AuCu_3$) as Pt_3Sn, which is the crystal structure generally assumed for nanoparticle Pt-Sn catalysts [49]–[51]. Although the $AuCu_3$ prototype phase also forms in many alloys between platinum and early to mid-3d transition metals such as vanadium, few nanoparticle catalysts have been reported, usually involving oxygen free colloidal synthesis [52]–[54]. Although V, In and Sn can all form the same Pt_3M alloy structure, the electronic effect in a Pt-V alloy should be different from that in either a Pt-Sn or Pt-In alloy due to the valance electron configuration in vanadium. Vanadium has a partially filled 3d shell which should readily overlap with platinum 5d electrons. On the other hand, tin and indium are 4p group elements, which should only have poor orbital overlap between the valence 4p orbital and platinum 5d. Theoretical studies of Pt-3d bimetallics show the strongest modification of the d band in early transition metals such as vanadium, which has been experimentally verified by valence band photoemission measurements on Pt_3M bimetallics [29], [55]. Hence, to further understand the nature of electronic modification in platinum alloys and how its interplay with structural changes influence dehydrogenation selectivity, we synthesized Pt_3V alloy catalysts which have the same $AuCu_3$ structure formed in the Pt_3In and Pt_3Sn phases[56], [57].

Herein, we demonstrate that Pt_3V nanoparticles significantly improve selectivity to propylene as compared to unalloyed platinum. We also assess whether the improvement stems from the changes in the electronic properties of platinum or the breakup of Pt ensembles by successive V incorporation, which leads to formation of a Pt_3V alloy phase. The corresponding changes in the electronic properties are probed using DFT, RIXS, XPS, and XANES. According to the DFT calculations, the binding strength of prototypical intermediates involved in coking and dehydrogenation decrease appreciably due to presence of vanadium promoter. Additionally, the electronic structure of Pt atoms also changes with increasing vanadium incorporation as evidenced from projected density of states (pDOS) analysis of Pt d-states. In agreement with DFT, the XPS, XANES, and RIXS show that the electronic modification of platinum is a change in 5d electron energy rather than change in the number of electrons. These measurements show the strong effect of the promoter in tuning the adsorption and catalytic properties of platinum-based catalysts and, as will be discussed, lead us to conclude that the changes in electronic properties drive the changes in catalytic behavior.

2.3 Experimental

2.3.1 Catalyst Synthesis

Pt-V catalysts were supported on Davisil grade 646 silica (35-60 mesh, Sigma-Aldrich) and synthesized by sequential incipient wetness impregnation. Platinum and Vanadium loadings are given in weight percent with respect to the total catalyst mass. All chemicals were purchased from Sigma-Aldrich and used without further purification. For the synthesis of a 5%V-5%Pt and 5%V-2%Pt, vanadium impregnation was done using a solution of 1:2 molar ratio of ammonium metavanadate to oxalic acid. 0.574 g of ammonium metavanadate and 0.884 g of oxalic acid dihydrate were dissolved in 4 mL of Millipore water. The oxalic acid/ammonium metavanadate solution was heated to 100°C and refluxed for one hour, during which the solution changed in color from red to deep blue, signaling the reduction of vanadium from V^{5+} to V^{4+} and the formation of a vanadium oxalate complex [58]. The V precursor solution was then added dropwise to 5 g of silica. The impregnated silica was dried at room temperature in air for 3 hours, and then overnight at 125°C. Dried catalysts were then calcined at 350°C for 3 hours in flowing air. After calcination, the V-SiO_2 turned yellow in color due to the decomposition of the vanadium oxalate complex and the oxidation of vanadium from the 4+ to 5+ state.

Vanadium impregnation was also done using vanadyl acetylacetonate to study the effect of the vanadium precursor on the dispersion of the vanadium oxide on silica. For the synthesis of a second 2%Pt-5%V catalyst 1.30 g of Vanadyl acetylacetonate was dissolved in 25 mL methanol and impregnated to the pore volume of 5 g of silica (davasil 646, Sigma Aldrich). Due to the low solubility of Vanadyl acetylacetonate, multiple rounds of impregnation and calcination were performed to achieve the desired 5% V weight loading. After each impregnation step, the catalyst was dried at room temperature for 3 hours, then at 125 C overnight and finally calcined at 300 C for 3 hours. Platinum was loaded on the 5V-SiO2(AcAc) to 2% weight in the same manner as the 2Pt-5V catalyst prepared with ammonium metavanadate. The reduction procedure for 2Pt-5V(acac) was identical to the other Pt-V bimetallic catalysts.

Platinum loading for the 5%V-5%Pt catalyst was accomplished by dissolving 0.499 g of platinum tetraammine nitrate in 4 mL of DI water. The pH of the platinum tetraammine nitrate solution was adjusted to 11, as measured by pH paper, by the addition of 30% ammonium hydroxide. The pH adjusted solution was then added to the V-SiO_2 dropwise until the pore volume of the support was filled. After impregnation of the platinum salt, the catalyst was dried

at room temperature for 3 hours and then overnight at 125°C. After drying, the catalyst was calcined at 250°C for 3 hours in flowing air. For the 2%Pt-5%V, the mass of platinum tetraammine nitrate was decreased to 0.200 g. A monometallic Pt catalyst was also synthesized by the above platinum incipient wetness impregnation method using a total platinum loading of 3%.

After calcination, catalysts were reduced in flowing 5% H_2 in N_2. Before starting H_2 flow, catalysts were dried by heating to 100°C in flowing N_2 until no visual condensation was left on the outlet of the reactor. Unless otherwise noted, reduction was performed using a slow ramp (2.5°C/minute) to 250°C with a 20-minute dwell every 25°C, and then a fast ramp (10°C/minute) to 550°C and a 30-minute dwell.

To study the effect of synthetic variables on the resulting structure and catalytic properties several Pt-V catalysts were synthesized varying the weight loading of both metals as well as varying the calcination temperature after vanadium or platinum impregnation. A list of catalysts synthesized, the loading of Pt and V as well as the calcination temperatures after each impregnation step is shown in table 1.

Table 1: Synthesis parameters for Pt and Pt-V catalysts

Name	Pt loading (wt%)	V loading (wt%)	V:Pt atomic ratio	V calcination temperature (°C)	Pt calcination temperature (°C)
3Pt	3	0	-	-	250
5Pt-2.5V	5	2.5	1.9	350	250
5Pt-5V	5	5	3.8	350	250
5Pt-5V-450C	5	5	3.8	350	450
5Pt-5V-500C	5	5	3.8	350	500
5Pt-5V-550C	5	5	3.8	350	550
5Pt-5V-600C	5	5	3.8	350	600
2Pt-5V	2	5	9.5	300	250
2Pt-5V(acac)*†	2	5	9.5	300	250
2Pt-10V†	2	10	19.1	300	250
1Pt-10V†	1	10	38.1	300	250

* vanadyl acetylacetonate was used as the vanadium precursor. For synthetic details, see the supplemental information.
†vanadium impregnation performed in multiple steps with drying and calcination steps between impregnations

2.3.2 Electron Microscopy

Particle size distributions were measured by scanning transmission electron microscopy (STEM) and are reported as volume average particle sizes. Imaging was performed on a FEI Titan using an accelerating voltage of 300 keV and a high angle annular dark field (HAADF) detector. Samples for STEM imaging were prepared by grinding pre-reduced catalyst granules into a fine powder and physically mixing the catalyst powder with a lacey carbon coated 300 mesh copper-TEM grid (SPI supplies). Particle size distributions were measured by counting over 250 particles per sample. Particle sizes were measured using ImageJ software [59].Energy-dispersive X-ray spectroscopy (EDS) maps were taken on a FEI Talos F200X S/TEM with an X-FEG high brightness electron source and a Super-X EDS system. The microscope was operated at an accelerating voltage of 200 keV and has a maximum STEM resolution of 1.2 Å and a maximum EDS mapping resolution of 1.6 Å.

The volume average particle size and standard deviation were calculated using equation 1 and 2 respectively below.

$$\bar{d}[4,3] = \frac{\sum d_i^4}{\sum d_i^3} \tag{1}$$

Where d[4,3] is the volume average particle size and d_i is the diameter of particle i. The standard deviation of the volume average particle size is given by:

$$\bar{\sigma}[4,3] = \sqrt{\frac{\sum \left(d_i - \bar{d}\right)^2 d_i^3}{\sum d_i^3}} \tag{2}$$

2.3.3 Propane Dehydrogenation

Catalytic measurements were performed on a laboratory scale fixed bed microreactor. 0.025 to 0.25 grams of catalyst were diluted to 1 g total mass with Davisil grade 646 (35-60 mesh) and loaded into a quartz tube for testing, creating a catalyst bed approximately 2-3 cm in length. A stainless-steel thermocouple well was inserted into the bottom of the catalyst bed to monitor temperature during reactions, and the catalyst bed was held in place by a quartz wool plug. Four mass flow controllers (parker) were used to supply reactant gasses to the reactor. Effluent gas was analyzed by an online HP 6890 gas chromatograph equipped with an FID

detector and a Restek Alumina BOND/Na2SO4 capillary column. Full separation of C_1 through C_3 products was accomplished in five minutes.

Selectivity to propylene and propane conversion were calculated on a carbon basis of gas phase products. Propylene production turnover rates (TOR) were normalized based on the fraction of surface platinum determined by surface oxidation difference X-ray absorption spectroscopy (described below). Prior to starting propane dehydrogenation tests, the catalyst was first reduced at 550°C in 5% H_2 in N_2 for 30 minutes and purged with N_2 to desorb any H_2 in the catalyst bed. In tests where significant deactivation occurred, initial gas phase product selectivity and conversion are reported by fitting Time on Stream (TOS) data to a first order exponential decay function. To ensure a good fit, 20 data points were taken over a minimum test length of 1.5 hours, the first data point being taken 2-3 minutes into each catalyst test. Each conversion, selectivity and initial turnover rate reported was determined using separate sample of pre-reduced and pretreated sample.

2.3.4 X-Ray Absorption Spectroscopy

Pt L_3 edge in-situ X-ray Absorption Spectroscopy (XAS) was performed at the Materials Research Collaborative Access Team (MRCAT) bending magnet line (10BM) at Argonne National Laboratory's Advanced Photon Source. Measurements were taken in transmission mode from 250 eV before the edge to 800 eV past the edge, with a reference foil spectrum collected simultaneously with all samples using a third ion chamber. Samples were ground into a fine powder and pressed into a self-supporting wafer inside of a steel sample holder. The steel sample holder was placed inside of a 1" OD quartz tube with Ultra-Torr fittings with Kapton® windows at both ends. Treatment gasses were introduced into the reactor via two three-way valves at either end of the reactor. Pre-reduced samples were re-reduced at 550°C for 30 minutes in 100 ccm of 3.5% H_2 in He. After reduction, the reactor was purged at 550°C with He and cooled to room temperature. He gas was purified using a Matheson PUR-Gas triple purifier cartridge to remove trace oxygen impurities. XAS data of the reduced catalysts was collected in He at room temperature. Scans were also taken after exposing the reduced samples to air at room temperature.

To study the surface layer of the Pt-V nanoparticles, EXAFS difference spectra were used. This was accomplished by subtracting EXAFS spectrum of the catalyst oxidized in air at

room temperature from that of the catalyst in the reduced state. Air exposure at room temperature oxidizes the surface layer of platinum nanoparticles [60]. The unchanged spectral features of the particle core common to both the reduced and surface oxidized samples are removed in the difference, leaving only the changes resulting due to the surface oxidation process. The two spectra were energy calibrated such that the edge energy of the concurrently collected platinum foil for both samples was 11.5640 keV. The same edge energy was used for both the oxidized and reduced samples for conversion into k space. The extracted chi data of the oxidized sample was then subtracted from the reduced sample. The difference chi was then k^2 weighted and Fourier transformed over a k range of 3 to 10 $Å^{-1}$. Because the Pt-O scattering present in the oxidized sample is subtracted from the reduced sample, the Pt-O scattering in the difference spectra is phase shifted by π radians with respect to the normal experimental phase function. To fit the phase shifted Pt-O scattering in the difference, the experimental reference Pt-O phase was aligned with the difference Pt-O scattering by adding π radians to the experimental phase function.

XAS data analysis was performed in WINXAS 3.1 software. Coordination numbers and bond distance were obtained using a least squares fit in R-space of k^2 weighted Fourier transformed data. Fourier transforms were taken from 2.7-11.5 $Å^{-1}$ and R-space fits were performed from 1.8-3.2 Å. For Pt-O and Pt-Pt scattering, experimental phase and amplitude functions were extracted from bulk references: $Na_2Pt(OH)_6$ (6 neighbors 2.05 Å) and Pt foil (12 neighbors at 2.77 Å). For Pt-V scattering, an experimental phase and amplitude function was created using a Pt-Fe scattering (7.5 neighbors at 2.66 Å) obtained from pure phase $PtFe_3$ nanoparticles. The bond distance and phase purity of the $PtFe_3$ nanoparticles was verified by in-situ synchrotron X-ray diffraction (XRD). The phase transference error in coordination number introduced by using Pt-Fe to fit Pt-V scattering was estimated using Pt-V and Pt-Fe phase and amplitude functions generated using FEFF and gave coordination numbers 6% lower in magnitude. Fitting was accomplished on isolated first shell coordination in R space by fixing the Debye-Waller factor ($\Delta\sigma^2$) and allowing coordination number (CN), bond distance (R) and energy shift (E_0) to vary.

2.3.5 Resonant Inelastic X-Ray Scattering

RIXS measurements were performed at the MRCAT insertion device line (10ID). Catalyst samples for RIXS measurements were ground into a fine powder and pressed into a self-supporting wafer inside of a stainless-steel sample holder. The sample holder was placed inside of an in-situ cell with X-ray transparent windows which allowed for fluorescence and transmission measurements. The cell consists of a water cooled, resistively heated stage with connections for gas flow and temperature measurement [61]. Samples for RIXS measurement were pretreated by heating in 3% H_2 to 550°C for 30 minutes and then cooling to 100°C for measurement.

RIXS measurements were made by the simultaneous measurement of the Pt L_3 absorption edge in transmission mode and the Pt $L\beta_5$ emission line. The wavelength dispersive spectrometer is based on a bent Laue silicon analyzer coupled to a Pilatus 100K (Dectris) 2D pixel array detector [24], [62]. The analyzer crystal is a 55-µm thick Si(400) wafer, cylindrically bent to ~0.5-m radius. We scatter from the Si(133) reflection with a calculated asymmetry angle of 13.76°. The analyzer was mounted to a rotation stage declined about 20° from horizontal to allow significant elastically scattered X-rays for accurate calibration. Elastic scatter was more than 5x stronger than the peak valence X-ray emission. To resolve the X-ray emission from the tails of the elastic peak, the elastic peak was removed by fitting a Gaussian curve to the truncated data and using a single pair of peak width and center values for the entire data set. The amplitude was varied using a linear function to simulate the effect of beam polarization on the elastic scatter amplitude as a function of emission angle.

2.3.6 X-Ray Photoelectron Spectroscopy

XPS analysis was performed by a Kratos Axis Ultra Imaging DLD spectrometer with an attached catalytic cell (CatCell) for sample heating and gas pretreatments. The XPS spectra were collected using a monochromatic Al Kα (1486.69 eV) radiation and a hemispherical electron energy analyzer operated with a constant pass energy of 20 eV for high resolution spectra. A built in Kratos charge neutralizer was used to mitigate non-homogeneous charging and to improve resolution. Prior to collecting XPS spectra the sample was heated to 550°C in 5% H_2 for 30 minutes in the CatCell. Following reduction, the sample was transferred under UHV (without any contact with air) within 1 minute into the analysis chamber for XPS measurement. XPS

spectra were processed using CasaXPS software. The Pt 4f peaks were fitted by an asymmetric Lorentzian function (LF(a,b,c,d) function in CasaXPS) after subtraction of a Shirley background. Charge correction was performed by setting the Si 2p binding energy to 103.7 eV.

2.3.7 X-Ray Diffraction

In-situ synchrotron X-Ray diffraction (XRD) spectra were collected at the 11-ID-C beam line at the Advanced Photon Source. XRD experiments were performed in transmission geometry, using an X-ray energy of 106.257eV (0.11684 Å) and a PerkinElmer large area detector. XRD samples were ground into a fine powder and pressed into a self-supporting wafer using a set of stainless-steel dies. Samples were loaded into a water cooled Linkam stage, which allowed for heating and cooling as well as gas flow. Samples were pretreated by first purging the cell with He before ramping to 550°C under flowing 3.5% H_2 in He. He used in the XRD experiments was purified in the same manner as the XAS experiments above. After a reduction period of 15 minutes under the above conditions, XRD patterns were collected at temperature, and again after cooling the sample to 35°C in 3.5% H_2 in He. Scans of the empty Linkam cell (in He and 3.5% H_2) and bare Davisil grade 646 silica were collected for background subtraction. The collected 2D diffraction patterns were calibrated using a CeO_2 standard sample, and integrated to give standard powder diffraction data using Fit2D software [63], [64]. Theoretical XRD patterns were calculated using crystallographic references and the Materials Analysis Using Diffraction (MAUD) software[[65]]. Multiple peak fitting was performed using OriginPro software using a mixed Gaussian-Lorentzian peak profile.

2.3.8 Density Functional Theory

Electronic structure calculations were performed using periodic, self-consistent Density Functional Theory (DFT), as implemented within the Vienna ab Initio Simulation Package (VASP) [66]–[69]. Electronic interactions were modeled using Perdew-Burke-Ernzerhof exchange-correlation functional [70]. Projector augmented wave (PAW) core pseudopotentials were used for all calculations [71]. Lattice constant optimization and bulk binary phase diagram calculations were done using a plane-wave cutoff energy of 600 eV and a 10x10x10 Monkhorst-Pack K-point grid. Methfessel-Paxton smearing was used to reduce the Pulay stress [72], [73]. Lattice constants were converged with a force criterion of 0.02eV/Å, giving a lattice constant of

3.98 Å for Pt and 3.92 Å for Pt_3V. Surface calculations were conducted on close-packed (111) facets with $\sqrt{3}x\sqrt{3}x5$ supercells of Pt and Pt_3V. For the surface calculations, plane-wave cutoffs of 500 eV and Monkhorst-Pack K-point grids of 4x4x1, and Methfessel-Paxton smearing were employed. The slabs were composed of 5 layers with the bottom 2 layers constrained to represent the bulk. To calculate binding energetics for Pt_3V skin configurations, Pt atoms in a 2x2x5 Pt slab were replaced with V atoms, corresponding to the surface ordering of Pt_3V (111) and allowed to relax. All calculations were spin polarized, and a dipole correction was employed perpendicular to slab surface to reduce periodic image interactions. Projected density of states calculations were conducted on (111) closed packed surfaces for Pt and Pt_3V with 2x2x5 slab super cells. For pDOS calculations, a plane-wave cutoff of 800eV, a denser k-point grid of 13 × 13 × 1, and tetrahedron Blöchl smearing were used. The density of states was projected according to the Wigner−Seitz radius provided by the PAW potential. The DOS was evaluated on 800 grid points between a range of ±8 eV from the corresponding Fermi energy for the system. Methfessel-Paxton smearing with smearing width of 0.2 eV was used to generate a smoother pDOS. The Pt d-band center was calculated as the first moment of the pDOS of d-electrons for surface platinum atoms, and the d-band width was evaluated as the square-root of its second moment. Transition-state (TS) energy calculations were performed with CI-NEB where each optimized TS structure was checked with a normal mode analysis to ensure that only a single imaginary frequency exists [74]. Gas phase species were calculated with a plane-wave cutoff of 500eV with gaussian smearing and a gamma k-point within a 20x21x22 Å supercell. For setup, visualization and analysis of atomistic simulations, Atomic Simulation Environment (ASE) was used [75]. Rendering of the atomic configuration was done using OVITO [76].

2.4 Results

2.4.1 Structural Characterization

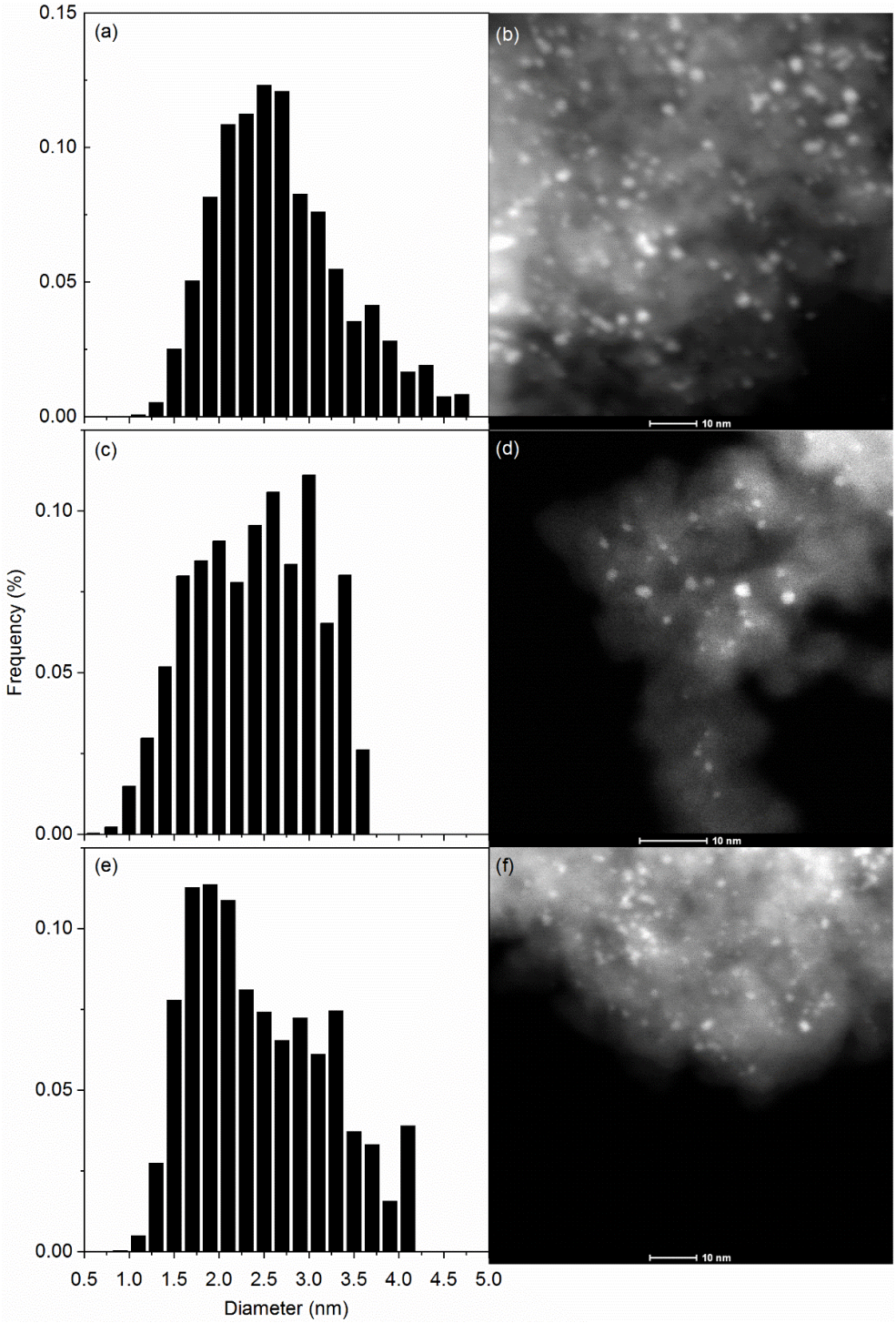

Figure 5: Volume average particle size distributions and representative STEM images for 3Pt (a,b), 5Pt-5V (c,d), 2Pt-5V (e,f)

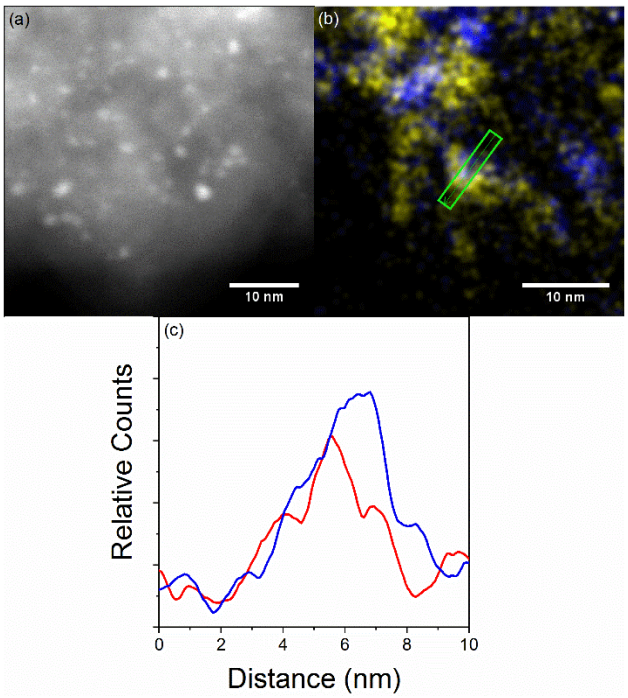

Figure 6: Pt-V catalyst characterization by electron microscopy. a) HAADF STEM image of 2Pt-5V. b) EDS map of 2Pt-5V with Pt in blue and V in yellow. c) EDS line scan of green boxed area in b, with Pt in blue and V in Red.

Metal nanoparticle sizes of the 3Pt, 5Pt-5V and 2Pt-5V catalysts were determined by STEM imaging (shown in figure 5). The volume average particle size for 3Pt, 5Pt-5V and 2Pt-5V were 2.6±0.5 nm, 2.2±0.5 nm, and 2.2±0.7 nm respectively. All three particle sized distributions deviate from pure Gaussian shape with an asymmetric tail towards higher particle sizes. Similar asymmetry has been reported for Pt nanoparticles on alumina after a high temperature treatment due to sintering [77]. All three samples have a particle size within one standard deviation of one another. Figure 6a shows a HAADF STEM image of 2Pt-5V after reduction at 550°C (and subsequent exposure to air) and is representative of all samples measured. All three catalysts have average particle sizes of 2-2.5 nm. Figure 6b shows overlaid EDS elemental maps of Pt (blue) and V (yellow) for 2Pt-5V. Both platinum and vanadium are present in the small particles. The vanadium oxide clusters, which were not distinguished strongly from the support in the STEM images, can be seen in the EDS maps. Pt particles present in the maps are close to or in intimate contact with vanadium, though the amount varies from particle to particle. Figure 6c shows a line scan taken from the EDS map pictured in 6b. The Magnitude of the V and Pt signals are comparable across the particle, demonstrating the

incorporation of V throughout the platinum particle as opposed to only on the surface layer, though vanadium oxide cannot be distinguished from V in a bimetallic. To determine if a Pt-V bimetallic forms, XAS was used to probe the local environment of Pt and V.

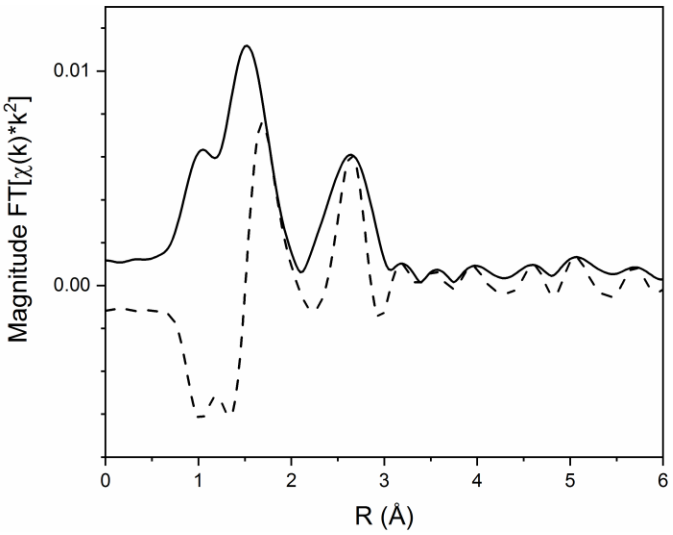

Figure 7: V K edge EXAFS of 5Pt-5V after reduction at 550°C in 3.5% H2.

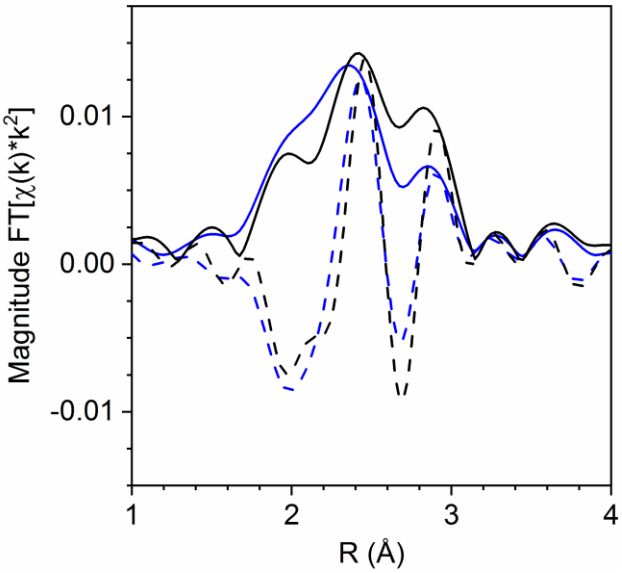

Figure 8: in-situ EXAFS magnitude (solid lines) and imaginary (dashed lines) of 3Pt (Black) and 2Pt-5V (blue) catalysts. Spectra were collected at room temperature in He after a 30-minute reduction at 550°C in 3.5% H2

XAS was used to verify that vanadium incorporates into the metallic platinum particles and forms a bimetallic phase. From the vanadium K edge (figure 7), only scattering from V-O and second shell V-O-V is evident after reduction of the 5Pt-5V sample, suggesting most of the vanadium is present as oxide clusters. Figure 8 shows the R-space magnitude and imaginary components of the EXAFS for 3Pt (black) and 2Pt-5V (blue). The lack of a low R Pt-O scattering peak (below about 2 Å) confirms that all samples are metallic. 3Pt shows the three peaks characteristic of scattering from metallic platinum. Compared to 3Pt, the first peak in the 2Pt-5V sample at 2 Å increases slightly in intensity, and the third peak at 3 Å decreases slightly in intensity. Additionally, the peaks in 2Pt-5V shift to lower R compared to 3Pt. The changes occur due to the formation of a Pt-V bimetallic nanoparticle, which gives rise to scattering from Pt-V in addition to Pt-Pt. Because scattering intensity is proportional to the number of electrons of the neighbor, scattering from Pt-V is weaker than scattering from Pt-Pt pairs and the shape of the first shell scattering envelope in the bimetallic still resembles monometallic platinum. Fits of the first shell EXAFS and XANES edge energies are shown in Table 2.

Table 2: XANES edge energies and EXAFS fitting parameters for 3Pt, 5Pt-5V and 2Pt-5V: coordination number (CN), bond distance (R), Debye-Waller factor (σ2), and E0 correction (E0)

Sample	XANES edge energy (eV)	Scattering Pair	CN	R (Å)	σ_2 (Å^2)	E0 (eV)
3Pt	11564.0	Pt-Pt	8.8	2.74	0.002	-0.9
5Pt-5V	11564.2	Pt-Pt	6.5	2.73	0.003	-0.8
		Pt-V	2.0	2.71	0.003	2.6
2Pt-5V	11564.4	Pt-Pt	6.2	2.72	0.003	-1.6
		Pt-V	2.9	2.72	0.003	2.3

For 3Pt, a high-quality fit was obtained by fitting with a single Pt-Pt scattering path. To fit the Pt-V samples, it was necessary to include a second scattering path (Pt-V) to fit the data. The total coordination number, which is correlated to the metal particle size [78], of all three catalysts is close to 9, which agrees with the STEM results showing that all three catalysts have similar particle sizes (2-2.5 nm). The bond distance of 2.74 Å in the 3Pt sample is characteristic of small Pt nanoparticles, where the decrease in average coordination number causes a slight contraction of the Pt-Pt bond distance from the bulk value of 2.77 Å [79]. In the Pt-V samples, the Pt-Pt bond distance was also contracted, with 5Pt-5V having a bond distance of 2.73, and

2Pt-5V having a Pt-Pt bond distance of 2.72 angstroms. For both alloy samples, the Pt-V bond distance for each sample was the same as the respective Pt-Pt bond distance. The 5Pt-5V catalyst had a Pt-Pt coordination number of 6.5 and a Pt-V coordination number of 2, leading to a ratio of Pt-V to Pt-Pt neighbors of 0.31. The 2Pt-5V catalyst had a Pt-Pt coordination number of 6.2 and a Pt-V coordination number of 2.9, giving a Pt-Pt/Pt-V coordination number ratio of 0.47. The coordination number ratio gives a measure of the extent of vanadium incorporation, with a higher ratio corresponding to a larger degree of vanadium incorporation.

Table 3: Average Pt-Pt and Pt-V coordination numbers and bond distances for Pt-V catalysts.

Sample	Scattering Pair	Coordination number	Bond distance (Å)	Pt-V/Pt-Pt coordination number rato
5Pt-5V-C450C	Pt-Pt	8.1	2.74	0.22
	Pt-V	1.8	2.72	
5Pt-5V-C500C	Pt-Pt	8.8	2.75	0.20
	Pt-V	1.8	2.73	
5Pt-5V-C550C	Pt-Pt	9.9	2.76	0.17
	Pt-V	1.7	2.73	
5Pt-5V-C600C	Pt-Pt	10.6	2.76	0.14
	Pt-V	1.5	2.73	
5Pt-2.5V	Pt-Pt	7.4	2.74	0.31
	Pt-V	2.3	2.71	
2Pt-5V(AcAc)	Pt-Pt	5.6	2.72	0.50
	Pt-V	2.8	2.71	
2Pt-10V	Pt-Pt	5.3	2.72	0.55
	Pt-V	2.9	2.71	
1Pt-10V	Pt-Pt	4.3	2.69	0.56
	Pt-V	2.4	2.68	
5Pt-5V-R200C	Pt-Pt	5.7	2.73	0.32
	Pt-V	1.8	2.69	

Table 4: EXAFS fits and XANES edge energies for Pt-V catalysts.

Scattering pair	Pt-Pt				Pt-V				XANES
parameter	CN	R (Å)	DWF ($Å^2$)	E0 (eV)	CN	R (Å)	DWF ($Å^2$)	E0 (eV)	Inflection point (eV)
5Pt-2.5V	7.4	2.74	0.003	-0.7	2.3	2.71	0.003	1.6	11564.2
2Pt-5V(acac)	5.6	2.72	0.003	-1.3	2.8	2.71	0.003	1.9	11564.4
2Pt-10V	5.3	2.72	0.003	-1.8	2.9	2.71	0.003	2.0	11564.5
1Pt-10V	4.3	2.69	0.004	-1.4	2.4	2.68	0.004	1.1	11564.6

Table 3 and 4 gives the Pt-V and Pt-Pt coordination number, bond distance, and coordination number ratio for 9 additional Pt-V catalysts synthesized with the goal of determining the effect of various synthetic variables on vanadium incorporation. The first four catalysts listed are 5Pt-5V catalysts which were calcined after platinum impregnation at temperatures higher than 250C. The latter four catalysts were Pt-V catalysts where the ratio of Pt:V weight loading was varied. Lastly, a fresh 5Pt-5V catalyst was reduced at low temperature to study at what temperature V incorporation starts.

For the 5Pt-5V samples calcined at 250, 450, 500, 550 and 600°C, the Pt-V:Pt-Pt coordination number ratio decreased as the calcination temperature increased: thus, high calcination temperatures lead to less vanadium incorporation. The total coordination number (Pt-Pt+Pt-V) also increased as the calcination temperature increased, which reflects an increasing metal particle size with increasing calcination temperature. In the 5Pt-2.5V sample, the coordination number ratio was close to that 5Pt-5V, demonstrating that the incorporation of V is less sensitive to V loading over the composition range tested. In contrast, samples where the Pt loading was decreased from 5% to 2% or 1%, the coordination number ratio increased. The upper limit in neighbor ratio was close to 0.5, as evidenced by the diminishing increase in neighbor ratio measured at the extreme of V:Pt ratios tested represented in the 2Pt-10V and 1Pt-10V samples. The total coordination number also tended to decrease with the total platinum loading regardless of the V loading. The presence of Pt-V scattering in 5Pt-5V-R200C (shown in figure 9 and fit in table 5) shows that vanadium reduces to the metallic state and forms a bimetallic at close to the same temperature that platinum reduces to the metallic state. All synthesized catalysts showed Pt-Pt scattering, which rules out the presence of PtV or PtV_3 in which Pt has only V nearest neighbors. The presence of nearest neighbor platinum would be expected in a Pt rich solid solution or the Pt_3V alloy phase.

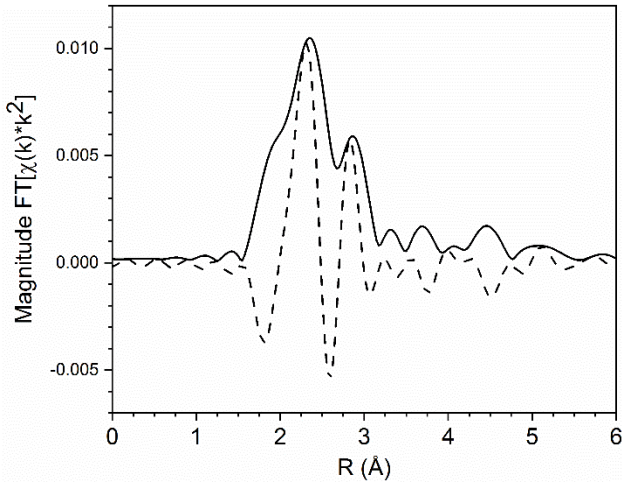

Figure 9: R space EXAFS magnitude (solid black) and imaginary (dashed black) components of 5Pt-5V reduced at 200°C in 3.5% H2.

Table 5: EXAFS fit of 5Pt-5V after reduction at 200°C.

Sample	Path	CN	R (Å)	σ^2 (Å^2)	E0 (eV)
5Pt-5V-R200C	Pt-Pt	5.7	2.73	0.003	-0.8
	Pt-V	1.8	2.69	0.003	1.1

To study the long-range order and phase composition of the Pt-V nanoparticles, in-situ synchrotron XRD was used. Due to the small crystallite size of the particles being measured (ca. 2 nm), it was necessary to use in-situ synchrotron XRD to collect data of sufficient quality for quantitative analysis. Due to the high energy of the X-rays used (106.257 keV), the diffraction peaks appear over a much smaller 2θ range (2-8 degrees) than a pattern obtained on a typical laboratory XRD instrument (20-80 degrees). Use of a high X-ray energy above the Pt K absorption edge is necessary to resolve the small fraction of the sample that is metallic (<5%); at high energy, the difference in absorption cross section between the support and platinum is large enough to resolve metallic peaks from the amorphous signal from the support. The high flux provided by an insertion device coupled with a wide area detector also gives a signal to noise ratio high enough to resolve the weak, broad diffraction peaks resulting from nanoparticles less than 3 nm in diameter [80]. Finally, in-situ measurement under reducing conditions ensures that the surface of the nanoparticle is metallic. Ex-situ XRD on small metal nanoparticles where the surface is oxidized can produce misleading results with respect to the observed lattice parameter and particle size [80].

Distinguishing between Pt and Pt_3V is also complicated by the small difference in their unit cell parameters: 3.92 Å for platinum and 3.87 Å for Pt_3V [56]. Additionally, below 10 nm, the lattice parameter of both Pt and Pt_3V change with particle size due to the contraction of bond distance that occurs in nanoparticles. Leontyev et al. used synchrotron XRD to measure the lattice parameter contraction in platinum nanoparticles of different size [81]. At two nm in size, the lattice parameter of Pt nanoparticles decreased from the bulk value by 0.03 Å, a decrease comparable in size to the lattice parameter difference between Pt and Pt_3V (0.05 Å). Because both vanadium incorporation and decreasing particle size each decrease the lattice parameter, changes cannot be solely attributed to composition unless a comparison is made between a Pt and Pt-V particle of the same size.

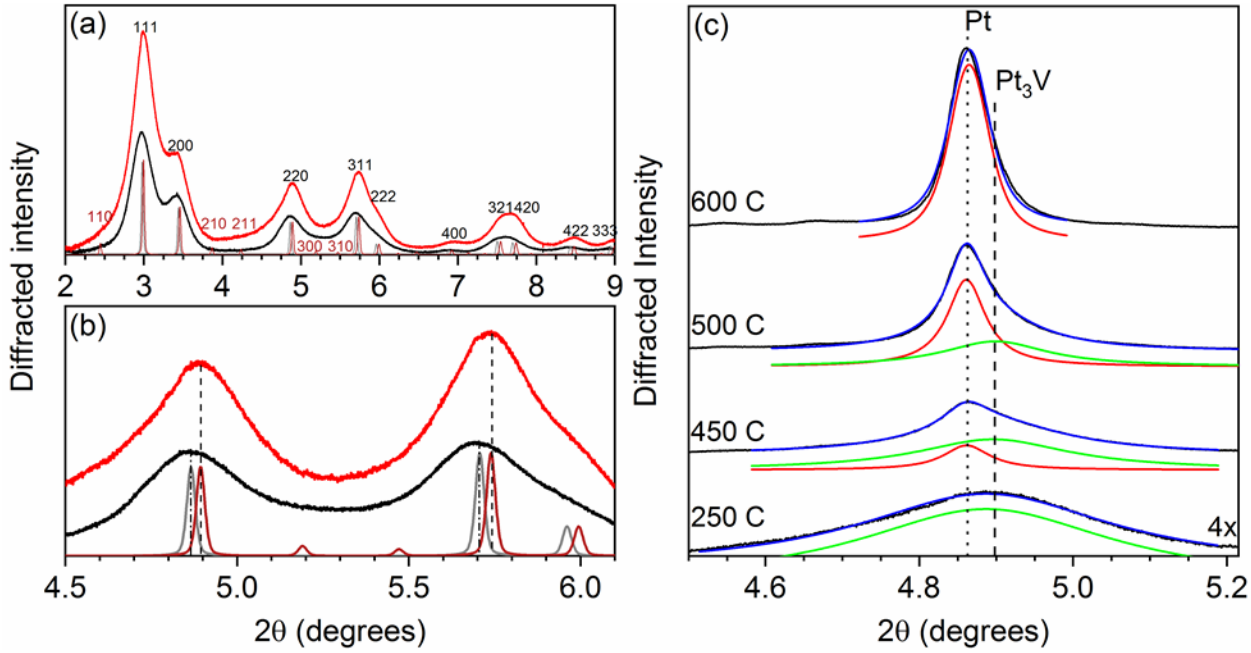

Figure 10: In-Situ synchrotron XRD patterns of a) 3Pt (black), 5Pt-5V (red). Fundamental FCC lines are labeled in black, and the first five superlattice lines of Pt_3V are labeled in red. b) Expanded view of the 220 and 311 reflection for the above samples with vertical dashed lines denoting experimental peak positions. All experimental spectra were collected at 35°C in 3.5% H2 after reduction at 550°C. Simulated patterns of Pt with a lattice parameter of 3.89 Å (grey) and Pt_3V with a lattice parameter of 3.87 Å (crimson) are also shown. c) Multi component fits of the 220 XRD reflection for 5Pt-5V catalysts calcined at 250°C, 450°C, 500°C, and 600°C. Raw data is shown in black, component fits in red (Pt) and green (Pt_3V) and total fit (Pt+Pt_3V) in blue. Component fits have been offset for clarity. Spectra were collected at 35°C in 3.5% H2 after reduction in the same atmosphere at 550°C.

Figure 10 shows the in-situ synchrotron XRD pattern at 35°C in 3.5% H_2 of 3Pt and 5Pt-5V after reduction at 550°C for 30 minutes. The fundamental lines characteristic of an FCC metal are present, ruling out the presence of Pt-V phases without FCC symmetry, such as PtV or Pt_2V. The XRD peaks are broad and weak in intensity due to the small average particle size present in the sample, as described above. No diffraction from a crystalline vanadium oxide phase are present, demonstrating that the unreduced vanadium in the sample is well dispersed. The peak positions of the 3Pt catalyst agree with the simulated Pt pattern with a lattice parameter of 3.89 Å. The peak positions of the 5Pt-5V catalyst are shifted to higher angle than the 3Pt catalyst. Simulating a Pt_3V pattern with a lattice parameter of 3.87 Å gives excellent agreement with the peak positions of the 5Pt-5V sample. Super lattice diffraction peaks could not be resolved due to the small average crystallite size of the sample. Figure 3b shows details of the 220 and 311 reflections for 3Pt and 5Pt-5V after a reduction treatment at 550°C. The 220 and 311 peak positions for the 5Pt-5V and 2Pt-5V catalysts are shifted to a higher 2θ value than those of the 3Pt catalyst of the same size (2-2.5 nm), indicating a decrease in the lattice parameter due to the incorporation of vanadium.

Vanadium present in the platinum nanoparticles could be arranged as a random solid solution or as an ordered intermetallic compound. To distinguish between the two possibilities, a series of 5Pt-5V samples were synthesized, where the calcination temperature after the impregnation of platinum tetraammine nitrate was increased from the 250°C temperature used for the above characterized 5Pt-5V catalyst to 450, 500, 550 and 600°C respectively. Higher calcination temperatures lead to larger platinum metal particle sizes after reduction [82]. Increasing the calcination temperature also decreases the dispersion of vanadium oxide [83]. These combined effects should lead to a lower degree of vanadium incorporation as the calcination temperature is increased.

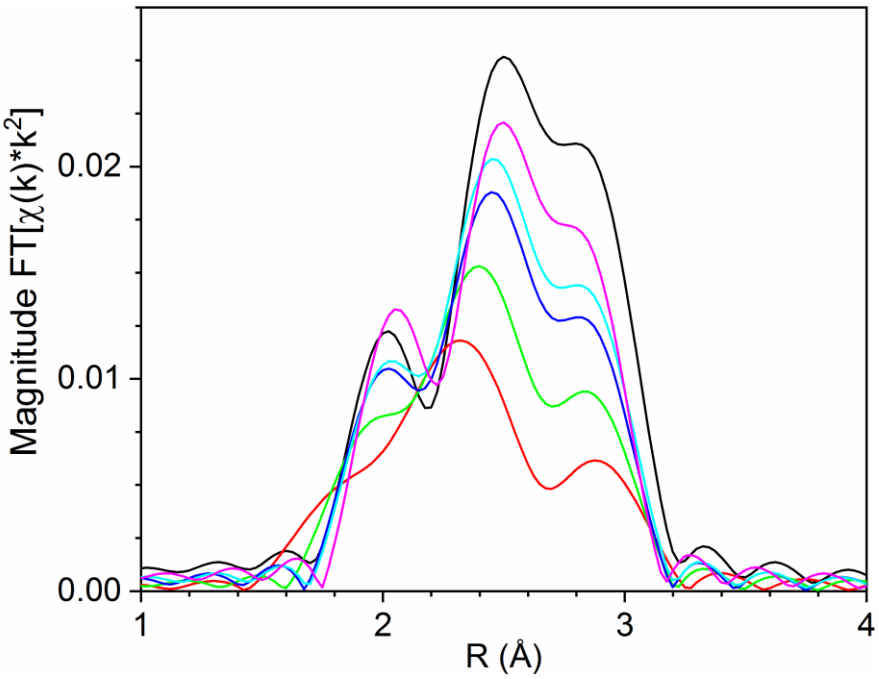

Figure 11: In-Situ Pt L3 edge EXAFS of Pt foil (black) and 5Pt-5V catalysts calcined at 600°C (magenta), 550°C (blue), 450°C (green), and 250°C (red). Scans were taken at room temperature in He after reduction at 550°C in 3.5% H2.

Table 6: First shell EXAFS fits and XANES edge energies of 5Pt-5V catalysts calcined at different temperatures.

Calcination temperature (°C)	XANES	Pt-Pt				Pt-V			
	Inflection point (eV)	CN	R (Å)	DWF (Å^2)	E0 (eV)	CN	R (Å)	DWF (Å^2)	E0 (eV)
Pt Foil	11564.0	12	2.77	0	0	-	-	-	-
600C	11564.1	10.6	2.76	.001	-0.6	1.5	2.73	.001	2.2
550C	11564.1	9.9	2.76	.001	-0.7	1.7	2.73	.001	1.9
500C	11564.1	8.8	2.75	.001	-0.4	1.8	2.73	.001	1.9
450C	11564.1	8.1	2.74	.002	-1.1	1.8	2.72	.002	1.3
250C	11564.2	6.5	2.73	.003	-0.8	2.0	2.71	.003	2.6

Figure 10c shows the 220 reflection for 5Pt-5V catalysts calcined at different temperatures. Consistent with the EXAFS results showing an increase in total coordination number (shown in Figure 11 and Table 6), the increase in calcination temperature results in larger particles, which is reflected in the XRD spectra as a decrease in the peak full width at half

maximum (FWHM). For the 5Pt-5V catalysts calcined at 450°C and above, the main peak position matches that of the 3Pt catalyst at 4.866 2θ, whereas the catalyst calcined at 250°C has a peak position at higher angle than the platinum catalyst. For the 5Pt-5V catalysts calcined at 450°C, and 500°C, the peak shape is asymmetric, with a shoulder at 4.896 and 4.899 2θ respectively. Asymmetric peaks are consistent with 2 phases, rather than a solid solution.

Fitting parameters for the 220 reflection for 3Pt and the four 5Pt-5V catalysts calcined at different temperatures are shown in Table 7. For the samples calcined at 250°C and 600°C, a single Lorentzian peak was sufficient to fit the spectra. For the samples calcined at 450°C and 500°C, a second Lorentzian was necessary to properly fit the high angle shoulder. The main peak for the 5Pt-5V catalysts calcined at 600, 500 and 450°C lies at 4.861, 4.861 and 4.865 2θ, respectively, and is attributed to diffraction from Pt. Using the Scherrer equation the particle size calculated using the FWHM of the main peak was 9, 11 and 16 nm for the sample calcined at 450, 500 and 600°C, respectively. In the 5Pt-5V samples calcined at 450°C and 500°C, the peak position of the shoulder was 4.896 and 4.899 2θ respectively. This peak is attributed to diffraction from Pt_3V based on the matching lattice parameter of 3.87 Å [56]. The particle size of the shoulder component peak was 3 and 4 nanometers for the 5Pt-5V samples calcined at 450°C and 500°C respectively. The 5Pt-5V sample calcined at 250°C has peak position 0.01 degrees lower than the shoulder component of the 450°C and 500°C samples at 4.887 2θ, which corresponds to a lattice parameter of 3.88 Å. In the 5Pt-5V-C250C sample, the particle size is too small to separately fit diffraction from Pt and Pt_3V, and the resulting peak position is the average lattice parameter of both phases, which is 0.01 Å larger than that found for the Pt_3V shell layers in the 5Pt-5V samples calcined at 450 and 500°C.

Table 7: Fits of the 220 reflection for 3Pt and 5Pt-5V catalysts calcined at different temperatures

Sample		FWHM (2θ)	Crystallite size (nm)	Peak Position (2θ)	Unit cell parameter (Å)	M-M bond distance (Å)
3Pt	Peak 1 (Pt)	.315	2	4.866	3.89	2.75
5Pt-5V-250C	Peak 2 (Pt_3V)	.401	2	4.887	3.88	2.74
5Pt-5V-450C	Peak 1 (Pt)	.073	9	4.861	3.90	2.76
	Peak 2 (Pt_3V)	.241	3	4.896	3.87	2.74
5Pt-5V-500C	Peak 1 (Pt)	.060	11	4.861	3.90	2.76
	Peak 2 (Pt_3V)	.166	4	4.899	3.87	2.73
5Pt-5V-600C	Peak 1 (Pt)	.042	16	4.865	3.89	2.75

2.4.2 Electron Characterization

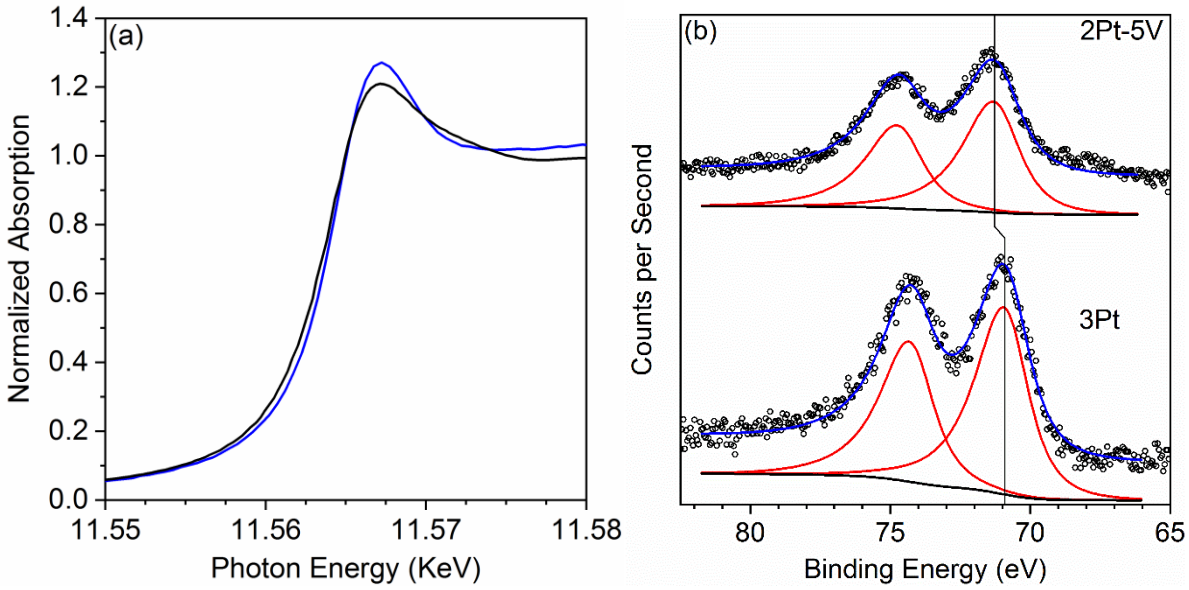

Figure 12: a) In-situ Pt L3 edge XANES of 3Pt (Black) and 2Pt-5V (blue). Spectra were collected at room temperature in He after reduction at 550°C in 3.5% H2 for 30 minutes and a subsequent purge in He at 550°C. b) High resolution Pt 4f XPS spectra of 2Pt-5V and 3Pt after a reduction treatment in 5% H2 at 550°C for 30 minutes. Black Circles: Raw data, black line: Shirley background, Red lines: component fits, Blue line: total fit. Background and components are offset for clarity. The vertical line denotes the peak position of the Pt 4f7/2 component of 3Pt and 2Pt-5V.

Figure 12a shows the Pt L_3 edge XANES for 3Pt and 2Pt-5V after reduction in 3.5% H2 at 550°C. The edge energy (measured as the energy of the first zero crossing of the second derivative of the XANES) for the 3Pt catalyst was identical to the concurrently measured foil value of 11.5640 keV. The edge energy of 2Pt-5V was shifted 0.4 eV higher than the Pt foil. The white line shape of 2Pt-5V is also different than the 3Pt sample which is a platinum nanoparticle of the same size, becoming narrower and higher in intensity. These changes occur due to the incorporation of metallic vanadium into the platinum nanoparticles. Shifts to higher energy of the XANES and changes in the white line shape have been reported in other platinum alloy catalysts [24], [26], [84]. The white line shape is also sensitive to particle size and the presence of adsorbates [85], [86]. In contrast to platinum alloys with Sn, In and Zn which have a lower white line intensity than a platinum nanoparticle of the same size, Pt-V bimetallics have a white line intensity that is higher which signifies modification of the Pt unfilled density of states in the bimetallic sample.

Table 8: Pt 4f XPS fitting parameters for 3Pt and 2Pt-5V

Sample	Pt $4f_{7/2}$ binding energy(eV)	FWHM (eV)	Spin orbital splitting (eV)	LF parameter a	LF parameter b	LF parameter c	LF parameter d
3Pt	70.9	1.7	3.3	1	1.6	10	30
2Pt-5V	71.3	2.0	3.4	1	1.6	10	30

Figure 12b shows the Pt 4f high resolution XPS spectra of 3Pt and 2Pt-5V. XPS spectra were collected following a reduction treatment in 5% hydrogen at 550°C for 30 minutes in the CatCell and UHV transfer. Fitting parameters for the Pt 4f high resolution XPS spectra are given in table 8 of the supplemental information. Fitting gave a binding energy for 3Pt and 2Pt-5V of 70.9 and 71.3 eV respectively. Platinum metal has a Pt $4f_{7/2}$ binding energy of 71.0 eV with an asymmetric peak shape towards higher binding energy, while platinum oxides have higher binding energies between 73-75 eV with a symmetric peak shape [87]. The asymmetric peak shape and binding energy for both samples is consistent with platinum in the metallic state. The core level shift (CLS) for 2Pt-5V is calculated as the difference in binding energy between the pure metal (3Pt) and the alloy, giving an increase in binding energy of 0.4 eV.

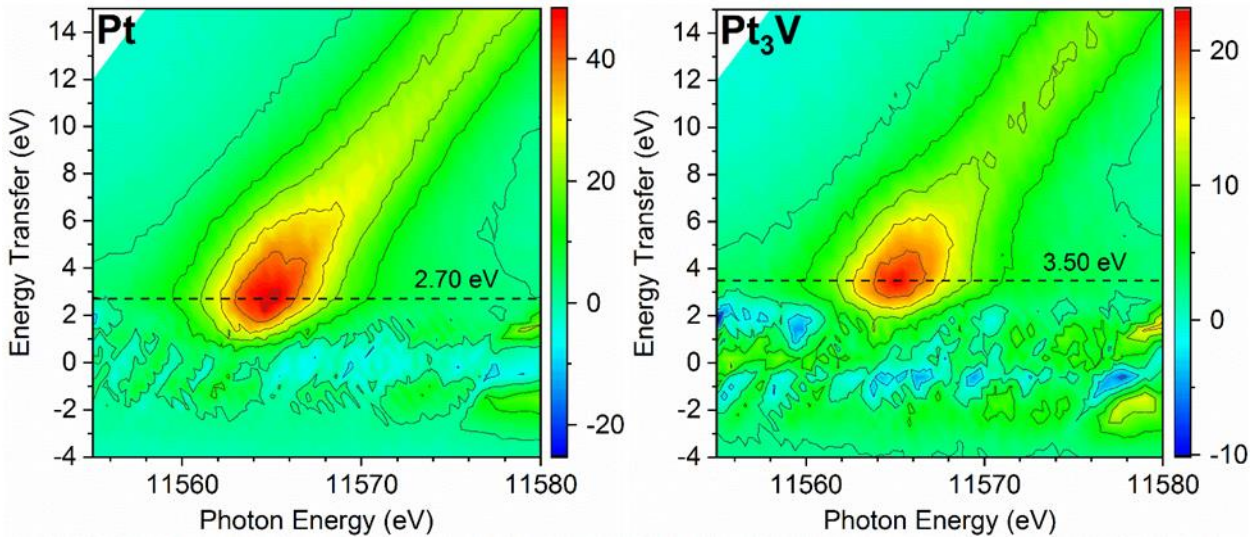

Figure 13: Pt L3-Lβ5 RIXS maps of Pt (left) and Pt3V (right). Spectra were collected after a reduction treatment at 550°C in 3.5% H2 for 30 minutes. Spectra were collected at 100°C in 3.5% H2. Horizontal dashed lines denote the maximum of the inelastic scattering peak for each sample.

RIXS is a two photon spectroscopy where an electron is photoexcited from a core state to a vacant valence state (here a Pt 5d unfilled state) and an emitted photon is measured arising from an electron from the filled valance state (Pt 5d filled state) filling the core hole. To probe the energy of the platinum 5d electrons the $L\beta_5$ emission line, which corresponds to the decay of a 5d electron into a 2p core hole, is selectively measured. RIXS maps are plotted as an intensity map with the incident photon energy on the ordinate and the energy difference between the incident and emitted photon (energy transfer) on the abscissa. When the incident photon is scattered elastically (i.e. the photoexcited 2p electron decays back into the 2p core hole), the fluoresced photon energy is equal to the incident photon energy, which gives a peak at an energy transfer value of zero eV. For clarity, the elastic scattering line has been subtracted from the RIXS plots in figure 13. Intensity fluctuations around an energy transfer value of zero eV are artifacts from the subtraction of the elastic scattering line. Inelastic scattering occurs when the fluorescent decay into the 2p core hole occurs by an electron other than the excited 2p electron. This can occur by any symmetry allowed electron transition according to dipole selection rules. Here the decay of a 5d electron is selectively measured. The inelastic scattering peak manifests as a broad maximum, centered at an incident energy value equal to the respective inflection point of the L_3 edge XANES for each sample. At energy values higher than the XANES inflection

point, the resonant enhancement of the $L\beta_5$ emission mode decays leading to a low intensity tail towards higher energy transfer values with increasing incident energy. For the platinum sample, the maximum of the inelastic scattering peak lies at an incident energy of 11.5640 keV and an energy transfer value of 2.7 eV. This corresponds to an energy separation of 2.7 eV between the average energy of the filled and unfilled states. For Pt_3V, the maximum of the inelastic scattering peak lies at an incident energy of 11.5644 keV, with an energy transfer value of 3.5 eV. The energy separation between the filled and unfilled states in Pt_3V is 0.8 eV larger than Pt. From the XANES edge energy of pure phase Pt_3V the 0.8 eV split can be separated into a 0.4 eV increase in the energy of the unfilled states and a 0.4 eV decrease in the energy of the filled 5d states.

2.4.3 Propane Dehydrogenation

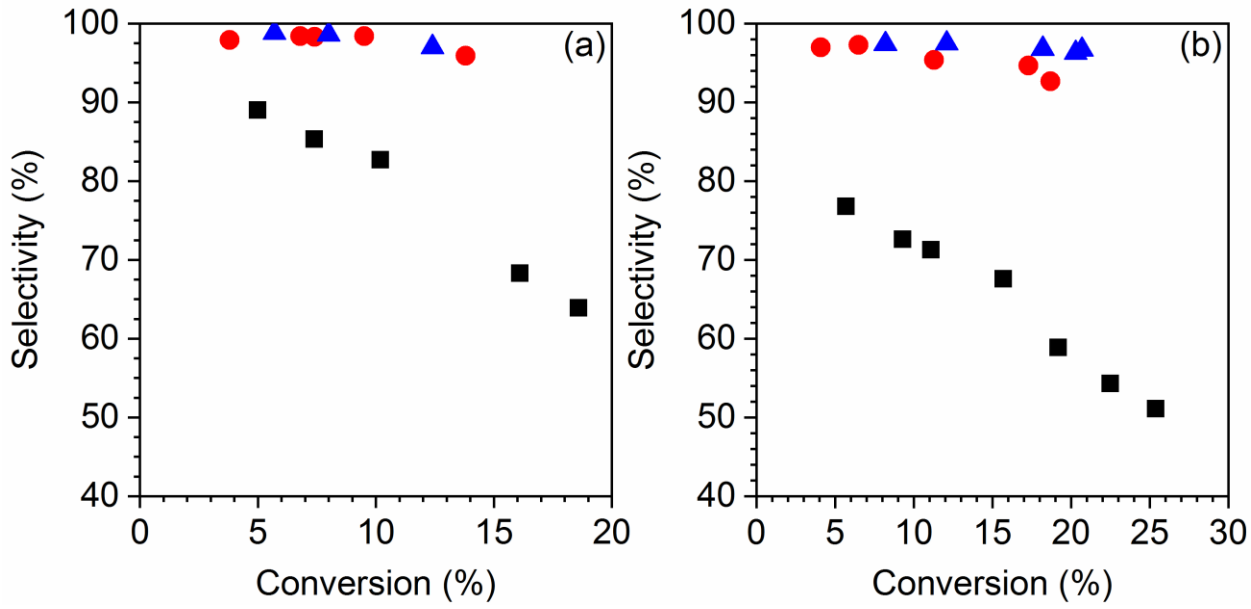

Figure 14: Propylene selectivity and propane conversion for 3Pt (black squares), 5Pt-5V (red circles), and 2Pt-5V (blue triangles) tested without (a) and with (b) cofed H_2. Reactions were performed at 550°C at 3 PSIG with 2.5% propane balance N_2. For plot (b) the hydrogen concentration was 2.5%. Data points shown are at zero deactivation with each data point representing a separate test.

Figure 14 shows propylene selectivity and propane conversion extrapolated to zero deactivation for 3Pt, 5Pt-5V, and 2Pt-5V. For all reactions, propylene was the main product; hydrogenolysis led to the formation of methane, and ethane and ethylene. Tests performed

without co-fed hydrogen are shown in Figure 14a. The selectivity of 2Pt-5V and 5Pt-5V were equivalent in tests without hydrogen, both showing above 95% propylene selectivity which did not decrease with increasing conversion. In comparison, 3Pt showed moderate selectivity which decreased as the conversion was raised.

Figure 14b shows catalyst tests performed with co-fed hydrogen. Dehydrogenation in the presence of H_2 is a more demanding test of the catalysts' selectivity as it is required for hydrogenolysis. The propane to hydrogen ratio was 1:1. Similar to the tests done without hydrogen, 3Pt decreased in selectivity with increasing conversion, but the selectivity at low conversion when tested with hydrogen was lower than when tested without. For the 2Pt-5V catalyst, co-feeding hydrogen did not change the selectivity noticeably from the values obtained without hydrogen. For 5Pt-5V, there was a 4% decrease in the selectivity with increasing conversion over the tested range when hydrogen was co-fed.

To count the fraction of surface platinum in the alloy and properly normalize the propylene production rate, XAS data was collected for each sample in the reduced state and after exposing the sample to air at room temperature. The basis of measuring dispersion by this method comes from the fractional Pt-O coordination arising from surface oxidized platinum. In a particle with 100% dispersion, each Pt(II) ion will have 4 oxygen neighbors (platinum oxide). As the dispersion decreases from unity, the Pt-O coordination number represents the fraction of the sample that is oxidized, and is proportional to the dispersion. By exposing the samples to air at room temperature, the oxidation is limited to the surface layer of the nanoparticle, and the core of the particle remains unchanged between the reduced and oxidized sample. Subtracting the EXAFS of the two samples the signal from the core is eliminated and the remaining spectral features represents the changes to the surface layer between the two samples. Furthermore, the phase shift introduced by subtraction allows for distinction between loss of metallic neighbors and the gain of oxygen neighbors. The same methodology of surface oxidation is the basis of H_2-O_2 titration, but because of the element specificity of EXAFS, the confounding effect of vanadium oxidation on the titration is avoided and additional structural information about the surface can be obtained.

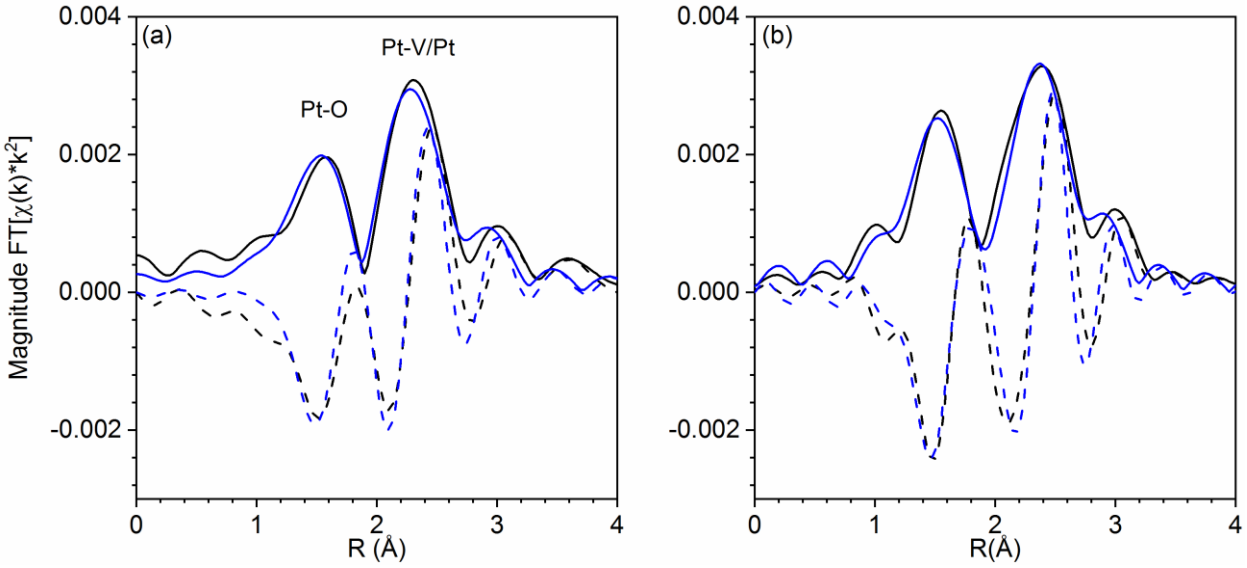

Figure 15: Pt EXAFS difference spectra for 2Pt-5V (a) and 5Pt-5V (b) (magnitude: solid black, imaginary: dashed black) and difference spectra fit (magnitude fit: solid blue, imaginary fit: dashed blue). A reduced scan of both 2Pt-5V and 5Pt-5V was taken at room temperature in He after reduction at 550°C in 3.5% H2, subsequently the samples were exposed to air for 30 minutes and then scanned again.

Figure 15 shows the EXAFS difference spectra for 2Pt-5V and 5Pt-5V, fitting parameters for the difference spectra are given in Table 9. Three peaks are present in the difference spectra. The first peak at low R (at about 1.5 Å phase uncorrected distance) is characteristic of Pt-O scattering. For the 2Pt-5V sample, fitting the peak gave a bond distance of 2.05 Å and a gain in average Pt-O coordination number of 0.5, which corresponds to a dispersion of 0.13. The two peaks between 2-3.5 Å (phase uncorrected distance) are due to lost Pt-Pt and Pt-V scattering. Fitting these peaks in the 2Pt-5V sample gives a Pt-Pt bond distance of 2.72 Å with a coordination number of 0.9 and a Pt-V bond distance of 2.70 Å with a coordination number of 0.6. Within the error of the small features in the difference spectrum, the surface layer Pt-V:Pt-Pt neighbor ratio for 2Pt-5V matches the total sample neighbor ratio.

The 5Pt-5V sample has a Pt-O coordination number of 0.6 at 2.03 Å, corresponding to a dispersion of 0.15. The bond distance for Pt-Pt and Pt-V was 2.74 Å with 1.2 and 0.7 Pt-Pt and Pt-V average coordination numbers respectively, giving a Pt-V:Pt-Pt neighbor ratio close to 0.5. The surface ratio of 0.5 is significantly higher than the total sample neighbor ratio of 0.31, showing that the surface composition in the 5Pt-5V sample is different than that of the total

sample. For both catalysts, the EXAFS difference analysis is consistent with a Pt_3V surface structure.

Table 9: EXAFS fit for Pt-V difference spectra

Sample	Path	CN	R (Å)	σ^2 (Å^2)	E0 (eV)
5P-5V	Pt-O	0.6	2.03	0.002	-4.5
	Pt-Pt	1.2	2.74	0.002	-3.0
	Pt-V	0.7	2.74	0.002	4.4
2Pt-5V	Pt-O	0.5	2.05	0.002	-4.4
	Pt-Pt	0.9	2.70	0.003	2.1
	Pt-V	0.6	2.72	0.003	-3.22

With the Pt dispersion from difference XAS, the propylene production turnover rates were calculated from catalyst test data. Catalyst tests for determining turnover rates were performed differential propane conversion (<10%) at 550°C with a propane concentration of 2.5% and when hydrogen was cofed the concentration was 2.5%. The pure platinum catalyst had a dispersion of 29% and a turnover rate of 0.36 s^{-1} when hydrogen was cofed and 0.03 s^{-1} without hydrogen. The 5Pt-5V catalyst had a dispersion of 15% and a turnover rate of 0.28 s^{-1}, while the 2Pt-5V catalyst had a dispersion of 13% and a higher turnover rate of 0.38 s^{-1}. When tested without hydrogen, 5Pt-5V had an initial TOR of 0.06 s^{-1} and 2Pt-5V had an initial TOR of 0.16 s^{-1}. The small differences between the samples under equivalent conditions are within the error generally assumed for the reproducibility of determining turnover rates [88].

2.4.4 DFT

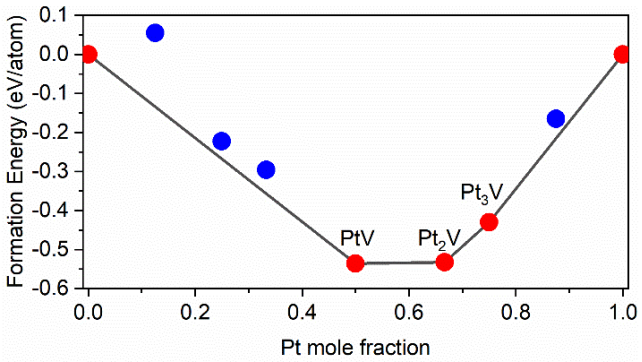

Figure 16: Binary compositional phase diagram for Pt-V. Red nodes are stable phases lying on convex hull. Blue nodes are the most stable phases for given Pt-V compositions which do not lie on the convex hull.

To better understand the electronic effect of vanadium incorporation in platinum when forming Pt_3V alloys, DFT calculations were conducted on model $Pt_3V(111)$ and Pt(111) surfaces. First, compositional phase stability of various Pt-V alloys was studied by constructing an isothermal-isobaric binary compositional phase diagram, shown in figure 16. Contributions from configurational and vibrational entropies are not expected to significantly impact the formation energy of the concerned alloy and hence are not considered. Each point on the plot is the most thermodynamically stable bulk structure for the given composition of Pt-V. The most stable phases are connected through a convex hull and represented by red points. Unstable phases lie above the convex hull (plotted in blue) and would decompose into nearest stable phase on the convex hull, with compositions predicted as per the lever rule. Apart from pure bulk Pt, the Pt_3V phase is the only stable close packed FCC phase. In the in-situ XRD analysis, described above, there is a distinct signature of an FCC phase, suggesting that Pt_3V is the only crystalline bimetallic phase that is present in the prepared sample.

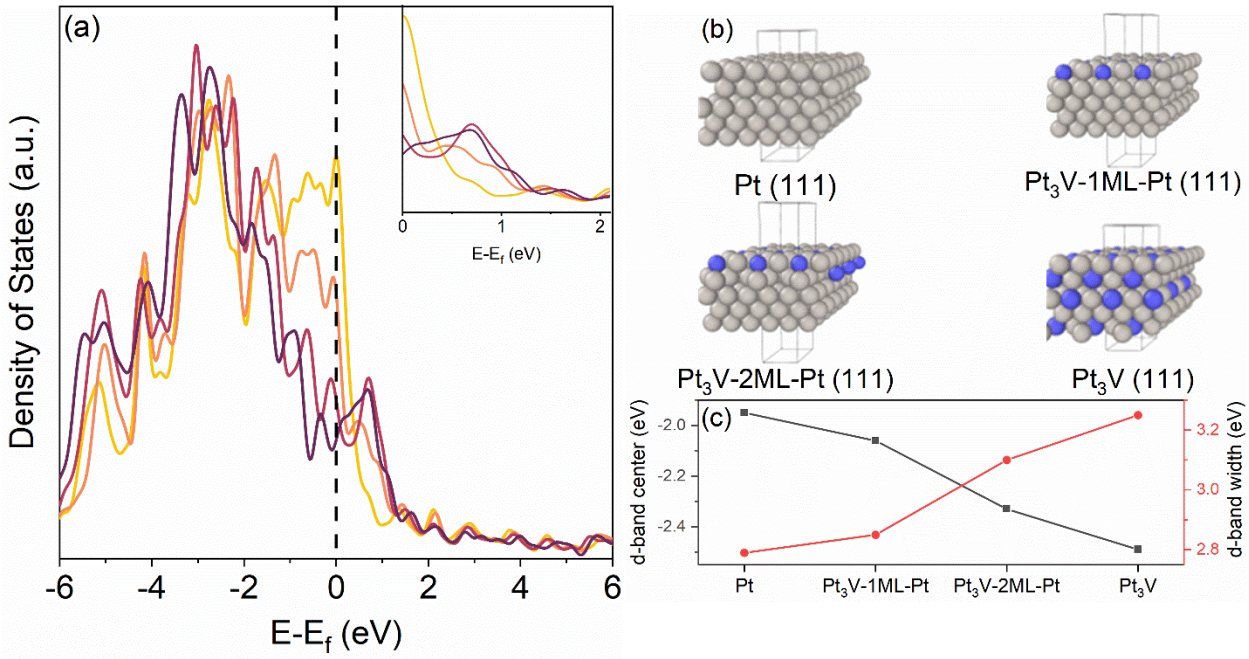

Figure 17: a) pDOS for Pt (gold), Pt_3V (burgundy) and two epitaxial Pt_3V on Pt structures with one (orange) and two (crimson) layers of Pt_3V on Pt with the Fermi energy marked by a vertical dashed line. The inset graph shows an expanded view of near-Fermi energy unfilled states. b) structures corresponding to each model. c) d-band center and d-band width for above structures.

The effect of vanadium incorporation on the platinum electronic energy levels was studied by examining calculated atom projected density of states of the platinum 5d band shown above in figure 17. Four geometries were modeled to represent pure platinum, a core shell structure with two different shell thicknesses, and pure Pt_3V. For modeling of the core shell structures, the top-most and top two layers of a Pt slab were replaced with Pt_3V, labelled as Pt_3V-1ML-Pt and Pt_3V-2ML-Pt respectively. Starting from platinum, replacing subsequent layers of the slab with Pt_3V causes a decrease in the density of states at the Fermi level and the creation of new unoccupied states further from the Fermi level. Pt occupied states broaden and shift to occupy lower energies with increasing V incorporation, with the most significant changes in density concentrated close below the Fermi energy. This shift results in the Pt d-band center decreasing from -1.95 eV for pure Pt to -2.49 eV for bulk Pt_3V. The degree of band filling is nearly constant for all Pt atoms in the surface and bulk alloys studied, suggesting that charge transfer to or from the d band in the system is minimal, in agreement with previous calculations on Pt bimetallics [29], [33].

Table 10: Binding energies of CO and CH_3 on Pt (111), Pt_3V-1ML, Pt_3V-2ML and Pt_3V (111). Binding energies were calculated according to equation 3 and 4.

System	Bindng energy (eV)	
	CO	CH_3
Pt (111)	-1.78	0.38
Pt_3V-1ML-Pt	-1.72	0.41
Pt_3V-2ML-Pt	-1.56	0.59
Pt_3V (111)	-1.60	0.62

$$\mathrm{BE_{CO}} = \mathrm{E_{CO+Slab}} - \mathrm{E_{slab}} - \mathrm{E_{CO(g)}} \tag{3}$$

$$\mathrm{BE_{CHx}} = E_{CHx+slab} + \frac{x}{2}E_{H2(g)} - E_{slab} - E_{CH4(g)} \tag{4}$$

The consequences of d band modification from V incorporation can be seen in the weakening of binding energy of CO and CH_3 as the alloy layer thickens (see table 10). For a single monolayer, the change from platinum is less than the typically assumed error in DFT of 0.1 eV. When the layer thickness is increased to two monolayers, CO and methyl both decrease in binding strength by about 0.2 eV, within error matching the binding energy values for the pure Pt_3V slab.

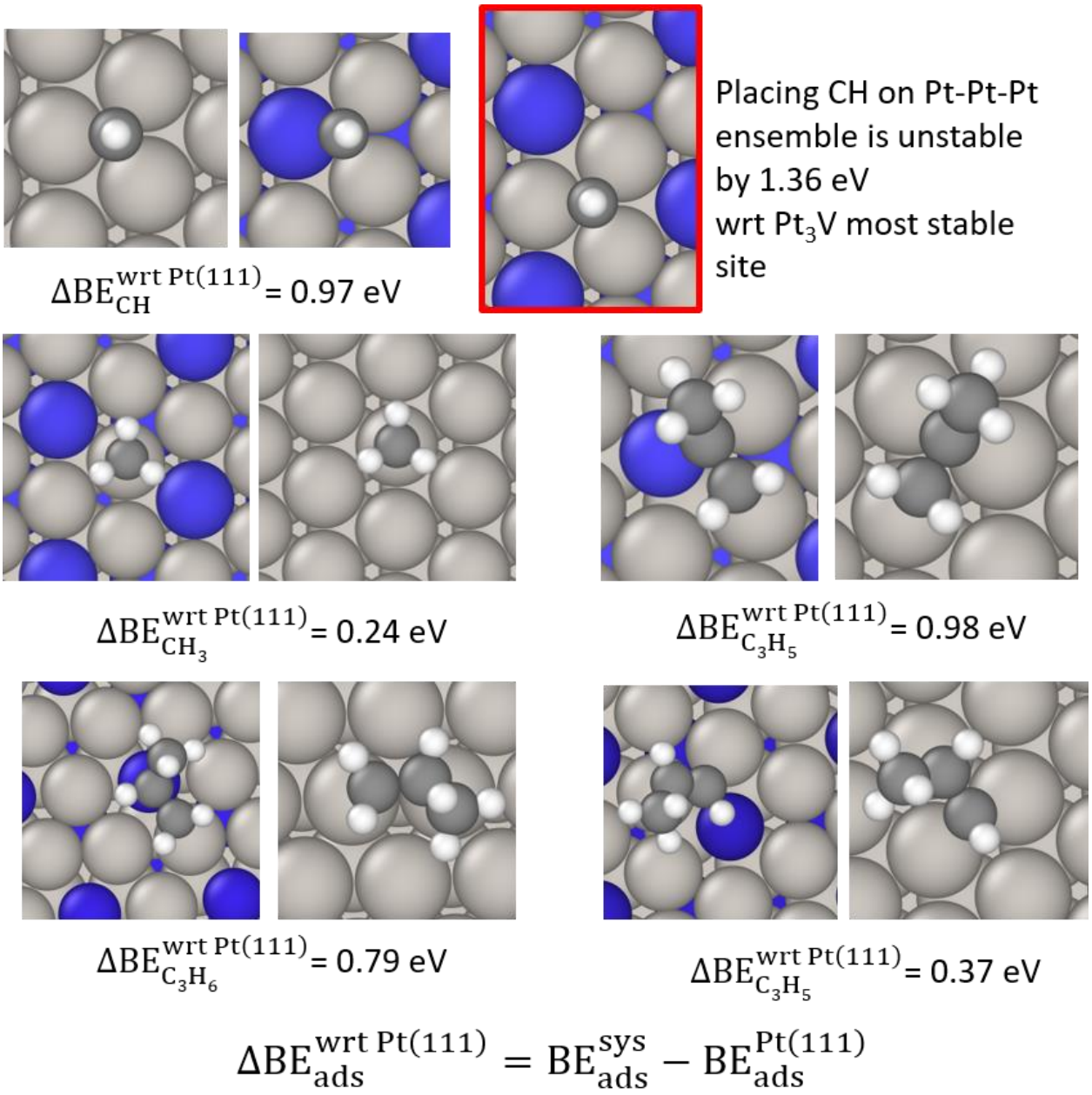

Figure 18: Schematics of binding configurations and their corresponding binding energies (with respect to Pt (111)) for CO, C_1, C_2 and C_3 hydrocarbon fragments on Pt_3V (111) and Pt (111) surfaces.

Table 11: Most stable binding configurations and their corresponding binding energies for CO, C_1, C_2, and C_3 hydrocarbon fragments adsorbed on Pt (111) and Pt_3V (111) surfaces.

Species	Most stable binding location on:		Binding energy relative to Pt (111) (eV)
	Pt_3V (111)	Pt (111)	
CO	Pt_{top}/V_{top}	FCC/HCP	0.19
CH	HCP/FCC (PtPtV)	FCC/HCP	0.97
CH_2	HCP/FCC (PtPtV)	Pt bridge	0.51
CH_3	Pt_{top}	Pt_{top}	0.24
C-CH_3	FCC (PtPtV)	FCC	0.67
CH_3-CH-CH_2	PtV bridge	Pt bridge	0.79
CH_3-CH-CH	HCP (PtPtV)	FCC	0.37
CH_3-C-CH_2	PtV bridge-Pt_{top}	Pt bridge-Pt_{top}	0.98

Table 11 shows the binding energy and corresponding binding sites on Pt_3V (111) and Pt (111) surfaces for CO, C_1, C_2 and C_3 fragments. The effects of electronically modifying platinum by alloying are seen on the binding energetics of important intermediates which have been used to model propane dehydrogenation and coking networks [44]–[46]. All the intermediates modeled show weaker binding on Pt_3V (111) compared to Pt (111). CH, CCH_3, and CH_3CCH_2 intermediates bind 0.97 eV, 0.52 eV, and 0.67 eV more weakly on Pt_3V compared to Pt. Additionally, Pt-Pt-Pt ensembles on Pt_3V are unstable compared to Pt-Pt-V 3-fold sites as seen from adsorption of CH and $CHCCH_2$ (see figure 18). Hydrogen binds equally as strong on the HCP site on Pt and Pt_3V, where the HCP site is a Pt-Pt-V ensemble. In contrast to Pt, all Pt_3V surface sites no longer isoenergetically bind H as shown in table 12.

Table 12: H binding energy on Pt (111) and Pt3V (111) references to H2 gas.

Pt (111) binding site	Binding energy (eV)	Pt3V (111) binding site	Binding energy (eV)
Pt top	-0.48	Pt top	-0.25
FCC	-0.44	V top	0.25
HCP	-0.48	HCP (Pt-Pt-V)	-0.43
Bridge	-0.44		

Table 13: Binding energies of CO and CHx species calculated on Pt_3V (111) and Pt (111) with the lattice constant of Pt_3V. The effect of changing the lattice constant of Pt (111) is minimal on the binding energy compared to the Pt slab constructed using the equilibrium lattice constant.

Species	Binding Energy relative to Pt(111)	
	Pt with Pt_3V lattice constant	Pt_3V
CO	0.08	0.19
CH	0.09	0.97
CH_2	0.07	0.51
CH_3	0.07	0.24

The contribution of surface strain to the binding energy changes observed was evaluated by fixing the Pt lattice constant to that of Pt_3V and recalculating the adsorption energies. The effect is caused due to the Pt-Pt distance decreasing from 2.81 to 2.77 Å when vanadium is incorporated into the lattice. In all cases, the change in binding energy was within the error of DFT (see table 13), demonstrating the preeminence of V in the modification of binding energies in the alloy even in cases where the adsorbate does not directly adsorb to a vanadium containing site.

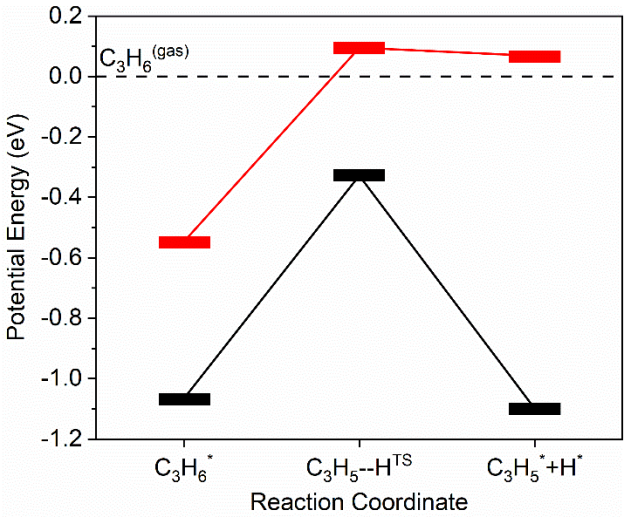

Figure 19: Calculated C-H bond breaking energy for adsorbed propylene on Pt (111) (solid black) and Pt_3V (111) (solid red) referenced to gas phase propylene (dashed black).

A frequently used descriptor for selectivity of dehydrogenation is the energy difference between the first deep dehydrogenation step and the desorption energy for propylene [46]. The barrier for C-H bond cleavage in adsorbed propylene, shown in figure 19, are similar on Pt and Pt_3V (111) surfaces. They differ by only about 0.1 eV, with the transition state on Pt_3V being

higher in potential energy. However, there is appreciable difference in the stability of transition state (TS) with respect to the desorbed gas phase C_3H_6: the TS for Pt is 0.32 eV more stable than desorbed propylene while for Pt_3V the TS is 0.09 eV unstable. This suggests that for modeled (111) surfaces of Pt_3V the thermodynamics of desorbing and bond-breaking are competitive but for Pt (111) the deep dehydrogenation pathway is favorable.

2.5 Discussion

2.5.1 Structural Model

There are several possibilities for the arrangement of platinum and vanadium in a bimetallic nanoparticle. The bulk Pt-V phase diagram lists five stable phases: Pt_8V, Pt_3V, Pt_2V, PtV, and PtV_3. Pt can form a solid solution with V, but the solubility (which decreases with temperature) is limited to 15 at% V at 400°C [89]. From the isothermal-isobaric phase diagram, Pt_3V, Pt_2V and PtV were identified as thermodynamically stable phases.

The primary reflections in XRD of the 5Pt-5V sample rule out the non-cubic, non-face centered Pt-V phases which include Pt_8V, Pt_2V and PtV. The $AuCu_3$ form of PtV_3 can be ruled out based on the presence of Pt-Pt nearest neighbors seen in EXAFS which would not be present in PtV_3. Because both a solid solution and Pt_3V with the $AuCu_3$ crystal structure have the same symmetry distinguishing between them by XRD without super lattice diffraction peaks, especially in small nanoparticles, is difficult. Since vanadium makes up nearly a third of the total number of neighbors by EXAFS, it is unlikely that the nano-particle structure is a solid solution. A solid solution would also have a homogeneous composition throughout the particle, but the 5Pt-5V sample has a vanadium rich surface, as measured by difference XAS, relative to the total particle composition. The peak asymmetry in the XRD reflections of 5Pt-5V calcined at 450°C and 500°C cannot be explained by a solid solution, which would be expected to have symmetric peaks with a position governed by Vegard's law. Fitting the 220 reflection (figure 10) shows that the peak position of both Pt and Pt_3V remain unchanged for different particle compositions as would be expected for a phase mixture. As the calcination temperature increases from 450°C to 500°C, the Pt peak component increases in relative intensity and FWHM but does not shift and the peak shoulder decreases in relative intensity but also remains in the same position. As the vanadium incorporation decreases, the Pt_3V surface layer on the growing platinum core becomes

a smaller fraction of the nanoparticle composition, which can be seen in the decrease and ultimately the disappearance of the high 2θ shoulder as the calcination temperature is raised from 450°C to 600°. Consistent with the XRD, EXAFS shows that Pt-V:Pt-Pt neighbor ratio decreased and the total coordination number increased, showing that as the calcination temperature is raised, the particles get larger and more platinum rich. This model is consistent with the DFT calculated phase diagram where compositions intermediate between Pt and Pt_3V would be expected to decompose into the two phases. At the highest calcination temperature, EXAFS results still show the presence of V neighbors (see table 3), but diffraction from the large Pt particles dominates the diffraction signal from the small fraction of Pt_3V. Thus, by the process of elimination, the alloy phase is Pt_3V with the $AuCu_3$ crystal structure. This result is also fully consistent with DFT calculations showing that Pt_3V is a stable bulk alloy on the Pt:V convex hull.

Further understanding of the arrangement of the Pt and Pt_3V phases can be gained through comparison of the total and surface XAS Pt-Pt:Pt-V neighbor ratios. The atomic environment of platinum in the Pt_3V phase is cuboctohedral with 8 platinum neighbors and 4 vanadium neighbors, both at a bond distance of 2.74 Å. As the particle size decreases, the total coordination number and bond distance both decrease, but the ratio of vanadium to platinum neighbors will remain constant between nano-phase and bulk Pt_3V because of the local Pt environment inherent to the phase. Thus, the Pt-Pt and Pt-V coordination numbers can be used to determine if a sample has a stoichiometry consistent with the Pt_3V phase.

For the 5Pt-5V sample, the Pt-V:Pt-Pt neighbor ratio is lower than bulk Pt_3V, indicating that the sample is platinum rich with respect to Pt_3V. The platinum enrichment in 5Pt-5V could take two forms: the sample could have unalloyed Pt particles, or the particles could be Pt_3V/Pt (or vice versa) core/shell particles. Surface oxidation difference XAS on the 5Pt-5V sample shows that they have, within error, the same surface stoichiometry as Pt_3V, which is consistent with a Pt_3V/Pt core shell particle. Since Pt-V scattering arises from the formation of Pt_3V, the Pt-Pt coordination number can be separated into Pt-Pt coordination in the alloy and Pt-Pt coordination in the platinum core, as the ratio of Pt-V to Pt-Pt in the alloy is fixed at 0.5. This allows for the fraction each phase to be derived from the total coordination number. For 5Pt-5V, the Pt-V coordination number of 2.0 gives a total Pt_3V coordination of 6 (2Pt-V + 4 Pt-Pt); the total coordination of 8.5 gives an alloy phase fraction of 70% and and a Pt core phase fraction of

30%. Given the volume average particle size (2.2 nm) and lattice parameter (3.88 Å), the alloy shell layer thickness can be estimated as in reference [90], giving a shell layer thickness of 4 Å on a core 14 Å in diameter. A 4 Å shell layer corresponds to approximately 2-3 atomic layers of alloy.

In the 2Pt-5V sample, the Pt-V:Pt-Pt neighbor ratio matches bulk Pt_3V. Based on the XRD results for 5Pt-5V the interpretation most consistent with the EXAFS would be that the 2Pt-5V samples is pure phase Pt_3V. The surface oxidation difference EXAFS data shows that the surface stoichiometry also matches that of Pt_3V and thus demonstrates that no surface segregation occurs under the reducing conditions. Additionally, the surface EXAFS suggests that there are few, if any, unalloyed Pt nanoparticles in this sample

Lowering the platinum loading from 5% to 2% weight increased the degree of vanadium incorporation despite the fact that, in the 5Pt-5V sample, vanadium is present in approximately a 12-fold excess of what is required for all the Pt present to form the Pt_3V phase. In spite of the large excess, the metallic particles in 5Pt-5V are platinum rich due to the way in which vanadium disperses on silica. Vanadia and silica are both acidic oxides and interact poorly. Unlike other oxides, vanadium does not form 2d layers on silica, instead going from single sites straight to small vanadia crystallites [91]. The effect of calcination temperature after platinum impregnation on both the particle size and vanadium incorporation can be seen in the series of 5Pt-5V samples calcined at different temperatures. When the calcination temperature is increased, both the platinum oxide and vanadium oxide clusters agglomerate, which after reduction results in larger Pt particles [82]. The agglomeration of vanadium oxide has the secondary effect of reducing the amount of platinum that is then in intimate contact with vanadium, resulting in less vanadium incorporation. Both factors lead to large platinum particles with vanadium incorporation taking the form of a Pt_3V shell layer of decreasing thickness in the 5Pt-5V samples calcined above 250°C, as can be seen by the decrease in the Pt-V:Pt-Pt coordination number ratio.

2.5.2 Nature of Electronic Modification

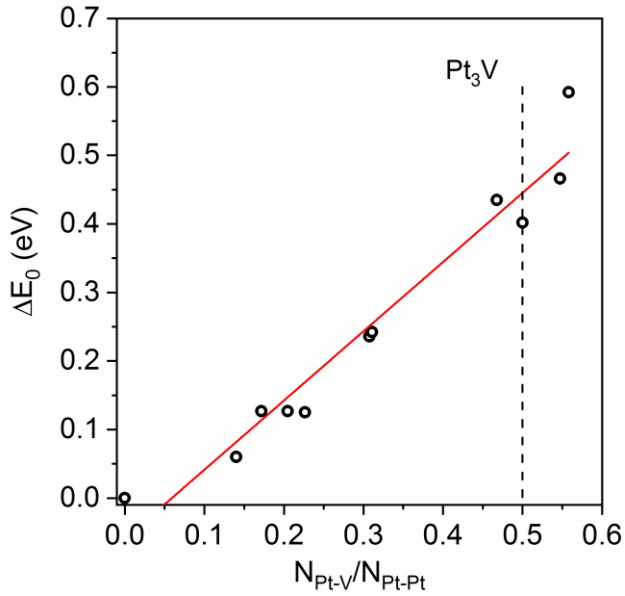

Figure 20: Pt L_3 edge XANES shift (vs. Pt foil) plotted against the ratio of Pt-V to Pt-Pt coordination numbers for 3Pt and 10 Pt-V catalysts. The Pt-V to Pt-Pt ratio for the bulk Pt_3V phase is shown as a vertical dashed line. A linear fit of the data is shown in red.

Figure 20 shows the correlation between the shift in the Pt L_3 XANES energy for Pt-V catalysts and the Pt-V/Pt-Pt neighbor ratio. EXAFS fits and XANES energies for the samples in figure 20 are given in tables 2, 3, 4, and 6. As the neighbor ratio increases (increasing vanadium content) the edge energy increases. Increases in the XANES edge energy indicate an increase in the average energy of the platinum 5d unfilled states, which is also seen by RIXS. The correlation shows that the magnitude of the electronic change increases as the vanadium content in the nanoparticle increases, which suggests that vanadium neighbors are responsible for the changes in the energy of the platinum 5d unfilled states. The linear relationship between the XANES edge energy and the neighbor ratio reflects the change in the fractions of Pt_3V and Pt present. It also demonstrates the importance of phase purity in determining the true magnitude of an electronic change due to alloy formation. From figure 20, the true shift in the XANES edge energy of a Pt_3V pure phase alloy which has the 2:1 neighbor ratio is 0.4 eV, demonstrating that the energy of the unfilled Pt 5d orbitals in Pt_3V are 0.4 eV higher than in Pt nanoparticles.

Frequently in the metal catalysis literature, the rigid band model is invoked to describe the mechanism of electronic modification of catalysts [30], [32], [35], [92], [93]. This model has

been successfully used to describe thermal and electronic properties of alloys, which are properties dominated by conduction band s and p electrons, whereas in metal catalysis the localized d electrons are responsible for catalytic behavior [94]. In the rigid band model, when two elements of different electronegativity are combined in an alloy, the atom with lower electronegativity transfers electron density to the other [95], [96]. This further fills the d band, shifting the Fermi energy to higher energy while the shape of the density of states remains constant. The model of charge transfer has been extend to describe electronic changes not only in alloys [30], [32], [51], but also nanoparticle-support interactions [97], and particle size effects [98]. These observations of electronic modification are based on spectral changes seen in various techniques sensitive to valence d electrons such as XPS, XANES, and ELNES, among others. Using this model, one could predict the direction and magnitude of electron transfer for a given alloy, and hence the spectral changes in XPS, XANES and RIXS. If electron transfer accurately describes the mechanism of electronic modification of platinum, the direction of charge transfer predicted should be consistent among these methods.

XPS binding energy shifts are frequently used demonstrate electronic modification resulting from alloying. The interpretation of XPS shifts in alloys is complicated due to the sensitivity of core level binding energies to particle size, chemical environment (initial state effect), the screening character of the valence electrons (final state effect), and changes in the position of the Fermi level which is the binding energy reference. The potential model of XPS is frequently invoked to describe XPS core level shifts between pure metals and alloys [99]. In this model, the initial state effect is due to a change in the electrostatic potential in the ground state between pure element and the alloy. This change in potential has been related to a difference in electron density between the two environments. If charge is removed from the atom, more energy is required to remove an electron from a more cationic atom and vice versa. The final state effect has intra-atomic and extra-atomic components and is caused by a change in the screening character of the valence electrons and a change in the electrical conductivity of the metal respectively. If one were to attribute a part, or the entirety of the 0.4 eV core level shift measured for 2Pt-5V to an initial state effect, the increase in binding energy by the above model would mean that platinum in Pt_3V has lost electrons through electron transfer to vanadium.

Because the Pt L_3 edge XANES transition probability is proportional to the number of unfilled states, changes in the intensity and broadness of the XANES white line can be attributed

to changes in the density of Pt 5d unfilled states [100], [101]. The rigid band model has also been used to describe these spectral changes in the XANES [32], [96]. In this interpretation, the transfer of electron density to platinum decreases the number of unfilled Pt 5d states leading to a lower white line intensity. Additionally, due to the increased filling of the d-band resulting from the electron transfer the average energy of the unfilled states increases which causes an increase in the XANES edge energy. By the above model, the 0.4 eV increase in XANES edge energy seen for Pt_3V would mean that platinum in Pt_3V has gained electrons through electron transfer from vanadium, which is the opposite conclusion reached using the same model to interpret XPS core level shifts.

While XANES and XPS allow for an indirect measurement of the d band, RIXS is a direct measurement of the filled d states responsible for adsorbate bonding. The inelastic scattering peak in RIXS represents the energy difference between the weighted average energy of the filled and unfilled states. By the rigid band model, any change in filling of the d band would shift the average energy of the filled and unfilled states in the same direction. Hence, the separation in energy between the filled and unfilled states should be similar regardless of any electron transfer. Based on the separately collected XANES spectrum, the energy transfer value can be deconvoluted into a downward shift in the filled state energy and an upward shift in energy of the unfilled state energy, which cannot be explained by electron transfer.

The inconsistency between the predicted direction of electron transfer in XPS, XANES and the increased separation energy between the filled and unfilled states by RIXS suggest that the rigid band model and electron transfer between Pt and the promoter atom is incorrect. For Pt and Pt_3V, the density of states calculations demonstrate that the alloy does not follow rigid band behavior. Instead, the d-band of Pt_3V is broadened with respect to Pt, resulting in changes the energy of the filled and unfilled 5d states. These energy changes are consistent with the spectral changes observed by XPS, XANES and RIXS. For example, the broadening of the d band causes the d-band center to shift away from the Fermi level, decreasing the average energy of the filled states, consistent with the RIXS results. The unfilled Pt 5d states also increase in energy due to the broadening of the band, resulting in an increase in the XANES energy in Pt_3V. Despite this modification in the density of states, the filling of the d band (and hence number of d electrons) remains constant as shown by the integration of the d band density of states for platinum and

Pt_3V. Thus, it is a change in the energy of the filled and unfilled d states that gives rise to the changes in the XPS, XANES and RIXS spectra of Pt_3V.

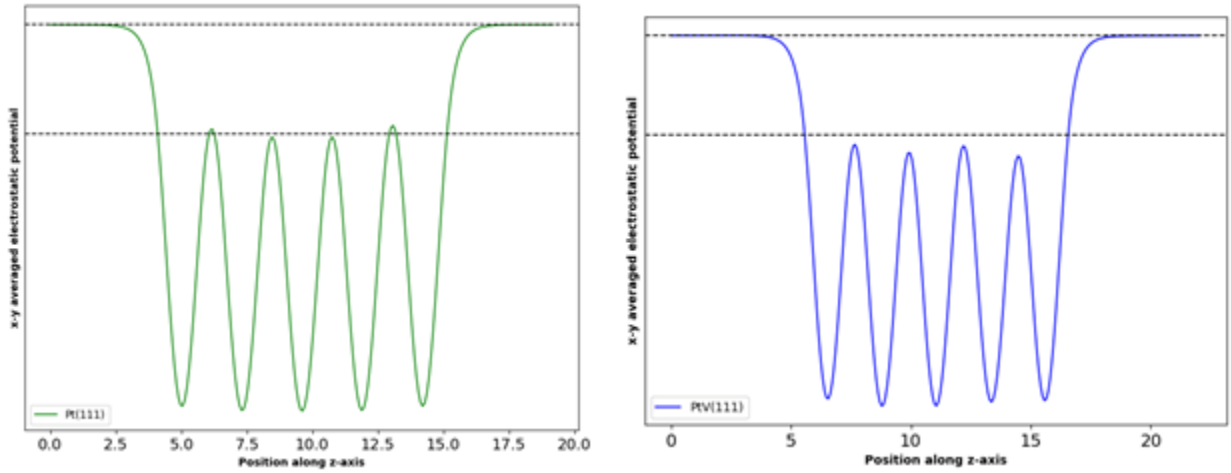

Figure 21: X-Y averaged electrostatic potential for Pt(111) and Pt3V (111) slab plotted along the Z-axis (perpendicular to the slab surface)

Table 14: Work function values for the (111) face of Pt and Pt3V.

	Pt (111)	Pt_3V (111)	Difference
Work function (eV)	5.68	5.27	0.41

While XPS shifts are often interpreted as due to initial state effects, core level shifts have been shown to move in the same direction as the valence band center as measured by valence band photoelectron spectroscopy, indicating a correlation between energy changes in the valence band and core level shifts (CLS) [102], [103]. Therefore CLS in alloys cannot be explained solely by the initial state effect or a transfer of electrons from one element to another, and the final state effect must also be considered [104], [105]. The calculated work function of the Pt and Pt_3V (111) surface (see figure 21 and table 14) are also different, which shows that changes in the fermi level between the two cannot be neglected as contributing to the core level shift. It has been demonstrated that the CLS in alloys may be due to the intra-atomic charge redistribution in the valence band [103], [106]. The 0.4 eV CLS for the 2Pt-5V catalyst is consistent with a shift of the d-band center away from the Fermi level caused by the redistribution of energy states in the d-band in agreement with DFT and RIXS. The present work on Pt_3V further demonstrates why assuming core level shifts are dominated by an initial state effect, or even that the core level

shift occurs in the same direction as the initial state effect is not a safe assumption. Theoretical calculations of core level shifts in alloy systems as a function of composition by the complete screening model show in many systems, such as Pd-Ag, that the final state effect is non-negligible and that initial state effect shift and total CLS do not have the same sign [103]. Further, the initial state effect shift of both components in an alloy do not always occur in opposite directions as would be expected in all cases if electron transfer explained the cause of the initial state effect for alloys[107].

Another consequence of non-rigid band behavior can be seen in the L_3 edge XANES of Pt_3V, where the white line increases in intensity and narrows compared to a platinum nanoparticle of the same size. Pt-Mo alloys also have a white line intensity higher than a similarly sized platinum nanoparticle despite Mo also being less electronegative than platinum [84], [108]. In the other direction gold-platinum alloys, where platinum is the more electropositive element have a Pt white line intensity is lower than that of the platinum foil and the XANES edge energy is shifted to a value higher than Pt [79]. The increase in XANES edge energy and white line intensity, therefore are not necessarily indicative of increased oxidation state, or electron transfer from Pt, as is often suggested. What is generally neglected in the interpretation of the white line intensity is that the broadness of the white line also changes. Thus, a small, broad white line can have the same area (and hence number of unfilled states) as a narrow, large white line. These changes reflect changes in the energy distribution of unfilled states (as seen in the d band DOS for Pt and Pt_3V), not necessarily the loss of states due to electron transfer. This was demonstrated by Schweitzer et al. based on the integrated area of experimental and calculated Pt L_3 edge XANES of platinum and platinum alloys [33]. The same conclusion was reached in nickel containing alloys using energy loss near edge structure (ELNES) and auger electron spectroscopy (AES) by Nikolla and coworkers [34].

The changes in energy of the filled and unfilled states originate from the formation of metallic bonds between platinum and vanadium which is reflected in the density of states and RIXS spectra of Pt and Pt_3V. Formation of a molecular orbital from the overlap of Pt 5d and vanadium 3d orbitals leads to the formation of filled and unfilled states shifted in energy compared to pure platinum. The shape of the white line reflects the changes in the shape of the unfilled Pt density of states resulting from alloy formation. The bonding states in a Pt-V bond are

also different in energy as compared to the Pt-Pt bonding states. This has the effect of broadening the d-band which results in the d band center shifting away from the Fermi level.

The consequence of these electronic effects can be seen in decrease in binding strength of adsorbates on alloys vs. pure platinum surfaces as seen in the electronic structure calculations shown in table 11. All the model adsorbates considered including CH_x, CCH_3, C_3H_5, and C_3H_4 showed weakening in binding energy compared to their binding strength on pure Pt. Because alloying decreases the average energy of the filled 5d states, the binding strength of adsorbates weakens as predicted by d-band theory [28]. It has been proposed that this weakening of adsorption strength leads to the desorption pathway being favored over deep dehydrogenation in DFT studies of platinum tin alloys [44]. As seen from figure 19, a similar conclusion can be drawn for Pt_3V since the thermodynamics of deep dehydrogenation vs desorption are competitive in case of Pt_3V while for monometallic Pt the deep dehydrogenation is clearly thermodynamically favored.

2.5.3 The effect of Structure on Catalytic Performance

The electronic effect occurs as a result of bonds between the active metal and the promoter. Due to this nature, electronic modification is a necessarily short range effect, as demonstrated by surface platinum density of states, which showed a large change when first nearest neighbors were changed, as compared to the small change which occurred between the two monolayer slab and the full alloy where only second nearest neighbors are changed. Unlike solid solution bimetallics, intermetallic compounds have fixed atomic positions within the unit cell. Thus, the atomic plane and crystal structure determines the number of metal-promoter bonds that surface atoms have and the active metal ensemble size. Whereas a solid solution bimetallic of the same composition will have a distribution of ensemble sizes and metal-promoter bonds. This leads to a distribution of electronic modification in solid solutions even with significant promoter content. The consequence for dehydrogenation selectivity in solid solutions is that they only show dehydrogenation selectivity comparable to intermetallic compound catalysts at very high dilutions where the active metal exclusively or close to exclusively heteroatomic bonds [22], [23].

The geometric effect, or the decreasing the active metal ensemble size, requires the presence of the promoter metal in the surface layer of the nanoparticle. Difference XAS spectra

on Pt-V alloys demonstrates that vanadium is present in the surface layer. The geometric effect is often cited as the dominant factor in dehydrogenation selectivity in alloys where the active metal is isolated [24], [26], [48]. However, in the case of Pt_3V, the (111) surface is composed of interconnected groups of 3 platinum atoms. Despite the lack of total platinum isolation Pt_3V still shows above 95% propylene selectivity, which suggests that total platinum isolation is not a requirement for high dehydrogenation selectivity. This conclusion is supported by DFT results, which show that Pt_3V alloys bind C_2 and C_3 intermediates more weakly on sites of different geometry as compared to pure Pt, in spite of the presence of 3 fold Pt sites geometrically equivalent to Pt on the Pt_3V surface.

It is also worth mentioning that mechanisms proposed for the hydrogenolysis of alkanes vary in the number of metal sites required for the reaction from two to more than four [14], [109]–[111]. DFT studies on various metals have shown that the barrier for C-C bond cleavage lowers as more hydrogen atoms are removed from the adsorbed hydrocarbon [112]. Based on these results the mechanism for hydrogenolysis is suggested to occur through a deeply dehydrogenated species. For every hydrogen lost to dehydrogenation, the C-H bond is replaced by a metal-carbon bond [20]. Thus, the extent of dehydrogenation at which hydrogenolysis occurs determines the number of active metal atoms needed to catalyze the reaction. Even assuming the high-end ensemble size requirements for hydrogenolysis (4+ atoms), the (111) surface of Pt_3V should still have a large enough active metal ensemble to catalyze hydrogenolysis. A reason that these sites, which are important for stabilization of coke precursors on platinum [113], do not cause low selectivity in Pt_3V may be due to the decreased binding strength and change of binding geometry of coke precursors shown in figure 17 and table 11. The surface and subsurface vanadium atoms proximal to the 3-fold site electronically modify platinum destabilizing adsorption on this site.

The 5Pt-5V sample, which has a Pt_3V surface 2-3 monolayers thick on a Pt core, has a high propylene selectivity similar to that of 2Pt-5V which is Pt_3V full alloy. This demonstrates that only the formation of a continuous surface layer of intermetallic compound is necessary for high dehydrogenation selectivity. The same phenomena has been reported for Pt_3Mn alloys in propane dehydrogenation, where the formation of a continuous surface layer Pt_3Mn and a full alloy both led to high propylene selectivity and weaker adsorbate binding, with the Pt_3Mn/Pt core shell catalyst showing lower selectivity when tested with cofed hydrogen [114]. From an

electronic effect standpoint, it is unsurprising that a 2 monolayer thick alloy surface shows similar selectivity to a full alloy, as the surface Pt density of states for both models are very similar and the nearest neighbors of the surface Pt atoms are the same in both cases. To more definitively show the predominance of geometry or electronic effects in driving dehydrogenation selectivity, it may be necessary to synthesize a catalyst with a single monolayer of alloy on a monometallic core. Regardless of the layer thickness the geometric effect of the promoter is the same, but the electronic effect between a 1 monolayer and 2 monolayer surface alloy catalyst would be clearly different as the nearest neighbors of surface platinum would be modified by subsurface promoter between the two catalysts. Regrettably this level of synthetic control was not possible by the methods explored in the present study, however it may be possible using atomically precise or self-limiting synthesis methods such as atomic layer deposition or epitaxy [115], [116].

2.6 Conclusion

The addition of vanadium to a platinum catalyst leads to the formation of the Pt_3V intermetallic compound with the $AuCu_3$ structure. The alloy forms during reduction by the sequential formation of platinum nanoparticles and subsequent reduction proximal vanadium oxide to form the alloy phase. This is evidenced by the comparatively low temperature required to form metallic vanadium when compared to the reduction of vanadium oxide without platinum. The formation of the Pt_3V phase, or an alloy surface layer on a Pt core, led to high propylene selectivity demonstrating that total platinum site isolation, and full alloy formation, is not required for high dehydrogenation selectivity. Formation of the ordered alloy phase ensures that all platinum atoms in the nanoparticle experience similar electronic modification and that large platinum ensembles are eliminated. Other unexplored alloys with the $AuCu_3$ structure may also show high dehydrogenation selectivity based on the high selectivity of both Pt_3Sn and Pt_3V despite very different bonding interactions between platinum and the promoting element. The magnitude of the electronic modification was shown to be dependent on the extent of alloy formation, demonstrating the importance of phase purity in determining the electronic modification inherent to a specific alloy phase. The source of electronic modification in platinum-vanadium alloys is not caused by electron transfer to, or from, the platinum 5d orbitals, but rather a change in the energy of the orbitals. The consequences of the electronic modification

were shown by DFT to be weakening of adsorbate bonding to platinum and changes in the most stable binding geometries in the alloy.

2.7 Acknowledgemnets

This paper is based upon work supported in part by the National Science Foundation under Cooperative Agreement No. EEC-1647722. Use of the advanced photon source was supported by the U.S. Department of Energy, Office of Basic Energy Sciences, under contract no. DE-AC02-06CH11357. MRCAT operations, beamline 10-BM and 10-ID, are supported by the Department of Energy and the MRCAT member institutions. The authors also acknowledge the use of the 11-ID-C beamline at the advanced photon source. XPS data was collected at the Surface Analysis Facility of the Birck Nanotechnology Center of Purdue University. Use of the Center for Nanoscale Materials (CNM), a U.S. Department of Energy, Office of Science, Office of Basic Energy Sciences User Facility; Information Technology at Purdue (West Lafayette, Indiana), and computational resources from the National Energy Research Scientific Computing Center is gratefully acknowledged. This material is based upon work supported, in part, by the U.S. Department of Energy Office of Science, Office of Basic Energy Sciences, Chemical Sciences, Geosciences, & Biosciences (CSBG) division. The authors acknowledge Joseph Kubal, Brandon Bukowski and Siddharth Deshpande for valuable discussions.

3. TESTING THE PREDICTIVE POWER OF A DEHYDROGENATION SELECTIVITY DESCRIPTOR IN PALLADIUM ALLOYS CATALYSTS WITH DIFFERENT STRUCTURES AND PROMOTERS

This chapter is composed of a manuscript currently under revision for publication.

3.1 Abstract

In this paper we show the synthesis and propane dehydrogenation performance of a series of palladium and palladium alloy catalysts. Alloy phases between Pd and Zn, Ga, In, Fe and Mn were verified using in-situ X-ray absorption spectroscopy (XAS) and synchrotron X-ray Diffraction (XRD). Electronic modification of the alloy catalysts was demonstrated using Pd L_3 edge X-ray absorption near edge structure (XANES), which showed a redistribution in energy of the Pd 5s unfilled density of states. The alloys all showed dehydrogenation turnover rates close to an order of magnitude higher than the monometallic Pd catalysts, and selectivities to propylene over 90%. Binding energies, C-H, and C-C bond breaking activation energies calculated by DFT reflect the structural and electronic modification of the alloys. Computed descriptors for dehydrogenation selectivity correctly predict increases in selectivity for site isolated alloys, but do not show strong trends for alloys without site isolation. The C-C bond breaking activation energy barrier gives further insight into the dehydrogenation selectivity trends.

3.2 Introduction

Dehydrogenation is the first step in the activation of alkanes, and on purpose catalytic dehydrogenation is becoming increasingly important with the widespread exploitation of shale gas reserves, which contain a significant fraction of C2+ alkanes [117]. Light olefins, such as ethylene and propylene produced from dehydrogenation are important feedstocks for the petrochemical industry [3], [118]. Commercial processes for the production of light olefins include the Oleflex process (UOP) using a platinum-tin alloy catalyst, and the Catofin process

(Mcdermott-Lummus) which uses a chromium oxide catalyst [5], [119]. Light olefins are also produced as a byproduct of the fluidized catalytic cracking (FCC) or by steam cracking [4]. Dehydrogenation is an endothermic reaction, where the equilibrium conversion to alkenes increase with temperature and decreases with alkane pressure [36]. At the high temperatures required for dehydrogenation of light alkanes, hydrogenolysis to form methane and other lower carbon number species causes low selectivity to olefins [120]. Hydrogenolysis is a structure sensitive reaction, meaning it requires multiple active metal atoms (termed an ensemble), to be catalyzed [21]. Surprisingly, hydrogenolysis turnover rates are enhanced on smaller metal nanoparticles, which is rationalized based energetic differences in reaction barriers and adsorption energies on high index facets [19]. In contrast, dehydrogenation is a structure insensitive reaction, meaning it only requires only a single active metal atom to be catalyzed and hence the dehydrogenation turnover rate is not a function of particle size [6], [121].

To improve the selectivity of dehydrogenation catalysts, alloys take advantage of the difference in structure sensitivity between dehydrogenation and hydrogenolysis. By separating active metals with an inactive atom, termed a promoter, the turnover rate of hydrogenolysis can be decreased while the turnover rate of dehydrogenation is minimally effected, resulting in increased olefin selectivity. Most of the early work on structure sensitivity in hydrogenolysis was performed on bimetallics that form solid solutions [21]. In these structures, a solute metal randomly substitutes for a solvent metal atom in the parent lattice. This leads to a distribution of active metal ensemble sizes, and high dehydrogenation selectivity is only achieved at very high dilutions of the active metal [22], [23]. Recent work has focused more on intermetallic compounds, which have a fixed (or narrow) composition and can have crystal structures that differ from their pure components [122]. In these materials, the ensemble size is determined by the crystal structure and atomic plane. In some intermetallic compounds, such as PtZn, the active metal atoms are completely isolated from one another by promoter atoms [24]. In other structures, there are still small active metal ensembles, such as in the case of Pt_3M alloys with the $AuCu_3$ prototype phase [31], [114].

In addition to breaking up active metal ensembles, the promoter also electronically modifies the active metal. The electronic modification takes the form of a redistribution energy states in the d band, which results in the d band center moving away from the Fermi level [33], [34]. The modification of the d-band in platinum alloys can be observed by spectroscopic

changes seen in the L_3 edge X-ray absorption near edge structure (XANES) which maps the unfilled valence d density of states [100]. More recently, changes in the energy of the filled density of states have also been observed experimentally using resonant inelastic X-ray scattering (RIXS), which measures the energy separation between the weighted average energy of the filled and unfilled valence d states [24], [123], [124]. By the d-band model of chemisorption, this movement of the d-band center away from the Fermi level correlates to a weakening of adsorbate binding strengths, which can also contribute to the increased olefin selectivity in alloys [28], [94].

Most research on selective dehydrogenation catalysts has focused on platinum, which is more stable against deactivation and has less hydrogenolysis activity compared to other catalytic metals [38]. Modeling efforts on dehydrogenation and dehydrogenation selectivity have also focused on platinum and platinum alloys [46], [125]–[128]. Recent reports have also shown that palladium intermetallic compounds can have dehydrogenation selectivity comparable to platinum intermetallic compounds, but comparatively few computational efforts have been dedicated to palladium intermetallics [26], [129]. A frequently used dehydrogenation selectivity descriptor proposed in platinum intermetallics is the energy difference between the alkene desorption energy and the activation energy barrier of the first deep dehydrogenation [46], [130]. This descriptor accurately predicted that a platinum tin alloy would be more selective than pure platinum, which has been shown experimentally [44], [131]. Though the selectivity descriptor has thus far been used only for platinum bimetallics, the same mechanism of dehydrogenation and hydrogenolysis should imply that it is extendable to other active metals such as palladium. The usefulness of such a selectivity descriptor comes from its predictive power to computationally rank different alloy systems in order of their expected selectivity and to guide experimental efforts.

In an effort to validate the proposed selectivity descriptor we synthesize a series of palladium and palladium alloy catalysts with a wide variety of promoters and alloy structures. Intermetallic compounds between palladium and five different promoters: Indium, Zinc, Gallium, Iron and Manganese were synthesized, tested, and characterized to determine their structure, catalytic performance and electronic modification. The formation of alloy phases was verified through characterization of the -long and short-range order of the nanoparticles using in-situ synchrotron XRD and in-situ XAS. Electronic modification was shown experimentally by

in-situ Pd L_3 edge XANES and computationally by the Pd projected density of states (pDOS), in which the alloys showed changes in the first and second moments of the d band. The selectivity descriptor correctly predicts that site isolated alloys are more selective than alloys without site isolation, but only predicts weak selectivity improvement for alloys with the Pd_3M.

3.3 Methods

3.3.1 Catalyst Synthesis

3.3.1.1 Pd

A Monometallic 2% Pd catalyst was prepared by strong electrostatic adsorption (SEA). 5 grams of davasil 646 silica was dispersed in 50 mL of deionized (DI) water and the pH was adjusted to 11 with 32% ammonium hydroxide. 2.8g of 10% palladium tetraammine nitrate solution was diluted to a total volume of 25 mL and the pH was adjusted to 11 by the addition of 32% ammonium hydroxide. The silica dispersion and the palladium solution were mixed for 15 minutes. The silica was then allowed to settle out of solution and removed by filtration. The Pd-SiO_2 was then washed 3 times with DI water and dried at room temperature for 3 hours and then overnight at 125°C. After drying the catalyst was calcined at 300°C for 3 hours. The Pd-SiO_2 was then reduced in 5% H2 in steps from 100°C to 250°C at a 2.5°C/min ramp rate with 15 minute dwells every 25°C and then a fast ramp (10 C/min) to 550°C and a 30 minute dwell. The catalyst was then cooled to room temperature and passivated in air. A second monometallic Pd catalyst was synthesized by the above method except the calcination temperature was 200°C for 3 hours and the mass of 10% palladium tetraammine nitrate was adjusted to give a weight loading of 1%.

3.3.1.2 Pd-In

A 2% Pd 3% In catalysts was synthesized according to the procedure for Pd-In 0.8 in reference [32]. Briefly, In-SiO_2 was synthesized by incipient wetness impregnation of a $In(NO_3)_2$/Citric acid solution pH adjusted to 11 with ammonium hydroxide. The In-SiO_2 was dried at 125°C overnight and then calcined in air at 200°C. Palladium was then added by incipient wetness impregnation of a pH adjusted solution of palladium tetraammine nitrate. The Pd-In-SiO_2 catalyst was then dried overnight at 125°C and calcined at 200°C. The catalyst was

then reduced using a slow ramp to 200°C and then a fast ramp to 600°C in 5% hydrogen (balance N_2). The catalyst was cooled to room temperature in nitrogen and then passivated in air.

3.3.1.3 Pd-Fe

A 2% Pd 3%Fe catalyst was synthesized according to the procedure for the procedure for Pd_3Fe small in reference [33]. A 2:1 molar ratio of citric acid to iron (III) nitrate nonahydrate was pH adjusted to 11 using concentrated ammonium hydroxide. The solution was impregnated dropwise onto 5g of SiO_2 and dried at 125°C and then calcined at 400°C for 3 hours. Pd loading was accomplished using a pH adjusted solution of palladium (II) tetraammine nitrate. The Pd-Fe-SiO_2 catalyst was then dried at 125°C and then calcined at 250°C for 3 hours. Reduction was performed in 3% H_2 (balance Ar) at 200°C for 30 minutes and then at 600°C for 30 minutes. The catalyst was then cooled to room temperature and passivated in air.

3.3.1.4 Pd-Ga

A 2.5% Pd 2.5% Ga catalysts was prepared by sequential incipient wetness impregnation of gallium and palladium on silica. 1.25 g of gallium nitrate hydrate and 2 grams of citric acid were dissolved in DI water to a total volume of 5 mL. The pH was adjusted to 10 with 32% ammonia solution and subsequently impregnated into 5 g of davasil 646 silica. The Ga-SiO_2 was dried at 125°C overnight and then calcined at 400°C for 3 hours. Pd impregnation was done using 3.3 g of 10% palladium tetraammine nitrate diluted to 5 mL total volume and pH adjusted to 10 with 32% ammonia solution. The Pd solution was then impregnated to the pore volume of the 5 g of Ga-SiO_2 catalyst and then dried at 125°C overnight. The Pd-Ga catalyst was then calcined at 250°C for 3 hours and then subsequently reduced in 5% H_2 with a slow ramp (2.5°C/min) through 200°C and then a fast ramp (10°C/min) to 600°C with a 30 minute dwell. The reduced catalyst was then cooled to room temperature in 5% H_2 and passivated in air.

3.3.1.5 Pd-Zn

A 2% Pd 3% Zn catalyst was synthesized by sequential incipient wetness impregnation. 1.14 g of Zinc nitrate hexahydrate was dissolved in 2 mL of DI water and the pH was adjusted to 11 using 32% ammonia solution. Finally, the total volume of the Zn solution adjusted to 5 mL with the addition of DI water. The Zn solution was impregnated to the pore volume of 5 g of davasil 646 silica and dried overnight at 125 C. The Zn-SiO_2 catalyst was then calcined at 300°C

for 3 hours. 0.281 g of palladium tetraammine nitrate was dissolved in 3.5 mL of DI water and the pH was adjusted to 11 using 32% ammonia solution. The palladium solution was then impregnated to the pore volume of the calcined Zn-SiO_2 and dried at 125°C. The Pd-Zn-SiO_2 catalyst was calcined at 200°C for 3 hours and then reduced in 5% hydrogen (balance N_2) with a slow ramp (2.5°C/min) through 250°C and a fast ramp (10°C/min) to 550°C and a 30 minute dwell at temperature. The reduced catalyst was then cooled to room temperature in hydrogen and passivated in air.

3.3.1.6 Pd-Mn

A 1% Pd 5% Mn catalyst was synthesized by sequential incipient wetness impregnation. 0.814 g of manganese (II) nitrate hydrate and 0.874 g of citric acid were dissolved in 5 mL of Millipore water to give a solution with a 2:1 molar ratio of citric acid to manganese nitrate. The pH of the solution was adjusted to 11 by the addition of 32% ammonium hydroxide. The solution was then added dropwise to 5 g of davasil 646 silica. The Mn-SiO_2 was then dried at 125°C overnight and calcined at 250°C for 3 hours. Pd loading was done by diluting 1.4 g of 10% palladium tetraammine nitrate to 5 mL total volume and adjusting the pH to 11 with 32% ammonium hydroxide. The solution was then added dropwise to the Mn-SiO_2 and dried at 125°C overnight and calcined at 200°C for 3 hours. The Pd-Mn-SiO_2 catalyst was then reduced in 5% hydrogen (balance N2) with a slow ramp (2.5°C/min) through 250°C and a fast ramp (10°C/min) to 550°C with a 30-minute dwell at temperature. The reduced catalyst was then cooled to room temperature in 5% H2 and passivated in air.

3.3.2 In-situ Synchrotron X-ray Diffraction (XRD)

In-situ synchrotron XRD was performed at the ID-11C beamline of the advanced photon source. XRD was performed in transmission geometry using an X-ray wavelength of 0.1173 angstroms (105.7 keV). Samples for XRD were ground into a fine powder and pressed into a self-supporting wafer. The sample wafers were then loaded into a water cooled linkam stage capable of gas flow and heating. The X-ray windows on the cell were made of kapton film. The cell was purged with He before a flow of 3.5% H2 in He was started and the temperature ramped to 550°C at 10°C/min. After a 30 minute dwell at temperature, the cell was cooled to 35°C and a spectrum was collected. Diffracted X-rays were measured using a Perkin-Elmer large area

detector. Calibration was performed using a CeO_2 standard. Trace oxygen was removed from He using an oxygen trap made by Restek.

The collected 2D diffraction patterns were integrated to give conventional 2d powder diffraction data using fit2d software [37,38]. Background subtraction was done using scans of the empty cell in and the bare SiO_2 support. Pattern simulation was done using Materials Analysis Using Diffraction (MAUD) and phase references from ICSD [39–44]. Particle size broadening in simulated patterns was varied by changing the crystallite size.

3.3.3 In-situ X-ray Adsorption Spectroscopy (XAS)

Pd K edge XAS was performed at the MRCAT 10BM line of the advanced photon source. Samples were measured in transmission mode using 3 ion chambers which allowed for simultaneous measurement of a Pd foil reference. Samples were ground into a fine powder and pressed inside of a stainless steel sample holder and loaded into a quartz tube reactor. The reactor was sealed at each end by a 1 inch ultra-torr union modified with a gas flow port and a kapton window. The reactor was purged with He and then treated at 550°C in 3.5% H2 for 30 minutes. The cell was then purged at high temperature with He to desorb chemisorbed hydrogen and decompose any palladium hydride that may have formed during treatment. The samples were then cooled to room temperature in He and scanned. Samples were also scanned after exposure of the reduced samples to air at room temperature.

Extended X-ray adsorption fine structure (EXAFS) data on Pd and Pd alloys was fit using WinXAS software. The extracted chi was k^2 weighted and fourier transformed over a k range of 2.9-12. Phase and amplitude functions for Pd-Pd scattering were extracted from Pd foil with a coordination number of 12 and a bond distance of 2.75 angstroms. Pd-O scattering was extracted from palladium (II) acetate (4 Pd-O bonds at 2.05 Å). Bimetallic scattering (Pd-Mn at 2.62 Å, Pd-Zn at 2.71 Å, and Pd-Ga at 2.6 Å) were constructed using FEFF with the amplitude reduction factor, Debye-Waller factor and E_0 correction fixed to the values fit to Pd foil. Fitting was performed in R space on isolated first shell scattering for each sample by allowing the coordination number, bond distance, Debye-Waller factor and E_0 correction to vary.

Reduction-Oxidation difference EXAFS was performed by subtracting unweighted chi data of the reduced and air exposed samples. The core of the nanoparticle, which is unchanged during the surface oxidation process is subtracted out in the difference, and only the signal from

surface scattering modified during the reduction-oxidation process remains. Scattering that is lost from the reduced sample remains in phase with experimental phase and amplitude functions, but the gained Pd-O scattering is phase shifted with respect to the experimental reference due to the subtraction. To properly fit Pd-O scattering in the difference, the experimental Pd-O phase function is shifted by π radians to align it with the Pd-O scattering in the difference spectra. The phase shift effect has the added benefit of resolving which bonds are lost (in phase) and gained (phase shifted) during the reduction-oxidation process. Fitting of the difference spectra was performed in R space on fourier transformed k^2 weighted difference chi. Fourier transforms were taken over a k range of 2.9-10 and fit over an R range of 1-3. The fitting procedure was then identical to the above reduced samples.

Pd L_3 edge X-ray adsorption near edge structure (XANES) were measured at the 9BM line of the advanced photon source. Measurements were performed in fluorescence mode using a vortex 4 element detector. The samples were ground and pressed into a steel sample holder with the catalyst wafer at a 45-degree angle relative to the beam. The reactor used for treatment has been described elsewhere [61], and is capable of heating and gas flow with kapton windows for transmission and fluorescence measurements. Samples were treated by heating to 500°C in 3.5% H_2. After a 30-minute dwell at 500°C, the gas flow was switched to He at high temperature to desorb hydrogen and decompose any palladium hydride formed during the reduction. The samples were then cooled to room temperature and multiple scans were collected and averaged. L_3 edge XANES spectra were normalized using first order polynomial for the pre-edge region and a second order polynomial for the post-edge region. Due to the close proximity of the L_3 to the L_2 edge, the data collection range for post edge normalization is limited and the third order polynomial typically fit to the post edge region fits poorly. The absolute energy scale was calibrated using bulk PdO with an L_3 edge energy of 3174.4 eV.

3.3.4 Propane Dehydrogenation

Propane dehydrogenation was performed in a fixed bed microreactor. 50-150 mg of catalyst was mixed to a total mass of 1 g with davasil 646 silica and loaded into a quartz tube reactor with an inner diameter of 9.5 mm. The catalyst bed was dried in flowing nitrogen at 100°C for 15 minutes and then reduced in 5% H_2 in N_2 at 550°C for 30 minutes. Before starting

the flow of reactant gasses hydrogen was purged from the bed by flowing 100 ccm of nitrogen for 5 minutes. Propane dehydrogenation reactions were carried out at 550°C at 3 PSIG with 2.5% propane and 2.5% hydrogen. Conversion was adjusted by changing the total flow rate and mass of catalyst used in a test. Conversion and selectivity were calculated based on gas phase products measured by an online HP 6890 gas chromatograph with a flame ionization detector and a restek Alumina BOND/Na_2SO_4 column. A chromatogram was collected every 5 minutes for 90 minutes. The resulting time on stream data was fit with a first order exponential function to give the selectivity and conversion at zero deactivation.

Deactivation rate constants were measured on catalysts with an initial conversion between 19-21%. Time on stream data from 20 to 90 minutes was fit using a first order exponential decay model according to equation 5 below [132].

$$Ln\left(\frac{1-X_a}{X_a}\right) = k_d t + Ln\left(\frac{1-X_0}{X_0}\right) \quad (5)$$

Where X_a is the conversion of the catalyst at time t and X_0 is the initial conversion. Propylene production turnover rates were measured at differential conversion (>5%) in 2.5% propane and 2.5% hydrogen at 550°C. Rates were normalized based on the fraction of exposed palladium determined by surface oxidation EXAFS using the Pd-O coordination number.

3.3.5 STEM/EDS

Scanning transmission electron microscopy (STEM) and energy dispersive x-ray spectroscopy (EDS) was performed on an FEI Talos F200X S/TEM with a super-X EDS system and a high brightness field emission electron source. The microscope was operated at 300 keV and STEM images were recorded using a high angle annular dark field (HAADF) detector. Ground catalyst powder was physically mixed with a copper 300 mesh lacey carbon coated TEM grid (SPI supplies). Reported particle size distributions are number average particle sizes and were determined by measuring more than 250 particles. Measurement of particles was done using the FIJI distribution of imagej [133].

3.3.6 DFT

All the periodic density functional theory (DFT) calculations were performed with the VASP program where Kohn-Sham equations are solved self-consistently using the Perdew, Burke, and Ernzerhof functional (PBE).[134] A plane wave energy cutoff of 400 eV was used with a 3x3x1 Monkhorst-Pack k-point grid for Pd (111), Pd_3Fe (111), PdIn (110), PdZn (101) alloy surfaces; while a 2x2x1 k-point grid was used for Pd_3Mn/Pd (111) owing to its larger unit cell, where as a 3x2x1 k-point grid was used for Pd_2Ga (010) due to its rectangular unit cell. These values were confirmed to converge the adsorption energies within 0.05 eV. The adsorption properties and thermodynamic energy barriers on the surface are calculated using DFT geometry optimizations. The activation barriers are then estimated by nudged elastic band (NEB) calculations using both the first and second order methods (Quick-Min, LBFGS) developed by Henkelmann [135]. For Density of States (DOS) calculations, an energy cutoff of 520 eV and 9x9x1 Gamma-centered k-point grid was used along with tetrahedron method using Blöchl corrections.

The adsorption energies of open-shell species were calculated by referencing to the corresponding closed-shell species gas phase energies and adding a stoichiometric amount of gas phase H_2. The binding energies of C_3, C_2, C_1 deep dehydrogenated species were estimated using the gas phase propane, ethane and methane energies respectively. For each of these adsorbates, all the distinct binding configurations were generated using CatKit, a python based open-source code developed at SUNCAT implemented with some modifications for binding of C_3 adsorbates [136]. The geometry optimizations were then performed for all the sites and configurations, and the energy of the most stable site has been reported.

3.4 Results

3.4.1 Structural Characterization

Detailed characterization of the particle size, and phase composition of the Pd-In and Pd-Fe catalysts is detailed in references [26], and [129] respectively.

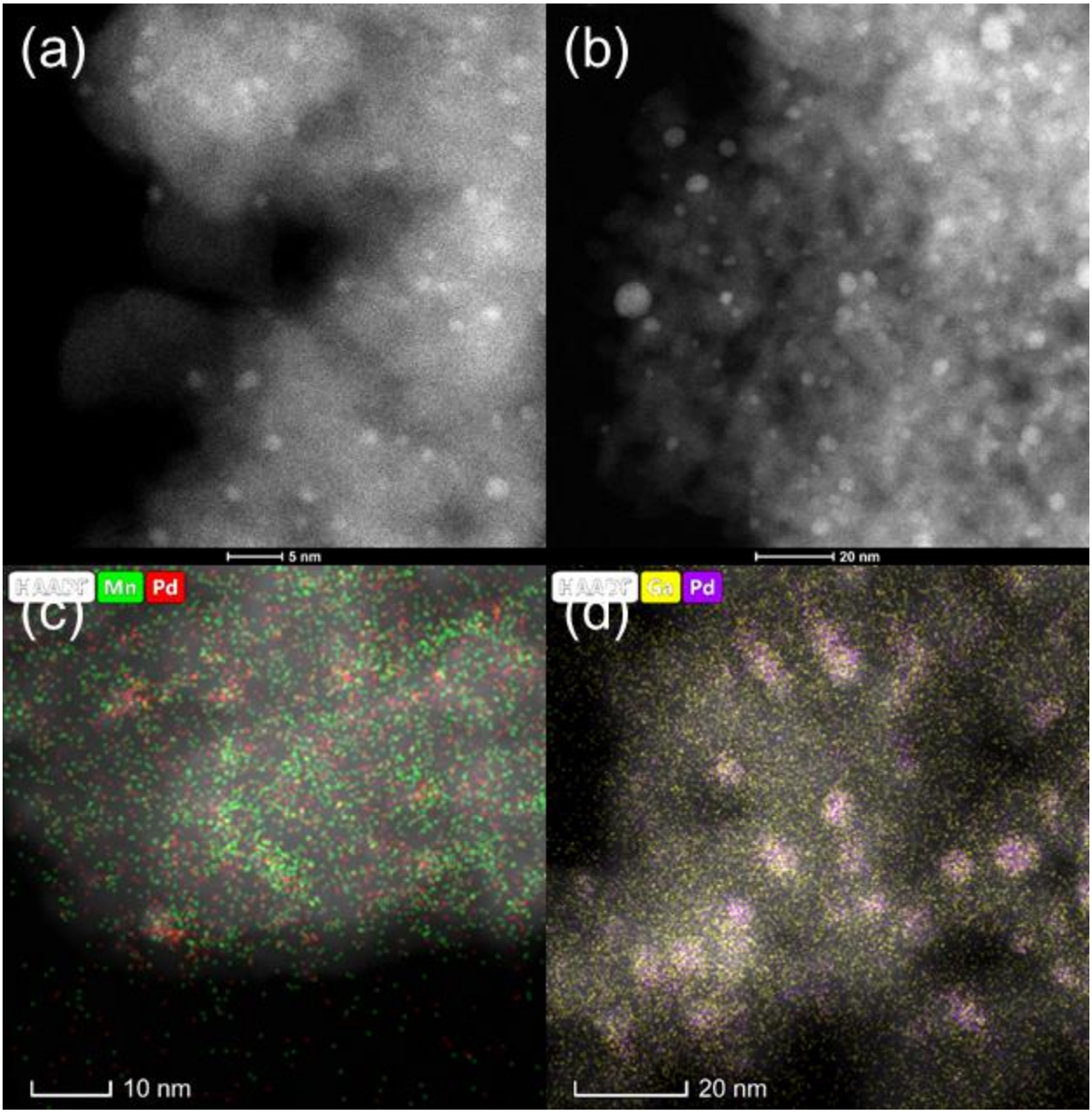

Figure 22: STEM images of Pd and bimetallic Pd catalysts: (a) 1Pd (b) 2Pd (c) STEM image of 1Pd-5Mn with overlaid EDX maps for Pd (red) and Ga (Green). (d) STEM image of 2.5Pd-2.5Ga with overlaid EDX maps for Pd (purple) and Ga (yellow)

Figure 22 shows STEM Images and EDX maps of Pd and Pd alloy catalysts. Pictured in figure 22a, the 1% Pd catalyst is monodisperse with small metal particles under 2 nm in diameter. In contrast, the 2% Pd catalyst, shown in figure 22a, contains both small (1-2 nm) particles and large (5+ nm) particles. The high temperature calcination treatment used in the 2Pd

catalyst results in agglomeration of the palladium oxide resulting in larger metallic particles after reduction. EDX was used to observe the dispersion of the second metal, which is difficult to distinguish from the support in STEM images. Figure 22c shows a STEM image of 1Pd-5Mn with overlaid EDX maps for manganese and palladium. The manganese is well dispersed across the support, small clusters containing both Pd and Mn can be seen, consistent with the formation of a Pd-Mn bimetallic. Ga in the Pd-Ga catalyst (figure 22d) is also well dispersed on the support, but the bimetallic Pd-Ga clusters are better resolved owing to their larger particle size.

Table 15: Number average particle size for Pd and bimetallic catalysts

Sample	Number average particle size (nm)
1Pd	1.4±0.5
2Pd	3.7±2.0
2Pd-3Zn	1.5±0.7
2Pd-3In	1.8±0.4
2.5Pd-2.5Ga	2.1±1.6
2Pd-3Fe	1.5±0.7
1Pd-5Mn	1.5±0.5

Table 15 shows the number average particle size for the two monometallic Pd catalysts and five bimetallic Pd catalysts. The 1% Pd catalyst was smaller in size than the 2% Pd catalyst due to the high calcination temperature employed in the synthesis of the 2% Pd catalyst. The standard deviation of the 2% Pd catalyst was also larger due to the presence of both small particles and a significant number of large agglomerates likely resulting from the coalescence and sintering of smaller particles. The bimetallic samples all had particle sizes within one standard deviation of one another and were approximately 1.5-2 nm. Similar to the 2% Pd catalyst, the 2.5%Pd-2.5Ga catalyst contained both small 1.5 nm particles and larger (5+ nm) agglomerates, which is reflected in the larger standard deviation of the particle size.

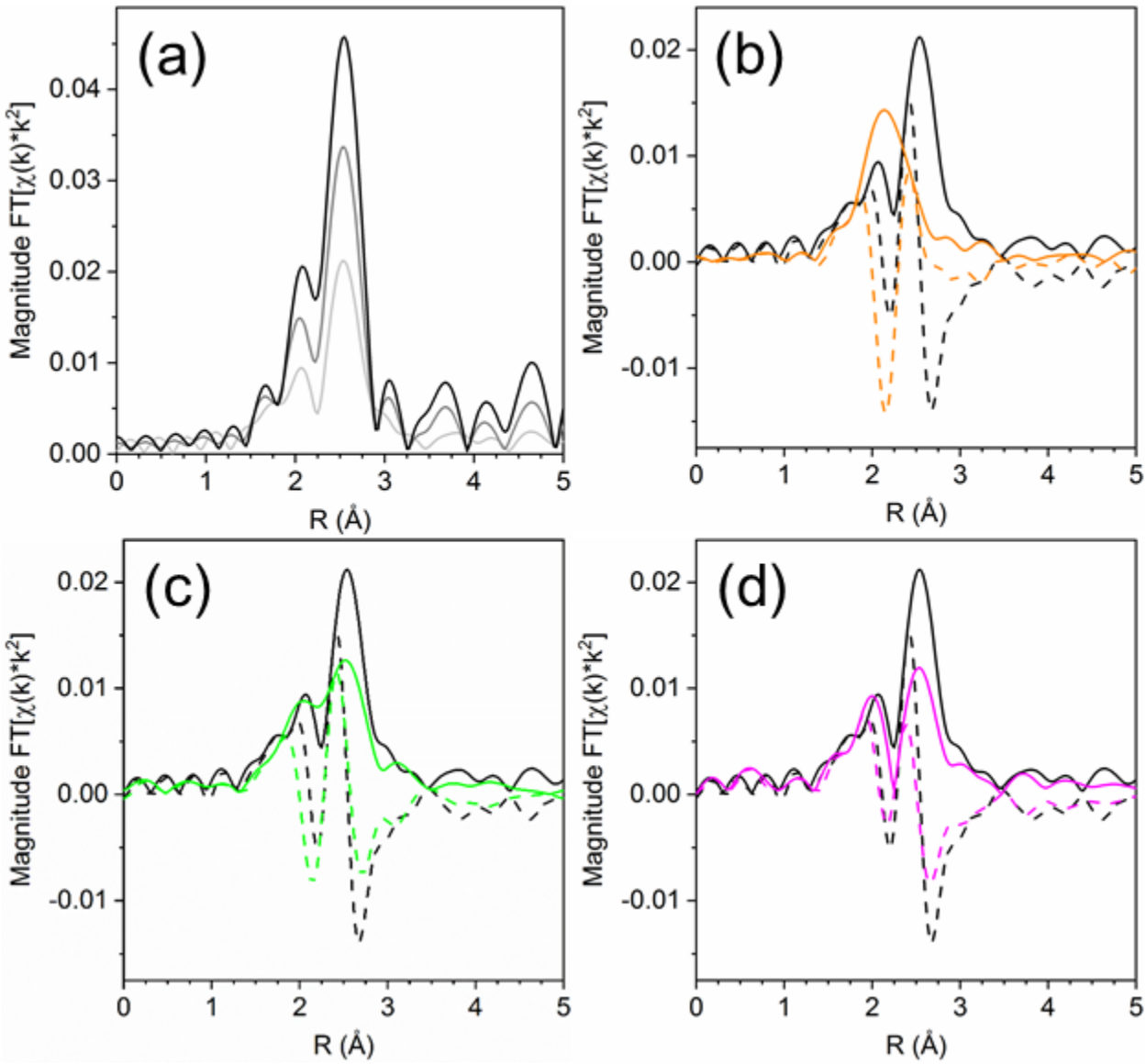

Figure 23: R space Pd K edge EXAFS magnitude (solid lines) and imaginary (dashed) components of Pd catalysts. a) monometallic Pd catalysts: Pd foil (black) 2Pd (grey) and 1Pd (light grey) b) 2Pd-3Zn (orange) and 1Pd (black) c) 2.5Pd-2.5Ga (green) and 1Pd (black) and d) 1Pd-5Mn (magenta) and 1Pd (black). Spectra were collected at room temperature in He after reduction at 550°C in 3.5% H2.

Table 16: EXAFS fitting parameters for Pd foil, Pd, Pd-Mn, Pd-Ga and Pd-Zn

Sample	Scattering Pair	CN	R (Å)	$\Delta\sigma^2$	E0 (eV)
Pd Foil	Pd-Pd	12	2.75	0	0
1Pd	Pd-Pd	7.7	2.74	.0035	-1.3
2Pd	Pd-Pd	10.4	2.74	.002	-1.8
1Pd-5Mn	Pd-Pd	6.1	2.71	.005	-2.6
	Pd-Mn	1.4	2.66	.005	-1
2.5Pd-2.5Ga	Pd-Pd	4.1	2.78	.003	-3.6
	Pd-Ga	2.7	2.49	.003	-3.7
2Pd-3Zn	Pd-Pd	1	2.81	.002	-5.1
	Pd-Zn	4.1	2.54	.002	-5.2

Pd K edge EXAFS results for the Pd, Pd-Ga, Pd-Mn, and Pd-Zn catalysts are shown in figure 23. For the monometallic Pd catalysts, the amplitude of the first shell scattering is attenuated due to the large fraction of surface atoms in the sample which decreases the average coordination number below 12 for bulk fcc metals. The second shell scattering in the 1Pd sample is also lower in intensity compared to the foil. No scattering from Pd-O is present demonstrating that the catalyst is in the metallic state. Fitting the first shell scattering for 1Pd (shown in table 16) gave a coordination number of 7.7 with a bond distance of 2.74 Å, which is consistent with a Pd nanoparticle. The 2Pd sample had a total coordination number of 10.4 at a bond distance of 2.74 angstroms.

The first shell scattering envelope in 2Pd-3Zn, shown in figure 23b, changes in shape relative to the monometallic Pd sample due to the formation of Pd-Zn bonds in the catalyst. The single R space peak is consistent with Pd having only nearest neighbor Zn. The broadness of the peak occurs due to an overlap between scattering from the first nearest neighbor zinc and single scattering from second nearest neighbor Palladium. Fitting (shown in table 16) gave 4.1 zinc neighbors at 2.54 Å and 1.0 Pd neighbors at 2.81 Å. The short Pd-Zn distance and long Pd-Pd distance is consistent with the structure expected for the β_1-PdZn phase [137].

The first shell scattering envelope from 2.5Pd-2.5Ga, bears resemblance to the monometallic Pd catalyst due to the presence of both Pd-Pd and Pd-Ga scattering. Pd-Pd scattering is comprised of 3 peaks, with the lowest intensity peak at the lowest R value and the highest peak at the highest R value. In the Pd-Ga catalyst, the second peak is much closer in intensity relative to the third high R peak as compared to the monometallic Pd sample due to

scattering from Pd-Ga. Fitting of the 2.5Pd-2.5Ga catalyst gave a Pd-Pd coordination number of 4.1 at a bond distance of 2.78 Å and a Pd-Ga coordination number of 2.7 at a bond distance of 2.49 Å. The Pd-Ga:Pd-Pd coordination number ratio (0.66) is consistent with the local Pd environment in Pd_2Ga which has a Pd-Ga:Pd-Pd ratio of 5:8 (0.63).

Similar to the Pd-Ga catalyst, the 1Pd-5Mn catalyst also showed a change in shape of the first shell scattering envelope, showing two peaks close to the same intensity instead of three peaks of increasing intensity. The scattering resembles that of the Pd-Fe sample in reference [129], albeit with the first peak at low R being lower in intensity than the high R peak. Fitting the Pd-Mn catalyst gave a Pd-Pd coordination number of 6.1 with a bond distance of 2.71 Å and a Pd-Mn coordination number of 1.4 at a bond distance of 2.66 Å.

The coordination number ratio in 1Pd-5Mn (0.23) does not match that of any bulk Pd-Mn phase. To further understand the structure of the catalyst, reduction-oxidation difference EXAFS was performed to examine the local Pd coordination in the surface layer of the nanoparticle. Figure 24 shows the R space difference XAS spectra between the 1Pd-5Mn catalyst in the reduced state and after exposure to air at room temperature. Three peaks are present: the lowest R space peak is due to Pd-O scattering gained during the surface oxidation, while the two higher R peaks between 2-3 Å (phase uncorrected distance) are due to the loss of Pd-Mn and Pd-Pd bonds. Table 17 shows the fit of the difference spectra. The Pd-O coordination number was 0.4 at a bond distance of 2.05 Å, a bond distance typical for palladium oxide. The surface Pd-Mn to Pd-Pd ratio from the difference is 0.56, significantly higher than the total nanoparticle ratio. The difference in ratio between the surface and total neighbor ratios is consistent with a core shell nanoparticle having a surface phase that is Mn rich with respect to the total particle composition.

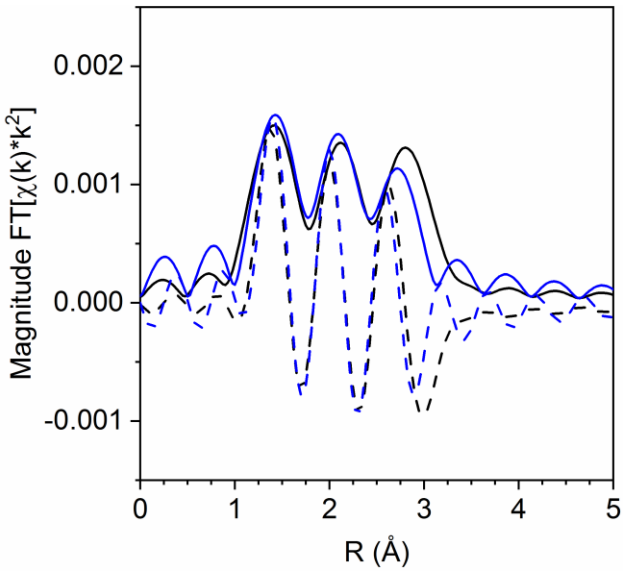

Figure 24: Reduction-Oxidation difference EXAFS of 1Pd-5Mn with the experimental difference magnitude (solid) and imaginary (dashed) shown in black and the difference fit shown in blue.

Table 17: Reduction-Oxidation difference EXAFS fit of 1Pd-5Mn

Scattering Path	Coordination Number	Bond Distance (Å)	σ^2 (Å^2)	E_0 (eV)
Pd-O	0.4	2.05	0.002	2.3
Pd-Pd	0.9	2.73	0.004	-3.2
Pd-Mn	0.5	2.63	0.004	1.8

To determine the phase composition of the catalysts, in-situ synchrotron XRD was used. A high X-ray energy was used to maximize the difference in absorption cross section between the amorphous SiO_2 support and palladium. The high flux provided by an insertion devise allows for collection of data with sufficient signal to noise to resolve the small broad features from nanoparticles. Use of an in-situ cell ensures that the entire nanoparticle remains in the metallic state during measurement, otherwise the surface of the nanoparticle is oxidized during measurement leading to misleading values of the particle size and lattice parameter [[80]].

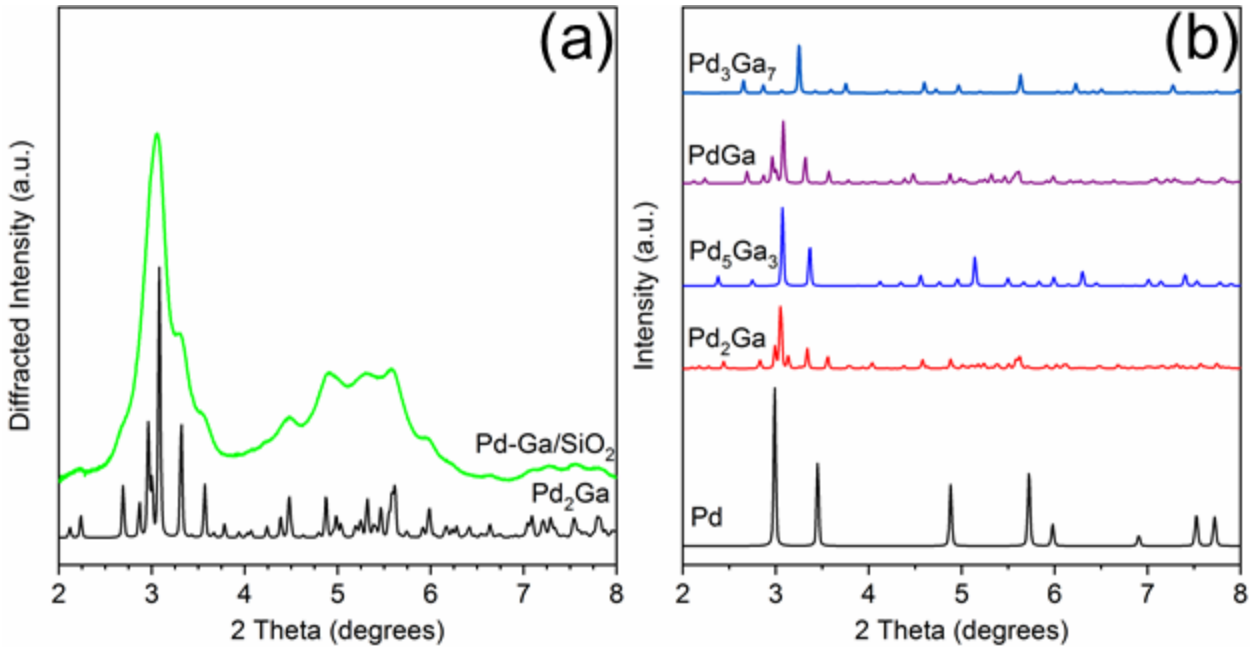

Figure 25: (a) In-Situ synchrotron XRD pattern for 2.5Pd-2.5Ga (green) after a reduction treatment at 550°C in 3.5% H2 with simulated Pd_2Ga pattern (black) and (b) Simulated bulk patterns for Pd-Ga intermetallic compounds

Figure 25 shows the simulated patterns of the possible PdGa phases and the experimental pattern for the Pd-Ga catalyst. The experimental pattern, though significantly broadened due to the particle size, matches that of Pd_2Ga, which has an orthorhombic Co_2Si structure. The high X-ray energy used (105.7 keV) causes diffraction peaks to occur at lower 2 theta and over a smaller 2 theta range than is typical of a laboratory XRD instrument. The XRD result is consistent with the EXAFS results which show Pd having a neighbor ratio (Pd-Ga:Pd-Pd) consistent with that of Pd_2Ga, in which Pd has 5 Ga neighbors and 8 Pd neighbors.

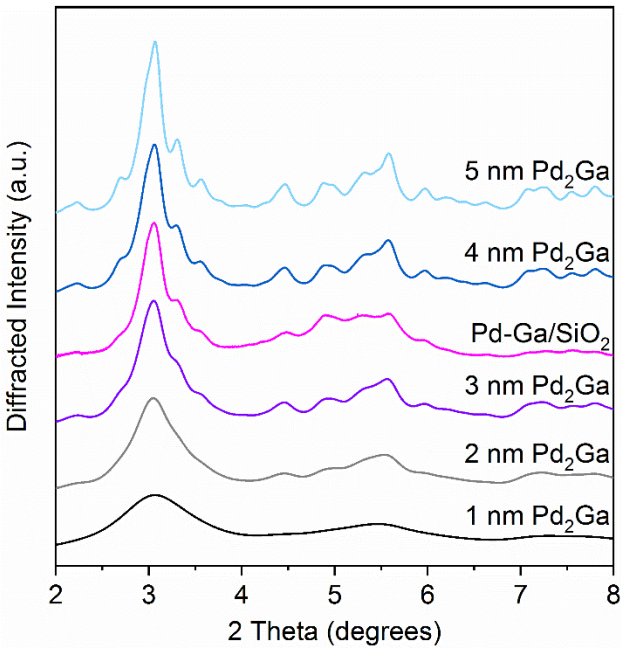

Figure 26: Simulated Pd_2Ga XRD patterns with different crystallite sizes (black, grey, purple, blue, light blue) compared with experimentally measured Pd-Ga catalyst (pink).

Due to the large number of overlapping peaks and imperfect background subtraction, it was not possible to determine a lattice parameter using the above pattern. However, simulation of the particle size broadening, shown in figure 26, gives an estimate of the particle size. The first major group of peaks, between 2.5-4 degrees, merges into a single asymmetric peak when the particle size is below 2 nm. In the 3 and 4 nm sized simulations, distinct shoulders start to emerge, and 4 major peaks can be resolved. In the 5 nm simulation, the most intense peak in the pattern around 3.1 degrees starts to split into two distinct peaks. In the Pd-Ga catalyst, the first cluster of peaks between 2.5-4 degrees most closely resembles the 3 nm simulation, which is larger the TEM measured particle size of 2.1. The difference between the XRD determined value and the TEM determined value can be attributed to the presence of microstrain broadening and the volume averaging nature of the XRD measurement.

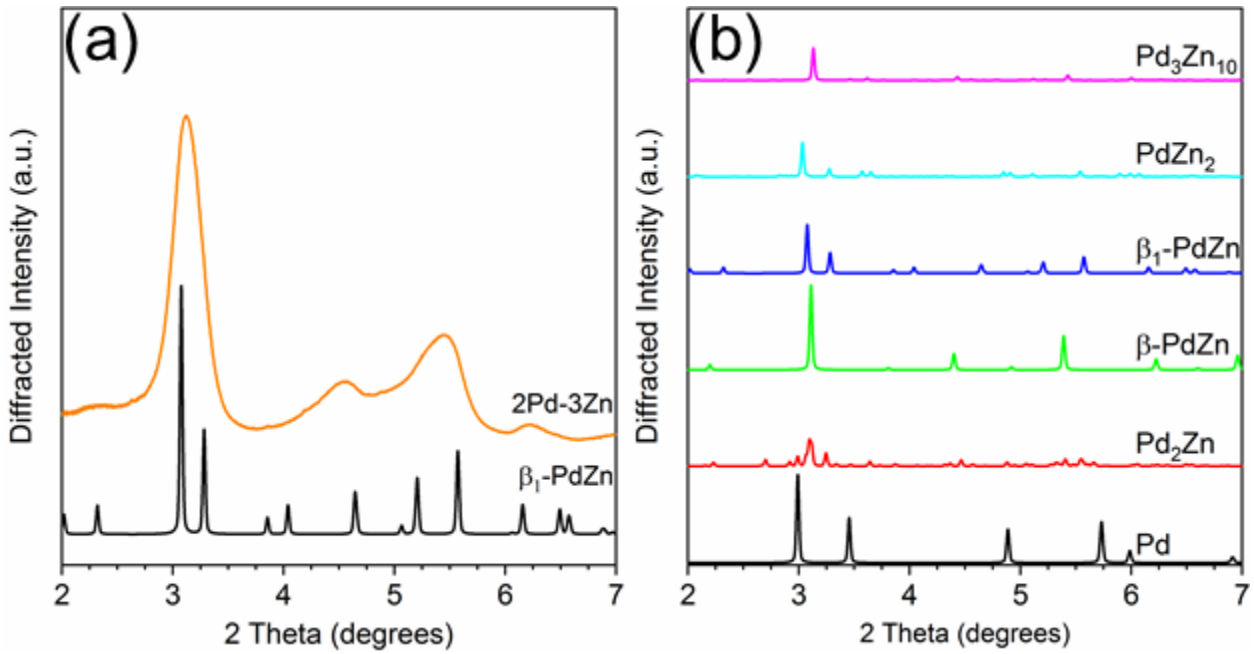

Figure 27: (left) simulations of bulk PdZn phases and (right) experimental in-situ synchrotron XRD pattern for the Pd-Zn catalyst (orange) along with simulated pattern for the β1-PdZn phase.

Figure 27 shows simulations of the bulk Pd-Zn phases and the experimental pattern for 2Pd-3Zn. Similar to the Pd-Ga catalyst, the diffraction peaks in the Pd-Zn catalyst are broadened due to the small particle size. Four distinct peaks are resolved, though some are asymmetric due to peak overlap. The pattern matches that of the β_1-PdZn phase, which has a tetragonal unit cell and body centered symmetry. The assignment of the β_1-PdZn phase is consistent with the EXAFS results which show only zinc nearest neighbors and a second nearest neighbor Pd at a long bond distance. Previous reports of Pd-Zn bimetallics synthesized by sequential incipient wetness impregnation have also shown the formation of the β_1-PdZn phase [25].

3.4.2 Propane Dehydrogenation

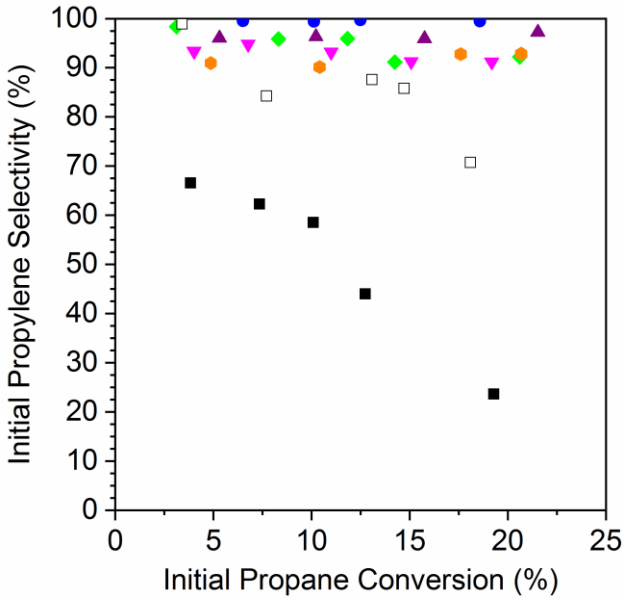

Figure 28: Initial propylene conversion for 2Pd-3Zn (blue circles), 2Pd-3In (purple triangles), 2.5Pd-2.5Ga (green diamonds), 1Pd-5Mn (magenta inverted triangles), 2Pd-3Fe (orange hexagons), 1Pd (open black squares), and 2Pd (filled black squares) plotted against the initial propane conversion. Tests were performed at 550°C in 2.5% H2 and 2.5% propane after pre-reducing in 550°C in 5% H2

Figure 28 shows the propylene selectivity at different levels of total propane conversion for Pd and Pd alloy catalysts. Catalyst tests were performed with cofed hydrogen as a more demanding test of catalyst selectivity, which is required for hydrogenolysis. The main products were propylene, methane, ethane and ethylene, the latter three resulting from hydrogenolysis. The 2% Pd catalyst (4 nm) shows poor selectivity, 70%, at differential conversion, but as the conversion is increased, the selectivity quickly drops to around 25% at 20% conversion. The 1% Pd catalyst (1.5 nm) shows much higher selectivity at equivalent conversion compared to the 2% Pd catalyst which demonstrates the effect of particle size on the rate of hydrogenolysis. Similar to the 2% Pd catalyst, the selectivity of the 1% Pd catalyst is high (~100%) at differential conversion but decreases with increasing conversion, falling to 70% at 20% conversion.

In comparison, the alloy catalysts have selectivity above 90% across the conversion range tested. For 2Pd-3Zn the conversion was above 99% up to 20% conversion. The 2Pd-3In catalyst also did not decrease with conversion, but the selectivity was slightly lower than the 2Pd-3Zn

catalyst at 96%. The 2.5Pd-2.5Ga catalyst showed a small decrease in selectivity, falling from 98% selectivity at 3% conversion to 92% selectivity at 20% conversion. The 1Pd-5Mn catalyst had a lower selectivity than the Pd-Zn and Pd-In catalysts, between 95-91%. The 2Pd-3Fe catalyst also did not decrease in selectivity with increasing conversion, but the selectivity was constant at a lower selectivity (91%).

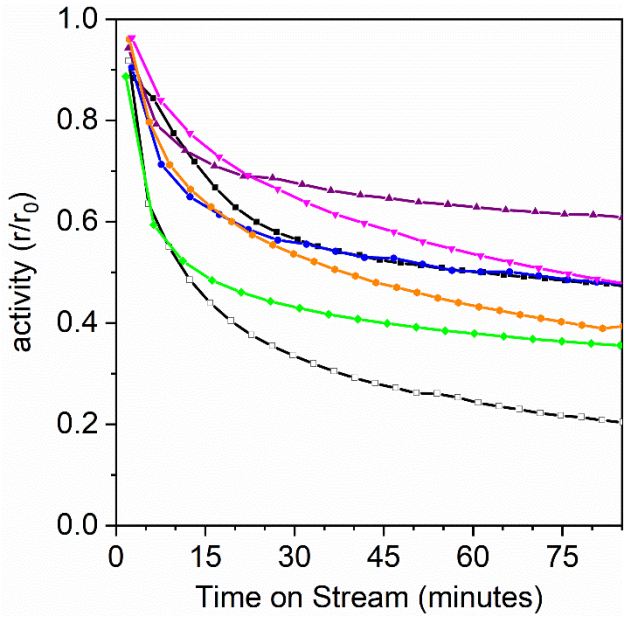

Figure 29: Normalized propane conversion vs. time on stream for 1Pd (unfilled black squares), 2Pd (filled black squares), 2Pd-3Zn(blue), 3Pd-3In (purple), 2.5Pd-2.5Ga (green), 1Pd-5Mn (magenta), and 2Pd-3Fe (orange). Tests were run at 550C, 3 PSIG, with 2.5% propane and 2.5 H_2

Figure 29 shows the dehydrogenation activity (r/r_0) as a function of time on stream for the Pd and Pd alloy catalysts with an initial conversion between 19-21%. All catalysts showed an initial fast deactivation period in the first 20 minutes of testing and which then leveled off to a slower deactivation rate. The deactivation rate constants for the catalysts in figure 29 are shown in table 18. The deactivation rate constant was smaller for the 2Pd sample which had a larger particle size as compared to the 1Pd catalyst which had a particle size the same as the alloy catalysts. The alloys had a lower deactivation rate constant compared to the similarly sized monometallic Pd catatalys, but the difference between the most stable alloy (2Pd-3In) and 1Pd was only a factor of 4. Among the alloys, the first order deactivation rate constants (shown in table 19) only varied by a factor of 3.

To measure the percentage of exposed palladium (dispersion) of the monometallic and alloy catalysts, the catalysts were measured by XAS after exposure to air at room temperature. The surface Pd oxidizes, which can be seen by XAS as Pd-O scattering. The fraction of exposed Pd is correlated to the dispersion based on the fractional Pd-O coordination number, where a Pd-O coordination number of 4 represents a dispersion of 100%. Fits of the oxidized catalysts are shown in table 18. The method closely matches the dispersion measured by CO chemisorption for the Pd-In catalyst as reported in reference [26], and has the added benefit of avoiding the confounding effect introduced with bimetallics where both constituents adsorb CO.

Table 18: Pd K edge EXAFS fits of Pd and Pd alloy catalysts after room temperature air exposure

Sample	Scattering Pair	Coordination number	Bond Distance (Å)	Debye-Waller factor ($Å^2$)	E_0 (eV)
1Pd	Pd-Pd	5.6	2.71	0.006	-3.2
	Pd-O	1.4	2.02	0.002	0.4
2Pd	Pd-Pd	8.6	2.74	0.0018	-2.0
	Pd-O	0.6	2.01	0.002	1.6
2Pd-3Zn	Pd-Pd	1.3	2.7	0.003	-3.6
	Pd-Zn	2.2	2.52	0.003	-9.6
	Pd-O	0.5	2.05	0.002	2.1
2Pd-3In	Pd-M	4.9	2.7	0.006	-3.3
	Pd-O	0.6	2.04	0.002	0.4
2.5Pd-2.5Ga	Pd-Pd	3.6	2.75	0.003	-1.8
	Pd-Ga	1.4	2.46	0.003	-9.2
	Pd-O	0.3	2.01	0.001	1.9
2Pd-3Fe	Pd-Pd	5.2	2.72	0.004	-0.2
	Pd-Fe	1.6	2.6	0.004	-4.4
	Pd-O	0.4	2.02	0.002	-1.6

Table 19: Dehydrogenation rate, first order deactivation rate constants and activity loss after 90 minutes of reaction for Pd and Pd alloy catalysts

Sample	Dispersion	Propylene TOR (s^{-1})	Deactivation rate constant (m^{-1})/10^{-3}	Activity loss after 90 minutes (%)
2Pd-3Zn	0.13	0.30	3.3	52
2Pd-3In	0.15	0.25	2.3	39
2.5Pd-2.5Ga	0.08	0.20	4.0	64
2Pd-3Fe	0.08	0.40	6.0	62
1Pd-5Mn	0.10	0.26	6.3	48
2Pd	0.18	0.03	3.2	54
1Pd	0.35	0.05	8.6	80

Table 19 also shows the propylene production turnover rate for the Pd and Pd alloy catalysts. The monometallic Pd catalysts have a low turnover rate: 0.03 s^{-1} for the 2Pd catalyst which has a large particle size and 0.05 s^{-1} for the 1Pd catalyst which has a particle size the same as the alloy samples. The alloy samples have propylene production turnover 4-8 times higher than the monometallic Pd catalyst of the same size. Between the alloys, the propylene production turnover rate only varied by a factor of 2.

3.4.3 Electronic Characterization

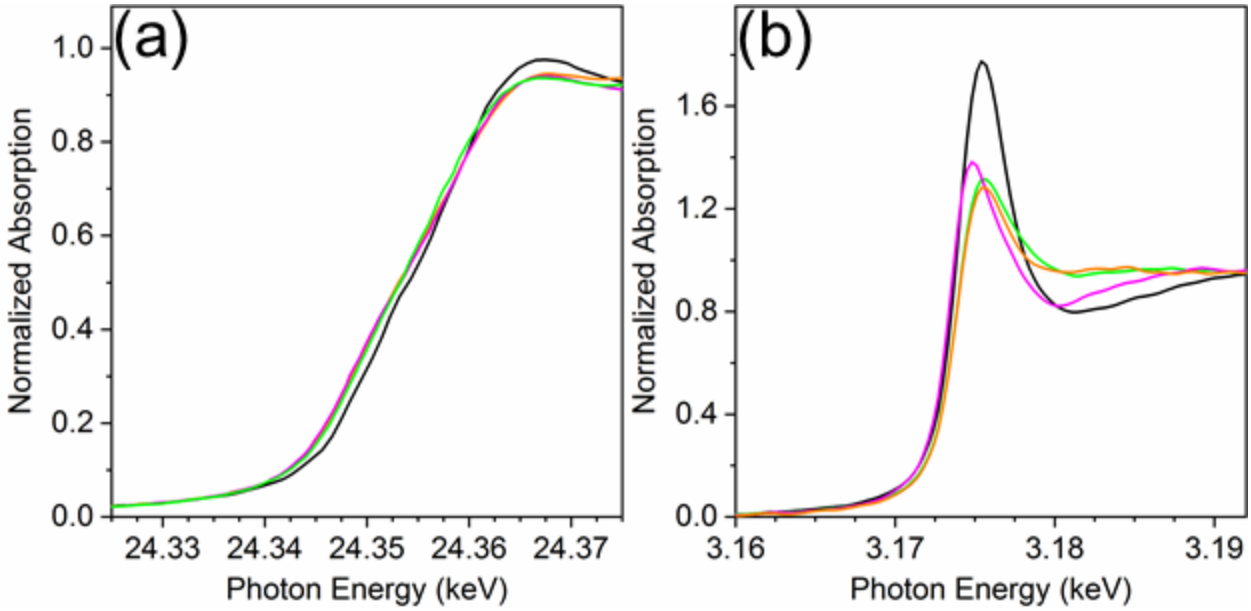

Figure 30: XANES of 1Pd (black), 2Pd-3Zn (orange), 2.5Pd-2.5Ga (green) and 1Pd-5Mn (magenta) at the K edge (a) and L_3 edge (b) after reduction at 550°C in 3.5% H2.

In addition to changing the catalyst structure, alloying can also electronically modify palladium, which can be studied by XANES. Figure 30a shows the Pd K edge XANES collected for 2Pd-3Zn, 2.5Pd-2.5Ga, 1Pd-5Mn and 1Pd after reduction in 3.5% H2 (balance He) for 30 minutes. The alloy samples show small changes in the edge shape which are indicative of alloying. The first peak in the XANES is lower in intensity for the three alloy samples and the edge position for each is shifted 0.2 eV lower in energy compared to the Pd foil value of 24350.0 eV. The close edge position and white line intensity shows that the alloy sample and Pd nanoparticles are all in the metallic state. Because the final state in K edge absorption is a p electron, and transition metals bond and adsorb through d electron interactions, only small changes are evident at the Pd K edge. Larger modifications can be seen at the L_3 edge, which is more sensitive to adsorbates and heteroatomic bonding due to the final state involving unfilled valence s and d states.

Figure 30b shows the Pd L_3 edge XANES for 2Pd-3Zn, 2.5Pd-2.5Ga, 1Pd-5Mn and 1Pd after reduction at 500C in 3.5% H_2. The modification of the XANES due to alloying is evident in the intensity and broadness of the white line, demonstrating the sensitivity of the L_3 edge to heteroatomic bonding. The PdZn and PdGa catalysts look similar, both with white line intensities lower than and broader than Pd sample. The PdGa sample white line is slightly broader and higher in intensity compared to the PdZn sample. Conversely, the PdMn sample has a white line that is narrower and lower in intensity compared to the Pd catalyst. The edge energy for the Pd and PdMn catalysts was 3173.6 eV. For PdGa and PdZn, the edge energy increased to 3173.9 eV. The dipole selection rule for Pd L_3 edge XANES allows for transition of a $2p_{3/2}$ electron into an unfilled 4s or 4d state. Since metallic Pd is d_{10}, there are no unfilled d states and the changes in the Pd L_3 XANES reflect the 4s unfilled density of states (conduction band) which are just above the 4d electrons in energy. The change in white line shape for the alloys represents a redistribution of the energy of the unfilled s states resulting from alloy formation.

3.4.4 Density Functional Theory

To further understand the catalytic trends in the different alloys considered, Density Functional Theory (DFT) calculations were carried out on model surfaces of each alloy. Calculations were carried out on the most stable terrace surfaces, corresponding to their respective bulk alloy structure found by XRD experiments at reaction temperatures. For alloy

phases with FCC structures, the (111) face was used. For the body centered cubic PdIn, the (110) surface was used, and the (101) surface was used for body centered tetragonal β_1-PdZn. For the orthorhombic Pd_2Ga structure, the (010) surface was chosen based on the high packing density and flatness compared to other crystal planes in Pd_2Ga and because the surface stoichiometry matches the bulk composition. The (010) surface of Pd_2Ga has also been modeled by others for the semihydrogenation of acetylene [138]. To simulate the core shell structure of Pd_3Mn/Pd Pd atoms were replaced with Mn atoms in the first two atomic layers of the slab corresponding to the ordering of Pd_3Mn with $AuCu_3$ structure.

For monometallic Pd, four adsorption sites were considered: 1-fold ontop, 2-fold bridge, 3-fold hexagonal close packed (HCP), and 3-fold face centered cubic (FCC). In the FCC alloy systems, the additional promoter ontop, Pd-M bridge, and 3 fold sites containing 2Pd and 1 promoter atom were also considered. In the 2:1 structure of Pd_2Ga, the same ontop and bridge site geometries were present as in the 3:1 fcc alloys, but the 3 fold sites had different geometry due to the crystal structure. The threefold sites considered were 3 fold sites of Pd with subsurface Ga, and 3 fold sites with 2 pd atoms and one Ga atom with subsurface Pd. In the site isolated 1:1 alloys, only ontop and bridge bonding configurations exist on the close packed model surfaces.

3.4.4.1 Adsorption Energies

The adsorption energies of all the intermediates considered are weaker on the alloys as compared to monometallic Pd. The changes in binding energies and the most stable configurations have been discussed for a few key intermediates (propylene, hydrogen, ethylidyne).

Table 20: Most stable binding site and binding energy (relative to gas phase propylene) for Pd and 5 Pd alloy surfaces.

Phase	Propylene Binding Site	Binding energy (eV)
Pd (111)	Pd-Pd bridge	-0.79
Pd_3Mn/Pd (111)	Pd-Pd bridge	-0.73
Pd_3Fe (111)	Pd top	-0.49
Pd_2Ga (010)	Pd top	-0.48
PdZn (101)	Pd top	-0.13
PdIn (110)	physisorbed	-0.06

Propylene binding sites and binding energies are shown in table 20. Propylene is most stable on the bridge site on Pd (111) surface, where it takes a di-sigma configuration; whereas

the ontop configuration is unstable by 0.1 eV. From the gas phase propylene, C=C pi bond is elongated from 1.34 Å to 1.45 Å indicating that the propylene pi bond is weakened upon adsorption. In comparison to Pd surface, the change in binding energy for the Pd_3Mn/Pd is less than 0.05 eV which is within DFT error. The most stable binding configuration is still the di-sigma in the bridge configuration. In contrast the binding of propylene is weakened by almost 0.3 eV for Pd_3Fe and Pd_2Ga surfaces. While the decrease in binding energies are larger, 0.66 eV and 0.73 eV for 1:1 PdZn and PdIn respectively in comparison to pure Pd surface. The most stable configuration also shifts from bridge Pd-Pd to ontop-Pd for the 4 alloy surfaces (Fe, Ga, Zn, In); most notably on the PdIn(110) surface propylene is physisorbed. This clearly shows that the effect of increasing in promoter content on the binding energies of propylene on the alloy surfaces.

Table 21: Most stable H binding site and corresponding binding energy (relative to gas phase H_2) for Pd and Pd alloy surfaces

Phase	H binding site	Binding energy
Pd (111)	FCC	-0.63
Pd_3Mn/Pd (111)	Pd-Pd-Pd HCP	-0.55
Pd_3Fe (111)	Pd-Pd-Pd HCP	-0.46
Pd_2Ga (010)	Pd-Pd-Pd HCP	-0.43
PdZn (101)	Pd-Pd bridge	-0.25
PdIn (110)	Pd-Pd bridge	0.03

Hydrogen binding sites and binding energies are shown in table 21. The most stable adsorption site for hydrogen atom on pure Pd (111) surface is the 3-fold fcc site. The binding energy of hydrogen is weakened by 0.1 eV on core-shell Pd_3Mn/Pd, while it decreases by approximately 0.2 eV on Pd_3Fe and Pd_2Ga surfaces in comparison to the pure Pd surface. The most stable adsorption site for hydrogen changes to the hcp Pd_2-Pd site for all three alloy surfaces. Similar to the case of propylene the decrease in binding energy for the 1:1 PdZn and PdIn surfaces are larger, by 0.38 eV and 0.66 eV respectively, and the most stable binding site becomes the Pd-Pd bridge. The changes of site preference for 1:1 alloys as compared to the 3:1 and 2:1 alloys, is attributed to the loss of three fold sites containing only the Pd sites.

Table 22: Most stable ethylidyne binding sites and binding energies for ethylidyne

Phase	Ethylidyne binding site	Binding energy (eV)
Pd (111)	HCP	0.96
Pd_3Mn/Pd (111)	Pd-Pd-Pd HCP	1.35
Pd_3Fe (111)	Pd-Pd-Fe FCC	1.54
Pd_2Ga (010)	Pd-Pd-Pd HCP	1.98
PdZn (101)	Pd-Pd-Zn HCP	2.96
PdIn (110)	Pd-Pd-In HCP	3.18

Among the intermediates considered, the deeply dehydrogenated intermediates had the largest decrease in binding energies, shown in table 22. Ethylidyne, one of the dehydogenated C_2 intermediates, is most stable on the 3-fold hcp site on the Pd (111) surface. The binding energy is weakened by 0.39 eV, 0.58 eV, 1.02 eV for Pd_3Mn/Pd, Pd_3Fe, Pd_2Ga terraces respectively. Ethylidyne is still most stable on 3-fold hcp site for Pd_3Mn/Pd and Pd_2Ga, but interestingly the site preference changes to fcc-Pd_2-Fe for the Pd_3Fe terrace; although the hcp Pd_2-Pd is unstable only by 0.1 eV. The decrease in binding energies are again higher for 1:1 PdZn and PdIn surfaces by 2.22 and 2.00 eV respectively. On the 1:1 alloys ethylidyne is most stable on the hcp-Pd_2-X sites, where the adsorbate directly interacts with the promoter, which contributes to the strong decrease in binding energy in the 1:1 alloys. The binding energy trends for propyne and methylidyne on the alloy surfaces are similar to ethylidyne.

3.4.4.2 C-H and C-C Bond Activation

A commonly used selectivity descriptor is the energy difference between the propylene desorption energy and the propylene dehydrogenation barrier, which has been shown to explain the selectivity trends for PtSn alloys in comparison to pure Pt [130]. The propylene dehydrogenation barrier to 1-propenyl was estimated using NEB calculations with the barrier tabulated in table 23. The increase in barrier, as compared to pure Pd, is highest for the PdIn surface where the barrier increases by ~0.7 eV; while the lowest change is for Pd_3Mn/Pd surface where the barrier increases by only 0.1 eV. Using these activation barriers, the selectivity descriptor was calculated in table 23, with more negative values signifying more favorable propylene desorption.

Table 23: Propylene dehydrogenation activation energy barrier and calculated dehydrogenation selectivity descriptor for Pd and Pd alloys.

Phase	Propylene dehydrogenation barrier (eV)	Selectivity descriptor (eV)
Pd (111)	0.98	-0.19
Pd_3Mn/Pd (111)	1.10	-0.37
Pd_3Fe (111)	1.30	-0.81
Pd_2Ga (010)	1.26	-0.78
PdZn (101)	1.38	-1.25
PdIn (110)	1.66	-1.60

The recent work of Saerens on Pt (111), also shows that the C-C bond breaking of propyne, which is turn formed from deeper dehydrogenation of propylene, is also kinetically relevant for the side-product formation methane, ethylene [139]. The propyne C-C bond breaking, leads to the formation of methylidyne (C_1) and ethylidyne (C_2) and these species can hydrogenate to form methane and ethane respectively. Alternatively, the C_1 and C_2 species can dehydrogenate further to form carbon on the surface which is believed to be a precursor to for coke formed on the surface. Hence C-C bond breaking barriers of propyne on the alloys can further solidify the trends observed from the estimation of the selectivity descriptor. The calculated thermodynamic and kinetic barriers for the propyne C-C bond breaking are given in the Table 24. The reaction thermodynamic barrier was estimated by using the binding energies of propyne, ethylidyne and methylidyne, by assuming infinite separation between the formed C_1 and C_2 intermediates, and the kinetic barriers were calculated using NEB. The thermodynamic barrier for C-C bond cleavage is larger on all alloys, the same is not true of the kinetic barriers, where for Pd_3Fe the kinetic barrier for C-C bond cleavage is 0.3 eV lower than on monometallic Pd. On all of the other alloys, the barrier is higher than monometallic Pd, with the site isolated alloys having higher barriers than those without.

Table 24: thermodynamic and activation energy barriers for C-C bond cleavage of propyne on Pd and Pd alloy surfaces

Alloy surfaces	Thermodynamic Barrier (eV)	Kinetic Barrier (eV)
Pd (111)	-0.08	1.2
Pd_3 Mn/Pd (111)	0.68	1.5
Pd_3 Fe (111)	1.06	0.92
Pd_2 Ga (010)	1.83	1.84
PdIn (110)	3.82	n.d.
PdZn (101)	3.97	n.d.

3.4.4.3 Electronic Structure Calculations

Table 25: First and second moments of the Pd d band pDOS for surface Pd atoms in monometallic Pd and Pd alloys.

Structure	d-band center (first moment) (eV)	d-band width (second moment) (eV)
Pd (111)	-1.54	2.19
Pd_3Mn/Pd (111)	-1.67	2.30
Pd_3Fe (111)	-1.85	2.51
Pd_2Ga (010)	-1.95	2.55
PdZn (101)	-2.07	2.70
PdIn (110)	-2.16	2.66

The d band projected density of states were calculated for surface Pd atoms to quantify the electronic modification of palladium in the alloy structures shown in table 25. All alloys show movement of the d-band center away from the Fermi level and a broadening of the d band. The changes are smallest for Pd_3Mn/Pd, which also showed the smallest changes in binding strengths. The alloys that had the largest binding energy shifts (PdIn and PdZn) also showed the largest movement in the d-band center, in agreement with the d-band theory. Integration of the pDOS up to the Fermi energy showed a negligible change in the number of valence d electrons in the alloy structures, which suggests that electron transfer does not occur to or from the d band and that palladium remains d_{10} in all the alloys. The lack of d states above the Fermi level is consistent with the L_3 edge XANES modifications coming from s unfilled state modification.

3.5 Discussion

3.5.1 Catalyst structure

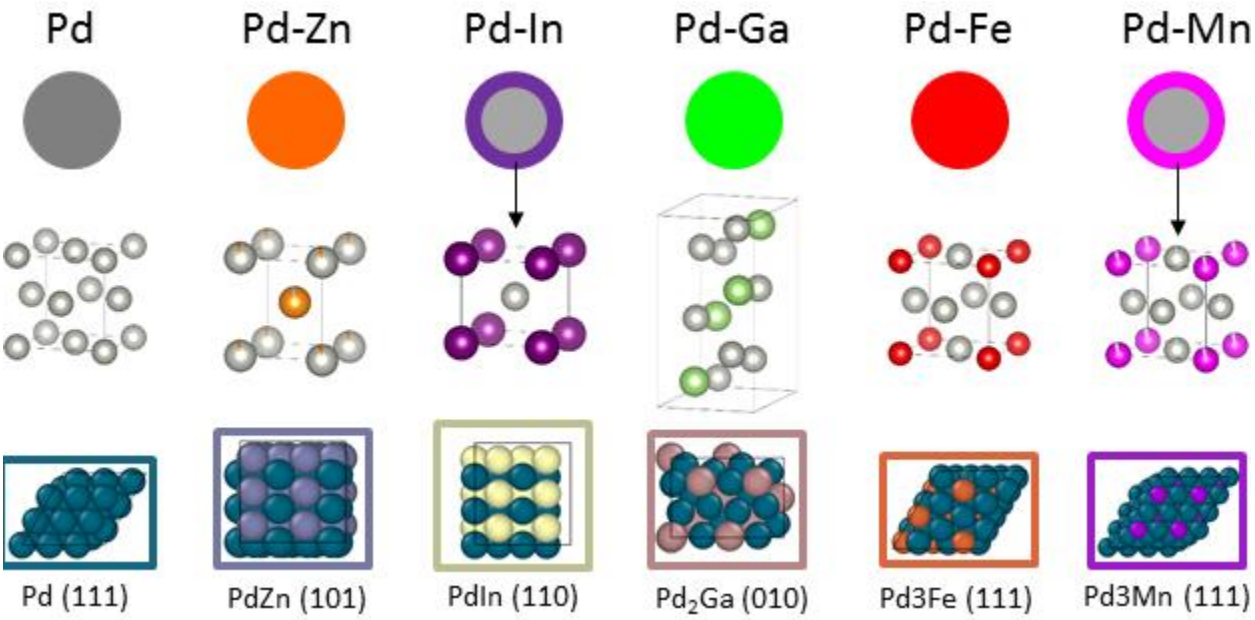

Figure 31: Structural model of Pd and Pd alloy catalysts. The PdIn and PdMn catalysts have alloy shells with a Pd core while the PdZn, PdGa and PdFe catalysts are pure phases. The unit cell of each alloy structure and the lowest energy surface are pictured beneath the respective nanoparticle models.

The catalyst structure of 2Pd-3Fe and 2Pd-3In are detailed in references [26], [129]. The 2Pd-3Fe catalyst is a pure phase Pd_3Fe alloy, based on the in-situ synchrotron XRD pattern and matching atomic Pd environment measured by XAS. The Pd-In catalyst had a Pd core and alloy shell of the Cubic PdIn phase with a CsCl structure. Pd-In and Pd-Pd scattering cannot be distinguished by EXAFS, but the XRD pattern showed weak peaks from the PdIn phase and the similarity in dehydrogenation selectivity between the core shell catalyst and a pure phase PdIn alloy sample suggests they have the same surface structure. The XRD pattern for 2Pd-3Zn showed that palladium and Zinc form the β_1-PdZn alloy phase. The formation of the β_1-PdZn phase in nanoparticle bimetallic Pd-Zn catalysts has been reported and is consistent with the present results [25], [48]. Consistent with the XRD result, the Pd K edge EXAFS showed exclusively Pd-Zn nearest neighbors and Pd-Pd scattering at an elongated distance. The 2.5Pd-2.5Ga catalyst was verified to form the Pd_2Ga phase with the Co_2Si structure, consistent with other literature reports on Pd-Ga bimetallics [140]. The Pd K edge EXAFS reflected the Pd_2Ga

structure in the Pd-Ga:Pd-Pd coordination number ratio witch closely matched that of Pd in Pd_2Ga. The 1Pd-5Mn formed a Pd-Mn bimetallic as shown by EXAFS, but the low Pd loading and small particle size did not allow for collection of XRD spectra even by synchrotron XRD. The catalyst was verified to have a core shell structure by difference XAS, which showed that the particle shell is manganese rich with respect to the total particle composition. The Pd-Mn/Pd-Pd neighbor ratio in the nanoparticle matched that of Pd_3Mn, which has an $AuCu_3$ structure. The formation of a shell layer of intermetallic also occurred in 2Pd-3In, and has been reported for other nanoparticle alloy systems resulting from the mechanism of alloy formation which involves the inward solid state diffusion of the promoter and a progressively shrinking monometallic core [31], [90], [141], [142].

In an intermetallic compound, the active metal ensemble size is determined by the crystal structure and atomic plane. This is in contrast to a solid solution, where the lack of ordering leads to a distribution of ensemble sizes and the number of active metal-promoter bonds. In FCC metals the lowest energy surface is typically the (111) plane. For the alloys with FCC symmetry (Pd_3Fe, Pd_3Mn) the (111) surface is composed of interconnected groups of 3 Pd atoms. In the tetragonal β_1-PdZn phase of PdZn, the (101) has isolated Pd atoms which resulted in only linearly bound CO when measured by IR [48]. The Pd-In catalyst also showed only linearly bound CO by FTIR, which is due to the CsCl structure of PdIn where the low energy (110) crystal plane also has only isolated Pd atoms [26]. On the (010) surface, Pd still has Pd neighbors, but at a bond distance longer than Pd metal (2.75 Å for Pd, 2.81 and 2.85 Å for Pd_2Ga).

The effect of active metal ensemble size on the rate of hydrogenolysis has been demonstrated in solid solution systems by varying the percentage of active metal [21]. As the average ensemble size is decreased, the rate of hydrogenolysis decreases. The decrease in the rate of hydrogenolysis is reflected in the increased selectivity of the alloy catalysts with respect to the monometallic Pd catalyst of the same size. Although all Pd alloy catalysts are significantly more selective than monometallic Pd, there are slight differences in selectivity depending on the structure and number of adjacent Pd atoms in the surface ensembles. In the alloy catalysts, the site isolated alloys, β_1-PdZn and PdIn have the highest dehydrogenation selectivity. The selectivity of the Pd_2Ga, which has a distorted 3-fold Pd ensemble with a long Pd-Pd bond distance is lower than the site isolated alloys and shows slight decrease in selectivity with

increasing conversion. The Pd_3Fe and Pd_3Mn alloys, with 3-fold Pd ensembles show the lowest selectivity among the alloys. The difference in selectivity from the most selective alloy (PdZn) and the least selective alloys (Pd_3Mn, Pd_3Fe) was only 10%, with all alloys showing selectivity at 20% conversion above 90%. The initial dehydrogenation turnover rate for the alloys only varied by a factor of 2, and such a small difference should be considered within the error of reproducibly determining turn over rates in a reaction with fast deactivation [88]. Because all the dehydrogenation turnover rates for the alloys are similar, the difference in selectivity comes from changes the rate of hydrogenolysis. An increase in selectivity from 90 to 99% requires that the rate of hydrogenolysis decrease by about an order of magnitude, with the dehydrogenation rate being constant. So, while the difference in selectivity between the site isolated alloys and those without is moderate, the difference in the hydrogenolysis rate is large.

Because the structure of the alloy determines the local Pd coordination in an intermetallic compound, it also determines the electronic effect, and the two effects cannot be decoupled. In addition to the difference in ensemble size between the alloys, they also differ in the number of surface Pd-Pd and Pd-promoter bonds. The Electronic effect occurs due changes in the local coordination sphere of the surface atoms, and the number of bonds changes the strength of the electronic modification. This has been demonstrated in the Pt-Mn system, where the subsurface alloy or Pt layer of the catalyst changed the CO heat of adsorption of the Pt_3Mn surface [114]. In the site isolated PdZn alloy, each surface Pd atom on the lowest energy surface has 6 heteroatomic bonds (4 surface, 2 subsurface) and 2 Pd second nearest neighbors at a non-bonding distance (2.89 Å); PdIn has the same number of herteroatomic bonds but 6 Pd second nearest neighbors at 3.22 Å. Pd atoms on the (010) surface of Pd2Ga have 3 Ga neighbors (2 surface, one subsurface) with 4 Pd nearest neighbors at an elongated bond distance (2.8, 2.85 Å). Lastly, surface atoms in the Pd_3M structures have 3 promoter nearest neighbors (2 surface, 1 subsurface) with 6 Pd-Pd bonds equal in length to the Pd-promoter bonds. As the local coordination changes, the d band of palladium is modified, which is quantified in the first and second moments of the d band. In general, as the number of Pd-promoter bonds increases, the d band shifts away from the fermi level and increases in width (see table 25).

While L_3 edge XANES is commonly used to demonstrate d-band modification in platinum, the same information cannot be gained at the Pd L_3 edge due to the electron configuration of Pd. Because Pd metal is d_{10}, there are no unfilled d states, and the L_3 edge

XANES cannot give information about the d-band. The lowest energy unfilled state accessible by the dipole selection rules of XANES is the 5s unfilled states. The change in whiteline shape observed for the alloys reflects the unfilled s states redistributing in energy due to overlap with neighboring promoter s orbitals, similar to how the 5d unfilled states in platinum are modified by promoters in platinum alloys [33].

The current dataset of alloy phases and their selectivity allows for refinement of selectivity descriptors calculated by DFT. A good descriptor should predict alloys with and without site isolation are more selective than palladium, and that site isolated alloys are more selective than those without. A frequently used dehydrogenation selectivity descriptor, which is calculated as the difference in energy between desorption of the alkene and the first deep dehydrogenation C-H bond activation energy is shown in table 23. The underlying assumption of the selectivity descriptor is that hydrogenolysis occurs on deeply dehydrogenated species, and thus weaker olefin adsorption favors high olefin selectivity. The computed selectivity descriptor correctly predicts that site isolated alloys are more selective than palladium, but only predicts a small improvement in selectivity for the Pd_3M alloys, which experimentally also show high selectivity.

In kinetic models of hydrogenolysis, all deeply dehydrogenated species are quasi-equilibrated with the adsorbed alkene, which would suggest that the first deep dehydrogenation barrier is not the proper point of divergence in the reaction pathway [14], [143]. The C-C bond breaking step is the rate limiting step and is effectively irreversible [15]. The gas phase product selectivity is a ratio of the dehydrogenation and hydrogenolysis rates, and as such, a proper selectivity descriptor should involve the rate limiting steps of the two reactions to properly capture trends in selectivity among different phases. The problem then becomes determining which deeply dehydrogenated species controls the rate of hydrogenolysis, which would also be a function of the reaction conditions (temperature, H_2 pressure, H_2:alkane feed ratio) at which the reaction is performed [14], [109], [110], [144]. In the case of the reaction conditions typical of dehydrogenation (high temperature, low H_2:alkane feed ratio), equilibrium would favor a more deeply dehydrogenated reactant pool as hydrogen surface coverage is expected to be low. Microkinetic models of the dehydrogenation and hydrogenolysis network on platinum have also shown that hydrogenolysis predominantly occurs through propynyl [139]. With this justification, the C-C bond breaking barrier for propyne is considered to illustrate the importance of

considering C-C bond cleavage in the selectivity descriptor of dehydrogenation. The total barrier for C-C bond cleavage of propyne in the Pd_3M alloy structures is doubled as compared to monometallic Pd, and correctly increases in magnitude for the alloys with more promoter neighbors (Pd_2Ga) and the site isolated alloys (PdIn, PdZn). While propyne might not necessarily be the rate controlling species in hydrogenolysis on the alloy surfaces, the trends in C-C bond breaking activation energy between alloys are directionally correct and appear to correlate with the olefin selectivity of these alloys.

3.6 Conclusion

Simple synthetic methods such as strong electrostatic adsorption and incipient wetness impregnation allowed for the synthesis of 1-2 nm intermetallic compounds between palladium and five different promoters: Zn, Ga, In, Fe and Mn. The alloys palladium forms with zinc and indium are site isolated and showed higher selectivity than those that were not site isolated (Ga, Fe, Mn). Alloys without site isolation had selectivity higher than monometallic Pd and had the same increase in dehydrogenation turnover rates seen in the site isolated alloys. The change in selectivity and turnover rate resulted from the heteroatomic bonds between palladium and the promoter, which results in both structural and electronic changes to the catalyst. While the site isolated alloys showed the highest selectivity, they also showed the largest electronic modification, and the two effects cannot be effectively decoupled to determine which plays a dominating role in determining selectivity. Computed selectivity descriptors used for platinum and platinum alloys involving the desorption energy and the first deep dehydrogenation C-H bond activation energy barrier correctly showed that site isolated alloys are expected to have higher selectivity than Pd, but only show weak improvements for Pd alloys without site isolation. A new selectivity descriptor involving the rate limiting step in hydrogenolysis (C-C bond cleavage) more accurately predicts that non-site isolated alloys would show increased dehydrogenation selectivity. The relation of the selectivity descriptor to the reaction mechanism implies that it can be extended to other catalysts having the same dehydrogenation and hydrogenolysis mechanisms, such as base metal alloys and metal phosphides.

3.7 Acknowledgments

This paper is based upon work supported in part by the National Science Foundation under Cooperative Agreement No. EEC-1647722. Use of the advanced photon source was supported by the U.S. Department of Energy, Office of Basic Energy Sciences, under contract no. DE-AC02-06CH11357. MRCAT operations, beamline 10-BM and 10-ID, are supported by the Department of Energy and the MRCAT member institutions. The authors also acknowledge the use of the 9-BM and 11-ID-C beamline at the advanced photon source.

4. INSIGHT INTO ELECTRONIC STRUCTURE OF PLATINUM ALLOYS BY RESONANT INELASTIC X-RAY SCATTERING

This chapter represents a draft of a manuscript currently under revision for publication.

4.1 Introduction

Bimetallic catalysts have been used in many important chemical reactions. The widespread industrial use and academic study is a result of bimetallics outperforming their monometallic constituents in one or more important metrics such as rate, selectivity or life [122]. The modification of performance compared to monometallic catalysts has been explained based on electronic modification of the active metal, which can result in weakening in adsorbate binding energies and increased barriers for certain reactions as calculated by DFT [29]. By selectively decreasing the binding energy of one type of adsorbate over another, the selectivity to a given product can be improved. In the case of selective hydrogenation of acetylene, alloying weakens the binding strength of ethylene, preventing over-hydrogenation to ethane [145]. In dehydrogenation, alloying weakens the binding strength of the alkene and deeply dehydrogenated species, which may contribute to their improved selectivity and coking resistance [131]. These changes are qualitatively explained by d-band theory, which correlates adsorbate binding strengths to the energy of the d-band center relative to the Fermi level [28]. As the d-band center moves further from the Fermi level, adsorbate binding strength weakens.

While, d-band theory was originally used to explain trends in adsorbate binding on pure metals, it has been extended to alloys quite successfully. The addition of the second metal modifies the d-band of the catalytic metal and causes the accompanying decrease in adsorbate binding strength [29]. Measurement of valence band photoemission spectra of bulk polycrystalline alloys has verified the modification of the d-band and replicated the trend seen computationally that early transition metals more strongly modify the d band through loss of density near the Fermi energy [55]. Weakening of adsorbate binding strengths has been

experimentally observed on single crystal alloy catalysts measured by TPD and by microcalorimetry on supported nanoparticle alloy catalysts [42], [146].

The great utility of d band center electronic descriptor developed in d-band theory comes from its broad applicability which allows for computational screening of many structures and alloys to then guide synthetic efforts. Paired with scaling relationships, optimal catalyst compositions have been proposed for several catalytic systems [147]. Recently, Cybulskis et al. reported a Pt-Zn intermetallic alloy catalyst for dehydrogenation which showed improved alkene selectivity and turnover rate for propane dehydrogenation [24]. While the d band of the alloy changed in shape, the d band center did not shift appreciably, which seemingly contradicts established relationships between the d band center and catalytic performance.

While measurement of the d band center is commonplace computationally, it is relatively inaccessible by experiment. Valence band photoemission is limited in its applicability beyond unsupported metals due to the strong contribution of the support to the spectra. Recently hard x-ray valence band photoemission has extended the applicability of the technique to carbon supported alloy catalysts at high loadings [148], but as of yet has not been demonstrated on oxide supported catalysts at technical loadings. Resonant inelastic X-ray scattering has recently been used to measure the energy of filled valence 5d states in such systems, which allows for a stronger connection to be made between computational descriptors and experimental measurement [24], [123]. Herein we measure the energy of the filled and unfilled valence 5d states by RIXS in a diverse set of platinum intermetallic compounds which have been previously reported as selective propane dehydrogenation catalysts. RIXS shows both a decrease in the energy of the filled 5d density of states and an increase in the energy of the unfilled 5d density of states. The advantage of RIXS over XPS, in which the strong coupling of the photoelectron to the core hole, is highlighted. The difference in the bonding interaction between platinum and the promoter is suggested to explain the trend in energy shifts between transition metal promoters and post transition metal promoters.

4.2 Experimental

4.2.1 Catalyst Synthesis

Bimetallic Pt-Ga catalysts were synthesized by sequential incipient wetness impregnation with a target loading of 5% Pt and 2.5% Ga. 1.25 g of 10 wt% $Ga(NO_3)_3$ solution and 1.33 g of Citric acid was dissolved in Millipore water and diluted to a solution volume of 5 ml with Millipore water and pH adjusted to 11 though the addition of 30% ammonium hydroxide. The solution was added dropwise to 5.00 g of Davasil 646 SiO_2. The Ga-SiO_2 was then dried at 125°C overnight and then calcined under flowing air at 600°C for 3 hours. 0.166 g of $Pt(NH_3)_4(NO_3)_2$ was dissolved in 1 mL of Millipore water and diluted to a total volume of 5 mL. The solution was pH adjusted to 11 with 30% ammonium hydroxide and added dropwise to the calcined Ga-SiO_2. The catalyst was dried at 125°C overnight and calcined at 350°C for 3 hours. The Pt-Ga catalyst was then reduced at 200C in 5% H_2 (balance N_2) at 100 ccm for 30 minutes and then 600°C in the same gas for 30 minutes. The catalyst was then cooled to room temperature in N_2 and passivated in air. A monometallic 3% Pt on SiO2 catalyst was synthesized in the same manner with the Pt loading adjusted by decreasing the mass of $Pt(NH_3)_4(NO_3)_2$ used during platinum impregnation.

4.2.2 Scanning Transmission Electron Microscopy (STEM)

The particle size of the reduced catalyst was measured by STEM imaging. STEM images were collected on an FEI Titan operated in STEM mode using an accelerating voltage of 300 keV and a high angle annular dark field (HAADF) detector. Samples for STEM were dispersed in isopropyl alcohol and dropped onto an ultrathin carbon film Au TEM grid (TedPella) and subsequently dried on a hotplate at 80°C. Image processing was performed using the FIJI distribution of ImageJ software, with a minimum of 100 particles measured to give the particle size distribution [133].

4.2.3 In-Situ X-ray Absorption Spectroscopy

In-Situ XAS at the Pt L_3 edge (11564.0 eV) was performed at the MRCAT bending magnet line (10BM) of the advanced photon source. Samples were measured in transmission mode using a set of 3 ion chambers, which allowed for simultaneous measurement of the sample and a reference foil. Samples for XAS were ground in a mortar and pestle and pressed into a

stainless steel sample holder. Samples were treated in a quartz tube reactor with Kapton windows and valves for gas flow. Catalysts were pretreated at 550°C for 30 minutes in 3.5% H_2. The reactor was then purged at temperature for 5 minutes with UHP Helium which was further purified using a Restek oxygen and water trap before cooling to room temperature in the same gas. The reactor atmosphere was then isolated using 3-way ball valves and transferred to the beamline for analysis.

XAS data analysis was performed using WinXAS software. Experimental phase and amplitude functions for Pt-Pt scattering was extracted from Pt foil (12 neighbors, 2.77 Å). Phase and amplitude functions for Pt-Ga scattering was generated using FEFF6 with a bond distance of 2.75 Å using the amplitude reduction factor (0.79) and Debye-Waller factor (0.004 $Å^2$) fit for the platinum foil. EXAFS data was k^2 weighted and Fourier transformed over k range of 2.6-12 $Å^{-1}$ and the first shell scattering was isolated over an R range of 1.5-3.25 Å. Fitting was performed over the R range of the first shell isolation using a least squares approach allowing the coordination number, bond distance and Debye-Waller factor to vary.

4.2.4 In-Situ Synchrotron X-ray Diffraction

In-Situ Synchrotron X-ray Diffraction measurements were performed at the 11ID-C beamline at the advanced photon source. Data was acquired in transmission mode using an X-ray wavelength of 0.117418 Å (105.091 keV) and a Perkin-Elmer large area detector. Samples were pressed into a thin pellet and loaded into a Linkam Thermal Stage, which allowed reactant gas flow during in-situ XRD measurement. The cell was purged with He for 5 minutes before flowing 100 ccm of 3.5% H_2 (balance He) and ramping the cell temperature to 600°C for 20 minutes. Diffraction patterns were collected at high temperature and the sample was then cooled to 35°C under gas flow and diffraction patterns were collected again. The SiO_2 support and empty cell were treated by the same procedure and scanned for background subtraction. 2D diffraction patterns were integrated using Fit2D software, giving standard powder patterns [63], [149]. Diffraction patterns of Pt-Ga phases were simulated using MAUD using reference CIF files from ICSD [65], [150].

4.2.5 Resonant Inelastic X-Ray Scattering

RIXS spectra were collected on the MRCAT insertion devise line (10ID) line of the advanced photon source. The silica supported catalyst was ground to a fine powder and pressed into a self-supporting wafer inside of a stainless steel sample holder. Sample treatment was performed in a purpose-built in-situ cell capable of heating and gas flow, described elsewhere [61]. Collection of transmission X-ray absorption and X-ray Emission spectra was made possible by three kapton windows in the cell. Samples were reduced at 550°C in 3.5% H_2 (balance He) for 30 minutes and then cooled to 100°C in 3.5% H_2 (balance He) for measurement.

During RIXS measurements, the X-ray beam was microfocused using a set of Kirkpatric-Baez mirrors. X-ray Absorption at the Pt L_3 edge was measured using a set of ion chambers and the $L\beta_5$ (L_3-$O_{4,5}$) X-ray emission line was measured using a bent crystal spectrometer [62]. The wavelength dispersive spectrometer was based on a bent silicon crystal. Fluoresced X-rays were detected using a Pilatus 100K (Dectris) 2D pixel array detector. The analyzer crystal used was a 55-µm thick Si (400) wafer cylindrically bent with an approximate bend radius of 0.5 m. X-rays were scattered from the Si(133) plane with a calculated asymmetry angle of 13.76°. The crystal analyzer was declined 20° from the sample horizontal to allow enough elastically scattered X-rays through the analyzer that the fluorescence energy scale could be calibrated based on the elastic scattering peak position. The intensity of the elastically scattered peak was approximately 5x that of the inelastic scattering peak. RIXS maps were then plotted as fluorescence intensity maps as a function of incident photon energy (abssica) and emission energy relative to the elastic scattering peak (ordinate), hereafter termed energy transfer, with the elastic scattering maximum corresponding to 0 energy transfer. The elastic scattering peak was subtracted from the RIXS maps by fitting a Gaussian curve to the truncated data, using a fixed value for the full width at half maximum (FWHM) and peak position per sample, and a linearly varying amplitude with incident photon energy to account for beam polarization changing the elastic scattering amplitude as a function of emission angle.

4.2.6 X-Ray Photoelectron Spectroscopy

XPS measurements were made on a Kratos Axis Ultra Imaging DLD spectrometer. Before measurement, the catalysts were treated in a catalytic cell (CatCell) attached to the spectrometer, which allowed for gas treatment and transfer to the spectrometer without exposing the catalysts

to oxygen. Monochromated Al Kα (1486.69 eV) X-rays were used, and photoelectrons were measured using a hemispherical electron energy analyzer operated with a constant pass energy of 20 eV. Differential charging was mitigated using a built in Kratos charge neutralizer. Before measurement, catalyst samples were pretreated in 5% H2 (balance Ar) for 30 minutes at 550°C; sample were then transferred under UHV to the analysis chamber for measurement. The base pressure of the CatCell and analysis chamber was $4x10^{-8}$ and $2x10^{-9}$ Torr respectively. Data analysis was performed using CasaXPS software. The binding energy scale was charge corrected by setting the binding energy of the Si 2p line to 103.7 eV. The Pt 4f photoemission peaks were fit using an asymmetric Lorentzian function (LF(a,b,c,d)) and a Shirley background. Fits of the Pt 4f 7/2 and 5/2 components were constrained to have the same full width at half maximum (FWHM) and the peak area ratio for the two components was fixed at 0.75, the peak position, area and full width at half maximum were allowed to vary.

4.3 Results

4.3.1 Characterization of Pt-Ga

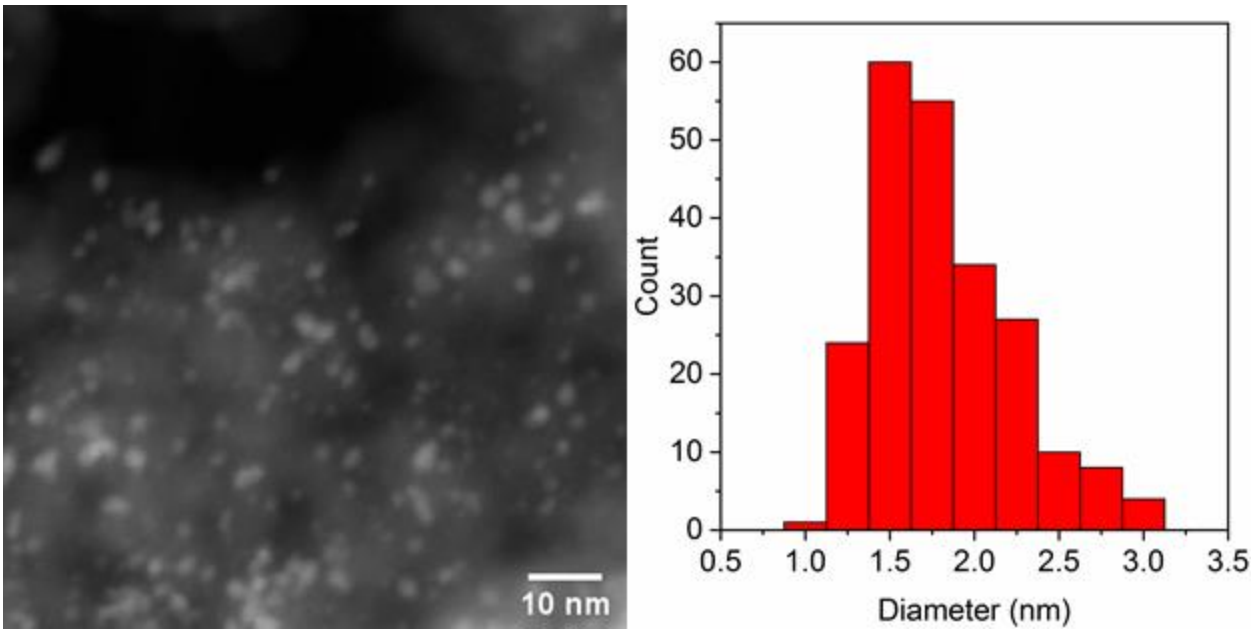

Figure 32: STEM image (left) and number average particle size distribution (right) of 5Pt-2.5Ga.

Metal nanoparticle size was measured on catalysts after reduction at 550°C and subsequent exposure to air. The number average particle size for the 5Pt-2.5Ga catalyst was

1.8±0.5 nm. Figure 32 shows the number average particle size distribution and a representative STEM image for 5Pt-2.5Ga. The metal particle size is comparable to all other Pt alloy catalysts measured in this study. The monometallic Pt catalyst had a particle size of 2.1±0.6 nm.

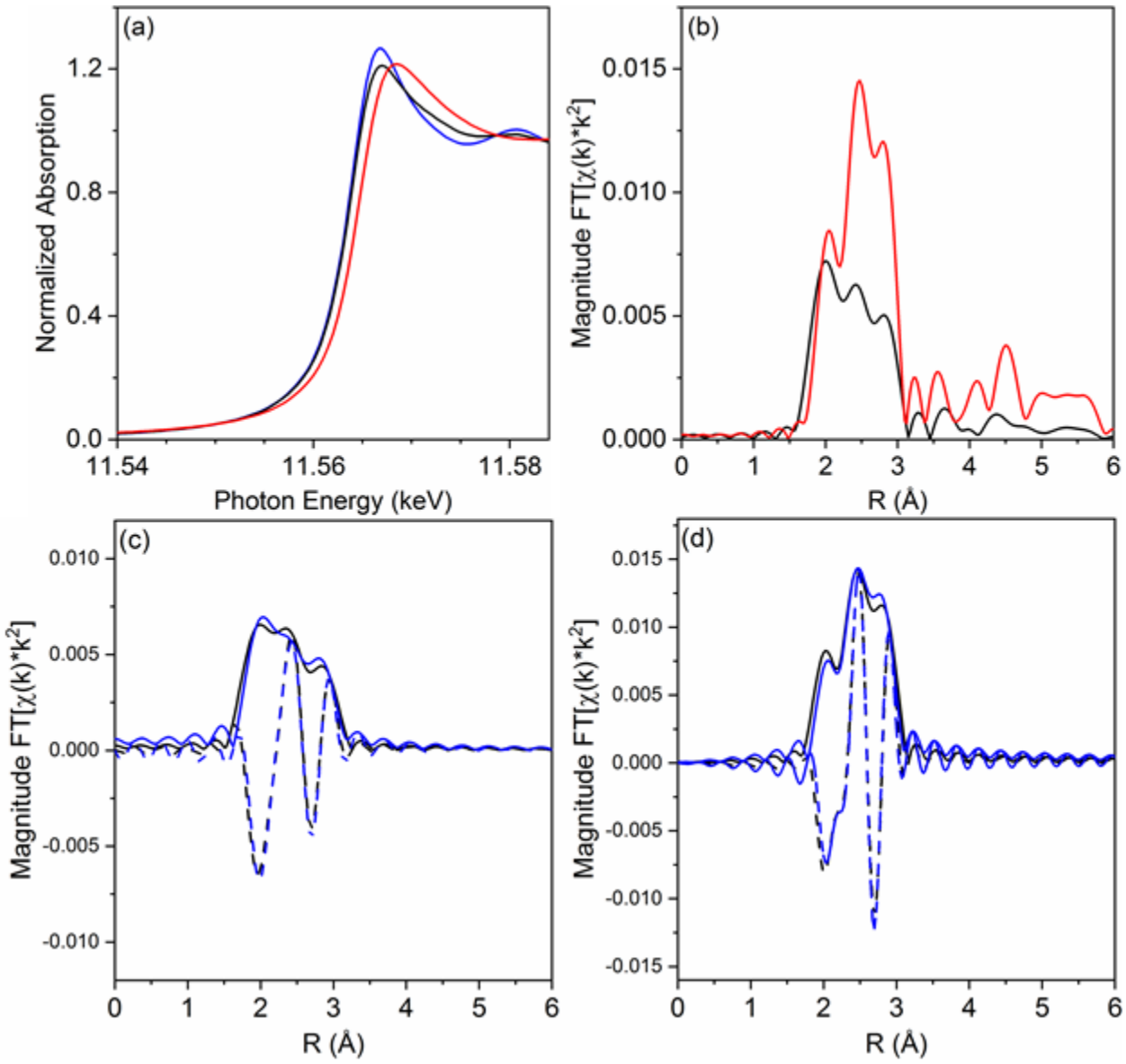

Figure 33: XANES and EXAFS results for Pt and Pt-Ga catalysts. (a) Pt L3 edge XANES for a 3Pt (black) 5Pt-2.5Ga (red) and Pt foil (blue). (b) EXAFS of 3Pt (black) and 5Pt-2.5Ga (red). R space EXAFS fits of 5Pt-2.5Ga (c) and 3Pt.

In-Situ XAS measurements at the Pt L_3 edge were performed to determine if a bimetallic formed. Figure 33a shows the X-ray absorption near edge structure (XANES) for a monometallic catalyst and the bimetallic 5Pt-2.5Ga catalyst. The edge energy of the Pt catalyst is 11564.0 eV, consistent with metallic platinum. The Pt-Ga catalyst has an edge energy shifted to 11564.5 eV and the white line is broadened, consistent with a change in the energy distribution of the unfilled 5d states resulting from alloy formation.

Table 26: Pt L3 edge EXAFS fits of Pt and Pt-Ga.

Sample	XANES edge energy (eV)	Path	CN	R (Å)	DWF (Å^2)	E_0 (eV)
Pt foil	11564.0	Pt-Pt	12	2.77	0	0
3Pt	11564.0	Pt-Pt	8.8	2.74	0.002	-0.8
5Pt-2.5Ga	11564.8	Pt-Pt	5.7	2.75	0.003	-3.8
		Pt-Ga	2.5	2.50	0.006	-7.5

Figure 33b shows the R space EXAFS spectra of 3Pt and 5Pt-2.5Ga. The monometallic Pt catalyst has 3 peaks typical of scattering from platinum neighbors. The first shell scattering envelope for the Pt-Ga catalyst changes relative to the monometallic Pt catalyst due the incorporation of Pt-Ga scattering. The Pt-Ga catalysts still has 3 peaks, but the position is shifted to lower R values and the relative intensity of each is modified relative to platinum: the first (low R) peak in the Pt-Ga catalyst is close to the same height as the middle peak, whereas the low R peak in the Pt spectra is the lowest peak and the middle peak is the highest. Fitting the monometallic Pt catalyst shown in table 26 gave a Pt-Pt coordination number of 8.8 at a bond distance of 2.74. Fitting the Pt-Ga catalyst gave a Pt-Pt coordination number of 4.9 at a distance of 2.74 Å angstroms and a Pt-Ga coordination of 1.7 at a bond distance of 2.48 Å.

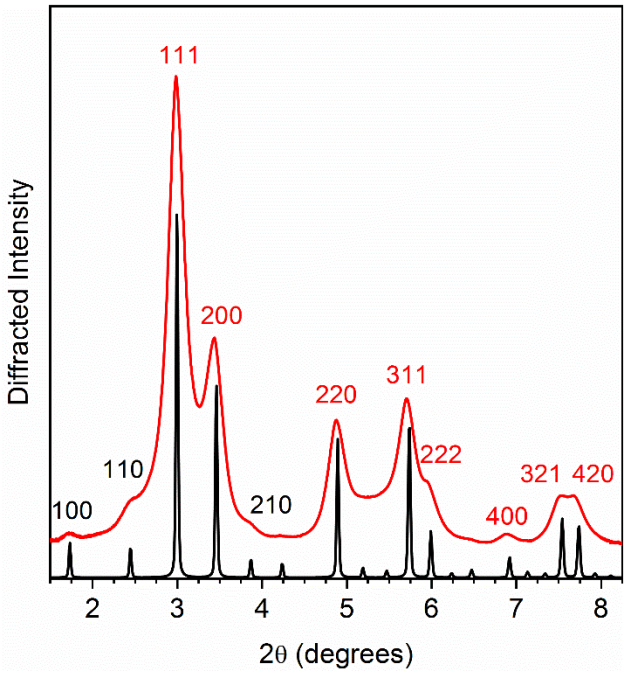

Figure 34: In-situ Synchrotron XRD pattern of 5Pt-2.5Ga (red) and Pt3Ga standard simulation with a lattice parameter of 3.89 Å. Superlattice diffraction peaks are labeled in black and primary reflections are labeled in red.

The phase composition of the bimetallic Pt-Ga catalyst was determined by in-situ synchrotron XRD. Figure 34 shows the powder XRD pattern for 5Pt-2.5Ga as well as simulated XRD patterns of Pt_3Ga. The diffraction peaks are broad due to the small particle size. The 2 theta range over which the typical primary reflections occur is much smaller than in a laboratory XRD pattern due to the high X-ray energy used (105.091 keV). The 5Pt-2.5Ga catalyst shows primary reflections typical of an FCC lattice. Four peaks are clearly resolved, (111), (200) (220) and (311), but in addition superlattice diffraction peaks are evident in the 5Pt-2.5Ga catalyst: (110), (210) and (211), which are indicative of an $L1_2$ ($AuCu_3$) structure. The presence of the superlattice diffraction peaks and FCC primary reflections are consistent with the Pt_3Ga intermetallic phase. Nevertheless, the two patterns do not match perfectly. Compared to the standard Pt_3Ga pattern, the peaks in the 5Pt-2.5Ga are shifted to lower angle (0.006° for the most intense peak). The (111) and (220) peak maxima have the least overlap by neighboring peaks and are used to calculated the lattice parameter. The peak position of the (111) and (220) peaks is 2.983° and 4.873° respectively, both giving a lattice parameter of 3.90 Å., which is larger than the 3.892 Å given by the Pt_3Ga standard, such a difference cannot be accounted for by a nanoparticle size effect, where the large fraction of undercoordinated surface atoms causes a

decrease in the lattice parameter. A plausible explanation is micorstrain caused by the presence of a thin shell layer of a second phase with a larger lattice parameter which cannot be resolved by synchrotron XRD. This interpretation is consistent with the EXAFS results which show a local platinum environment which is platinum rich with respect to that expected for Pt_3Ga.

4.3.2 Resonant Inelastic X-ray Scattering

The particle size, phase composition and phase purity of Pt_3V, Pt_3Mn, Pt_3Fe, Pt_3Co, Pt_3In, and PtZn are described in reference [24], [31], [114]. The energy transfer maximum and Pt L3 edge XANES edge energy for PtZn is reproduced from reference [24].

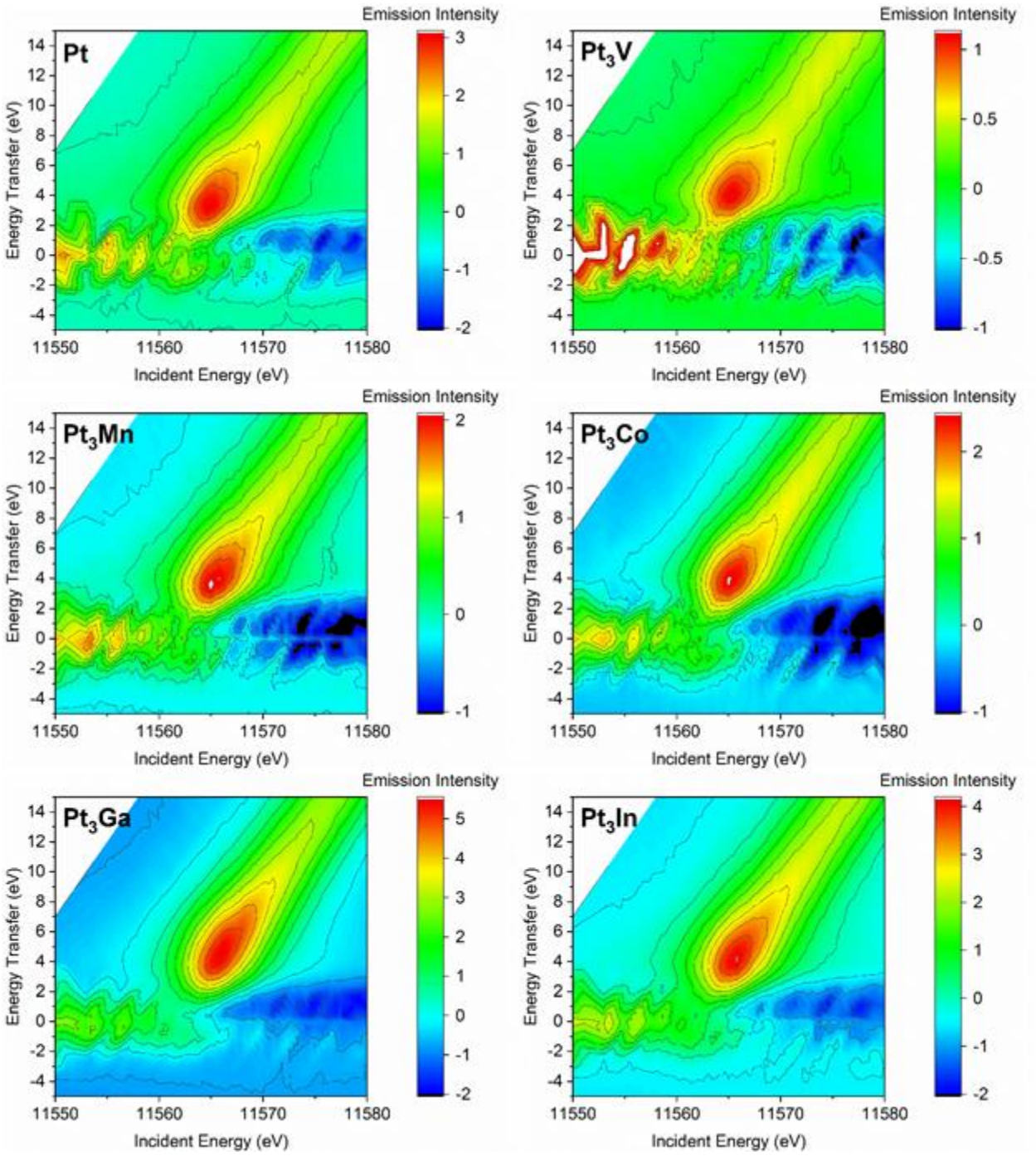

Figure 35: RIXS plots of Pt and Pt alloy catalysts after reduction at 550°C in 3.5% H2.

RIXS plots of Pt, Pt_3V, Pt_3Mn, Pt_3Co, Pt_3In and Pt_3Ga are shown in figure 35. RIXS maps are plotted as a function of the incident photon energy on the horizontal axis, and the fluoresced photon energy relative to the elastic scattering energy, termed energy transfer, on the

vertical axis. The plotted intensity is that of the fluoresced X-rays resulting from scattering. Elastic scattering occurs when the excited $2p_{3/2}$ electron decays back into its own core hole. For clarity, the elastic scattering peak has been subtracted, and residual fluctuations at 0 energy transfer are artifacts from the subtraction. Inelastic scattering occurs when an electron other than the excited $2p_{3/2}$ electron decays back into the core hole. The bent crystal geometry of the spectrometer used in this study allows for the selective measurement of fluorescence from the $L\beta_5$ decay mode (L_3-$O_{4,5}$), which corresponds to a $5d_{3/2}$ or $5d_{5/2}$ electron filling the core hole. Fluorescence from the $L\beta_5$ decay mode manifests in the RIXS plots as a broad maximum with the onset near the L_3 absorption edge of the respective material at an energy transfer value greater than zero. For platinum, the inelastic peak maximum occurs at an energy transfer value of 3.2 eV. Because the $L\beta_5$ probes all filled d states, and the L_3 edge probes all unfilled d states, the energy transfer maximum represents the energy separation between the weighted average energy of the filled 5d states and the weighted average energy of the unfilled 5d states. The broadness of the inelastic scattering peak reflects the width of the d band in platinum and platinum alloys. In the alloy samples, the energy transfer maximum is shifted to higher values (see table 27), meaning the energy of both the filled and unfilled states further separate in the alloys. The shape of the inelastic scattering peak also changes, which reflects the changing distribution of states in energy in each alloy phase. As the incident photon energy increases past the L_3 absorption edge, the resonant enhancement of the $L\beta_5$ fluorescence mode decays, leading to a loss of intensity and the diagonal tail of the inelastic scattering peak.

Table 27: Energy transfer maximum values and Pt L3 edge XANES edge energy values for Pt and Pt alloy phases

Phase	Energy Transfer (eV)	XANES edge energy (eV)
Pt	3.2	11564.0
Pt_3V	4.1	11564.5
Pt_3Mn	3.6	11564.3
Pt_3Fe	3.5	11564.2
Pt_3Co	3.9	11564.6
Pt_3Ga	4.6	11564.8
Pt_3In	4.2	11564.8
PtFe	3.7	11564.4
$PtFe_3$	3.8	11564.6
PtZn	4.5	11564.8

The energy transfer values for the platinum alloys with post transition metals (In, Ga, Zn) are larger than those alloys with 3d elements, even in Pt_3In and Pt_3Ga where Pt has the same number of Pt-promoter bonds as in the 3d $AuCu_3$ structures. For the Pt alloys with the 3d metals, vanadium and cobalt show the largest energy transfer values, while iron and manganese had the smallest increase in energy transfer of the alloys measured.

Table 28: Pt 4f7/2 fit details and calculated Pt 4f7/2 core level shifts for Pt and Pt alloys after a reduction pretreatment at 550°C in 5% H2.

Sample	Pt $4f_{7/2}$ binding energy (eV)	Pt $4f_{7/2}$ FWHM (eV)	Pt 4f spin orbital splitting (eV)	Core level shift (eV)
Pt	70.9	2.0	3.4	-
Pt_3V	71.3	2.2	3.5	0.4
Pt_3Mn	71.0	1.7	3.3	0.1
Pt_3Fe	71.4	2.0	3.4	0.5
Pt_3Co	71.5	2.1	3.4	0.6
Pt_3Ga	71.6	1.9	3.4	0.7
Pt_3In	71.3	1.9	3.3	0.4
PtZn	71.7	1.9	3.3	0.8

Table 28 shows the Pt $4f_{7/2}$ binding energy for Pt and 7 platinum alloys after reduction at 550°C in 5% H_2. The monometallic Pt sample had a Pt $4f_{7/2}$ binding energy of 70.9 eV and an asymmetric peak shape, consistent with metallic platinum. Similarly, the alloy samples also had asymmetric peak shapes, but the Pt $4f_{7/2}$ binding energy was shifted to higher binding energy.

The core level shift for each alloy was calculated as the difference in Pt $4f_{7/2}$ binding energy between the alloy and the monometallic platinum. All of the alloys had a positive core level shift, which is consistent with platinum in the alloy being electronically modified. The varying magnitude of the core level shifts for each alloy reflects the different electronic modification inherent to the heteroatomic bonds present in each phase.

4.4 Discussion

Pt_3V, Pt_3Mn, Pt_3Fe, Pt_3Co, Pt_3In and Pt_3Ga all have the same $AuCu_3$ crystal structure. By virtue of the common structure, platinum in each catalyst has the same number of Pt-Promoter bonds. This is important for considering trends in electronic modification because the number of Pt-Pt and Pt-M bonds that platinum has dictates the electronic modification. The importance can be seen in the density of states of surface platinum atoms in Pt_3V alloy layers of different thickness [151]. Large changes in the density of states are seen when first nearest neighbors are change from Pt to V, but only small changes are seen when second nearest neighbors are switched. In alloys of different structure, the number of Pt-Pt and Pt-promoter bonds is different, and the unequal number of bonds in each must also be considered in understanding the trends of electronic modification by different promoters. By comparing different alloys with the same structure, the electronic effect can be modified while the structure is held constant, allowing for the geometric and electronic effect to be decoupled to a large extent. Holding structure constant does not fully control for geometry, as the Pt-Pt and Pt-Promoter bond distances in each alloy are not the same, varying from 2.74 Å for Pt_3V to 2.82 Å for Pt_3In. While the bond distance will affect the amount of orbital overlap between nearest neighbors, the variation between the alloys considered here is not large and is expected to be of secondary importance compared to the promoter identity.

The ability of RIXS to probe the filled 5d states comes from the measurement of the $L\beta_5$ fluorescence line and the specificity in fluorescence line measurement afforded by a wavelength dispersive detector. Above the L_3 adsorption edge, any dipole allowed electron transition can fill the 2p core hole, but because each transition is separated in energy, a wavelength dispersive detector allows for measurement of a single decay mode. The dipole transition for the $L\beta_5$ decay mode allows for either a $5d_{5/2}$ or $5d_{3/2}$ electron to fill the $2p_{3/2}$ core hole, meaning that all 5d electrons can be probed by L_3-$L\beta_5$ RIXS. Similarly, the L_3 absorption edge allows for excitation

into the $5d_{3/2}$ (filled) and $5d_{3/2}$ (partially filled) unfilled states, meaning that all 5d unfilled states are probed at the L_3 edge. The transition probability for the absorption process is related to the density of unfilled 5d states, and similarly the transition probability for the 5d filled state into the $2p_{3/2}$ core hole is proportional to the filled 5d density of states. These proportionalities mean that the energy transfer measured by RIXS represents the energy difference between the weighted average energy of the filled states and the weighted average energy of the unfilled states.

In all cases, the RIXS energy transfer maximum in the alloys is larger than monometallic platinum, and additionally, the difference in energy transfer maximum between platinum and the alloy is larger than the XANES edge energy shift between the respective alloy and platinum. This demonstrates that the increase in splitting measured by RIXS is not solely due to an increase in the energy of the Pt 5d unfilled states, but also due to a decrease in the energy of the filled 5d states relative to monometallic platinum. The consequence for catalysis of the filled d states decreasing in energy can be explained by d-band theory, which relates the energy of the d band center relative to the Fermi level to the binding strength of adsorbates to a metal surface. As the d band center move further to the Fermi level, adsorbate binding becomes weaker. The filled 5d states moving down in energy relative to platinum would mean the creation of new states further in energy to the Fermi level, meaning that the alloys would also have a d-band center further from the Fermi level, which has been demonstrated both by DFT calculations and valence band photoemission on bulk polycrystalline alloys. The decrease in binding strengths predicted by d-band theory was seen in the Pt_3Mn catalyst, which showed a decrease in the CO heat of adsorption [114].

The electronic changes demonstrated by RIXS are a result of the bonding interactions between platinum and the promoter element. In the alloys with 3d elements, the valence 5d orbitals can readily overlap with the valence 3d orbitals of the promoter. This covalent interaction leads to the creation of bonding (filled) and antibonding (unfilled) states that are different in energy compared to those in a Pt-Pt bond, which results in the redistribution of states in the d band. On the other hand, in the alloys with post transition elements, the promoter element has a filled non-bonding d shell, and the valence is composed of s and p electrons. These electrons do not have the correct orbital symmetry to interact strongly the platinum 5d valence electrons. Instead, the modification to the platinum d band in the post transition elements comes from the 5d electrons participating less in metal-metal bonding interactions. The loss of Pt-Pt

bonding and weak interactions between platinum's 5d electrons and the promoter valence electrons results in redistribution of the energy of 5d filled states.

The mechanism by which the promoter modifies the d band is often described as an ionic like transfer of electron density to or from platinum [30], [35]. Evidence for this theory comes from the interpretation of XPS binding energy shifts, where the initial state effect contribution of the core level shift is related to a difference in the charge on the atom, with the removal of charge being more difficult (higher B.E.) when the atom is positively charged (loss of electrons) [96], [99]. The core level shifts measured on the alloy samples all show binding energies higher than monometallic platinum. The above interpretation would conclude that platinum in the alloy has lost electrons. In contrast, the XANES edge energies of all the alloys also shift to higher edge energies, which by the same electron transfer model would be interpreted as further filling of the d band by electron transfer. If this was the case, the average energy of the filled states would also increase, which experimentally was observed not to be the case. Additionally, neither the RIXS shifts nor the XPS core level shifts correlate with the electronegativity difference between platinum and the promoter, which would be expected if electron transfer governed electronic modification. The XANES and RIXS shifts instead reflect a redistribution of the energy of filled and unfilled 5d states resulting from the changing bonding environment in each alloy [103], [105]. The XPS core level shifts cannot be interpreted by initial state effects alone. Intra- and extra- atomic relaxation, changes in the Fermi level should be considered.

4.5 Conclusion

A series of Pt_3M alloy catalysts with similar particle size were characterized by RIXS and XPS to elucidate trends in the electronic modification of platinum by different promoters in the same structure. By comparing promoters in platinum alloys of the same structure and particle size, the number of Pt-Pt and Pt-Promoter bonds is controlled and the effect of promoter identity can be independently studied. RIXS on the alloy catalysts showed an increase in the energy separation between the filled and unfilled 5d states in platinum. From the separately collected XANES measurements, the RIXS splitting is shown to be due to both an increase in the unfilled state energy and a decrease in the filled state energy. Post transition metals were shown to have larger effects on the energy distribution of filled and unfilled states as compared to transition metals, which is a result of the lack of orbital symmetry between the valence Pt 5d electrons and

the sp metal promoters. XPS core level shifts for the alloys are all positive, but do not reflect platinum being electron deficient in the alloy, but rather reflect the redistribution of states in the valence band in addition to changes in the Fermi energy and relaxation effects in the alloy.

5. SUMMARY

The collected works in this dissertation connect the nature of electronic modification of catalytic metals by heteroatomic bonds to electronic descriptors and further to consequences for the dehydrogenation reaction network. Owing to their narrowly defined stoichiometry and defined local atomic environments, intermetallic compounds are particularly suited for the study of electronic modifications in alloys. This is due to the source of electronic modification, which is the metallic bonding between the components of an alloy. Because the number of bonds of each type influences the electronic structure, ensuring that each atom has the same electronic modification allows for a stronger structure function relationship to be established. Another consequence of the nature of electronic modification is that it is short range in nature, which is reflected in the similarity in performance of the Pt-V alloys discussed in chapter two, where a pure Pt_3V nanoparticle and a 4 angstrom alloy layer on a Pt core were indistinguishable catalytically, whereas they showed small differences spectroscopically. This additionally highlights the importance of phase purity in determining the electronic modification inherent to a given alloy phase.

Using electron transfer to interpret the spectral shifts observed for alloys in XPS, XANES and RIXS leads to conflicting conclusions regarding the direction and magnitude of electron transfer. A consistent explanation for the observed changes is a redistribution of d state energies in the alloy due to changes in bond distance and the presence of heteroatomic bonds and is in agreement with ab-initio calculations on the alloys considered. The change in bond distance changes the degree of orbital overlap between neighbors, leading to more or less hybridization between neighbors. The heteroatom orbitals are energetically and spatially different from the catalytic metal, with the same consequences as changes in bond length. In the case of filled d valence or post transition metal promoters, the d electrons are low in energy and non-bonding, and the valence s and p electrons do not have the correct orbital symmetry to meaningfully hybridize with the valence d electrons of the active metal. In this case, the valence d electrons participate less in metal-metal bonding, which similarly perturbs the energy distribution of these electrons. The change in energy of the filled and unfilled 5d states in platinum can be experimentally measured by RIXS.

By perturbing the energy of the valence d electrons in platinum and palladium through heteroatomic bonding, the bonding between surface metal atoms and adsorbates is also affected. In binding sites of equivalent geometry, decreasing the average energy of the filled states led to a decrease in the binding energy of hydrogen and hydrocarbon adsorbates. This finding is in agreement with d band theory, which predicts that shifting the average energy of the d band away from the fermi energy leads to weaker adsorption. In the alloy catalysts, multiply bound adsorbates were found to be more strongly affected by electronic modification than were adsorbates which bond to a single atom. The geometry of the alloy surface plays a role in that multiply bound adsorbates are more favorably stabilized when carbon atoms assume tetrahedral coordination. In the BCT alloy, PdZn, the three-fold sites that stabilize hydrogenolysis products such as ethylidyne are not present, which changes the thermodynamics of hydrogenolysis from energetically favorable, to energetically unfavorable. Thus, while site isolation provides a path to selectivity by removing sites where hydrogenolysis is energetically favorable, alloys with the Pd_3M or Pt_3M structure are selective due to electronic modification destabilizing the hydrogenolysis pathway on a site geometry equivalent to that of the pure metal. Because the electronic effect is intrinsically tied to the site geometry and vice versa through metallic bonding, the primacy of either effect in the observed high dehydrogenation selectivity cannot be definitively stated.

REFERENCES

[1] U.S. EIA, "Annual Energy Outlook 2019 with projections to 2050," 2019.

[2] A. J. Kidnay and W. R. Parrish, *Fundamentals of Natural Gas Processing*. Taylor & Francis, 2006.

[3] A. Al-Douri, D. Sengupta, and M. M. El-Halwagi, "Shale gas monetization – A review of downstream processing to chemicals and fuels," *J. Nat. Gas Sci. Eng.*, vol. 45, pp. 436–455, Sep. 2017.

[4] K. J. Caspary, H. Gehrke, M. Heinritz-Adrian, and M. Schwefer, *Handbook of Heterogeneous Catalysis*. Weinheim, Germany: Wiley-VCH Verlag GmbH & Co. KGaA, 2008.

[5] M. . Bhasin, J. . McCain, B. . Vora, T. Imai, and P. . Pujadó, "Dehydrogenation and oxydehydrogenation of paraffins to olefins," *Appl. Catal. A Gen.*, vol. 221, no. 1–2, pp. 397–419, Nov. 2001.

[6] R. D. Cortright, P. E. Levin, and J. A. Dumesic, "Kinetic Studies of Isobutane Dehydrogenation and Isobutene Hydrogenation over Pt/Sn-Based Catalysts," *Ind. Eng. Chem. Res.*, vol. 37, no. 5, pp. 1717–1723, May 1998.

[7] Q. Li, Z. Sui, X. Zhou, and D. Chen, "Kinetics of propane dehydrogenation over Pt–Sn/Al2O3 catalyst," *Appl. Catal. A Gen.*, vol. 398, no. 1–2, pp. 18–26, May 2011.

[8] P. Cremer, C. Stanners, J. W. Niemantsverdriet, Y. R. Shen, and G. Somorjai, "The conversion of di-σ bonded ethylene to ethylidyne on Pt(111) monitored with sum frequency generation: evidence for an ethylidene (or ethyl) intermediate," *Surf. Sci.*, vol. 328, no. 1–2, pp. 111–118, Apr. 1995.

[9] F. Zaera, T. V. W. Janssens, and H. Öfner, "Reflection absorption infrared spectroscopy and kinetic studies of the reactivity of ethylene on Pt(111) surfaces," *Surf. Sci.*, vol. 368, no. 1–3, pp. 371–376, Dec. 1996.

[10] F. Zaera and D. Chrysostomou, "Propylene on Pt(111) II. Hydrogenation, dehydrogenation, and H-D exchange," *Surf. Sci.*, vol. 457, no. 1–2, pp. 89–108, Jun. 2000.

[11] A. Valcarcel, J. M. Ricart, A. Clotet, F. Illas, A. Markovits, and C. Minot, "Theoretical study of dehydrogenation and isomerisation reactions of propylene on Pt(111)," *J. Catal.*, vol. 241, no. 1, pp. 115–122, Jul. 2006.

[12] F. Zaera and D. Chrysostomou, "Propylene on Pt(111) I. Characterization of surface species by infra-red spectroscopy," *Surf. Sci.*, vol. 457, no. 1–2, pp. 71–88, Jun. 2000.

[13] M.-L. Yang, Y.-A. Zhu, C. Fan, Z.-J. Sui, D. Chen, and X.-G. Zhou, "Density functional

study of the chemisorption of C1, C2 and C3 intermediates in propane dissociation on Pt(111)," *J. Mol. Catal. A Chem.*, vol. 321, no. 1–2, pp. 42–49, Apr. 2010.

[14] D. W. Flaherty, D. D. Hibbitts, E. I. Gürbüz, and E. Iglesia, "Theoretical and kinetic assessment of the mechanism of ethane hydrogenolysis on metal surfaces saturated with chemisorbed hydrogen," *J. Catal.*, vol. 311, pp. 350–356, 2014.

[15] R. D. Cortright, R. M. Watwe, and J. A. Dumesic, "Ethane hydrogenolysis over platinum selection and estimation of kinetic parameters," *J. Mol. Catal. A Chem.*, vol. 163, no. 1–2, pp. 91–103, 2000.

[16] D. W. Flaherty and E. Iglesia, "Transition-state enthalpy and entropy effects on reactivity and selectivity in hydrogenolysis of n -alkanes," *J. Am. Chem. Soc.*, vol. 135, no. 49, pp. 18586–18599, 2013.

[17] D. W. Flaherty, D. D. Hibbitts, and E. Iglesia, "Metal-catalyzed C-C bond cleavage in alkanes: Effects of methyl substitution on transition-state structures and stability," *J. Am. Chem. Soc.*, vol. 136, no. 27, pp. 9664–9676, 2014.

[18] D. D. Hibbitts, D. W. Flaherty, and E. Iglesia, "Role of Branching on the Rate and Mechanism of C–C Cleavage in Alkanes on Metal Surfaces," *ACS Catal.*, vol. 6, no. 1, pp. 469–482, Jan. 2016.

[19] R. M. Rioux, H. Song, J. D. Hoefelmeyer, P. Yang, and G. A. Somorjai, "High-Surface-Area Catalyst Design: Synthesis, Characterization, and Reaction Studies of Platinum Nanoparticles in Mesoporous SBA-15 Silica †," *J. Phys. Chem. B*, vol. 109, no. 6, pp. 2192–2202, Feb. 2005.

[20] R. M. Watwe, R. D. Cortright, J. K. Nørskov, and J. A. Dumesic, "Theoretical Studies of Stability and Reactivity of C $_2$ Hydrocarbon Species on Pt Clusters, Pt(111), and Pt(211)," *J. Phys. Chem. B*, vol. 104, no. 10, pp. 2299–2310, 2000.

[21] J. H. Sinfelt, J. L. Carter, and D. J. C. Yates, "Catalytic hydrogenolysis and dehydrogenation over copper-nickel alloys," *J. Catal.*, vol. 24, no. 2, pp. 283–296, 1972.

[22] G. Sun, Z. J. Zhao, R. Mu, S. Zha, L. Li, S. Chen, K. Zang, J. Luo, Z. Li, S. C. Purdy, A. J. Kropf, J. T. Miller, L. Zeng, and J. Gong, "Breaking the scaling relationship via thermally stable Pt/Cu single atom alloys for catalytic dehydrogenation," *Nat. Commun.*, vol. 9, no. 1, 2018.

[23] Z. Ma, Z. Wu, and J. T. Miller, "Effect of Cu content on the bimetallic Pt–Cu catalysts for propane dehydrogenation," *Catal. Struct. React.*, vol. 3, no. 1–2, pp. 43–53, 2017.

[24] V. J. Cybulskis, B. C. Bukowski, H. T. Tseng, J. R. Gallagher, Z. Wu, E. Wegener, A. J. Kropf, B. Ravel, F. H. Ribeiro, J. Greeley, and J. T. Miller, "Zinc Promotion of Platinum for Catalytic Light Alkane Dehydrogenation: Insights into Geometric and Electronic Effects," *ACS Catal.*, vol. 7, no. 6, pp. 4173–4181, Jun. 2017.

[25] J. R. Gallagher, D. J. Childers, H. Zhao, R. E. Winans, R. J. Meyer, and J. T. Miller, "Structural evolution of an intermetallic Pd–Zn catalyst selective for propane dehydrogenation," *Phys. Chem. Chem. Phys.*, vol. 17, no. 42, pp. 28144–28153, 2015.

[26] Z. Wu, E. C. Wegener, H.-T. Tseng, J. R. Gallagher, J. W. Harris, R. E. Diaz, Y. Ren, F. H. Ribeiro, and J. T. Miller, "Pd–In intermetallic alloy nanoparticles: highly selective ethane dehydrogenation catalysts," *Catal. Sci. Technol.*, vol. 6, no. 18, pp. 6965–6976, 2016.

[27] J. K. Nørskov, "Covalent effects in the effective-medium theory of chemical binding: Hydrogen heats of solution in the <math display="inline"> <mn>3</mn> <mi>d</mi> </math> metals," *Phys. Rev. B*, vol. 26, no. 6, pp. 2875–2885, Sep. 1982.

[28] B. Hammer and J. K. Nørskov, "Electronic factors determining the reactivity of metal surfaces," *Surf. Sci.*, vol. 343, no. 3, pp. 211–220, 1995.

[29] J. R. Kitchin, J. K. Nørskov, M. A. Barteau, and J. G. Chen, "Modification of the surface electronic and chemical properties of Pt(111) by subsurface 3d transition metals," *J. Chem. Phys.*, vol. 120, no. 21, pp. 10240–10246, 2004.

[30] G. J. Siri, J. M. Ramallo-López, M. L. Casella, J. L. G. Fierro, F. G. Requejo, and O. a. Ferretti, "XPS and EXAFS study of supported PtSn catalysts obtained by surface organometallic chemistry on metals," *Appl. Catal. A Gen.*, vol. 278, no. 2, pp. 239–249, Jan. 2005.

[31] E. C. Wegener, Z. Wu, H.-T. Tseng, J. R. Gallagher, Y. Ren, R. E. Diaz, F. H. Ribeiro, and J. T. Miller, "Structure and reactivity of Pt–In intermetallic alloy nanoparticles: Highly selective catalysts for ethane dehydrogenation," *Catal. Today*, no. October 2016, Apr. 2017.

[32] P. Sun, G. Siddiqi, W. C. Vining, M. Chi, and A. T. Bell, "Novel Pt/Mg(In)(Al)O catalysts for ethane and propane dehydrogenation," *J. Catal.*, vol. 282, no. 1, pp. 165–174, Aug. 2011.

[33] N. Schweitzer, H. Xin, E. Nikolla, J. T. Miller, and S. Linic, "Establishing Relationships Between the Geometric Structure and Chemical Reactivity of Alloy Catalysts Based on Their Measured Electronic Structure," *Top. Catal.*, vol. 53, no. 5–6, pp. 348–356, May 2010.

[34] E. Nikolla, J. Schwank, and S. Linic, "Measuring and Relating the Electronic Structures of Nonmodel Supported Catalytic Materials to Their Performance," *J. Am. Chem. Soc.*, vol. 131, no. 7, pp. 2747–2754, Feb. 2009.

[35] M. T. Greiner, T. E. Jones, S. Beeg, L. Zwiener, M. Scherzer, F. Girgsdies, S. Piccinin, M. Armbrüster, A. Knop-Gericke, and R. Schlögl, "Free-atom-like d states in single-atom alloy catalysts," *Nat. Chem.*, vol. 10, no. October, 2018.

[36] J. J. H. B. Sattler, J. Ruiz-Martinez, E. Santillan-Jimenez, and B. M. Weckhuysen,

"Catalytic Dehydrogenation of Light Alkanes on Metals and Metal Oxides," *Chem. Rev.*, vol. 114, no. 20, pp. 10613–10653, Oct. 2014.

[37] M. Guisnet and P. Magnoux, "Organic chemistry of coke formation," *Appl. Catal. A Gen.*, vol. 212, no. 1–2, pp. 83–96, Apr. 2001.

[38] J. H. Sinfelt and D. J. C. Yates, "Catalytic hydrogenolysis of ethane over the noble metals of Group VIII," *J. Catal.*, vol. 8, no. 1, pp. 82–90, 1967.

[39] R. D. Cortright, J. M. Hill, and J. a Dumesic, "Selective dehydrogenation of isobutane over supported Pt/Sn catalysts," *Catal. Today*, vol. 55, no. 3, pp. 213–223, Jan. 2000.

[40] P. Sun, G. Siddiqi, M. Chi, and A. T. Bell, "Synthesis and characterization of a new catalyst Pt/Mg(Ga)(Al)O for alkane dehydrogenation," *J. Catal.*, vol. 274, no. 2, pp. 192–199, Sep. 2010.

[41] G. Siddiqi, P. Sun, V. Galvita, and A. T. Bell, "Catalyst performance of novel Pt/Mg(Ga)(Al)O catalysts for alkane dehydrogenation," *J. Catal.*, vol. 274, no. 2, pp. 200–206, Sep. 2010.

[42] M. A. Natal-Santiago, S. G. Podkolzin, R. D. Cortright, and J. A. Dumesic, "Microcalorimetric studies of interactions of ethene, isobutene, and isobutane with silica-supported Pd, Pt, and PtSn," *Catal. Letters*, vol. 45, no. 3/4, pp. 155–163, 1997.

[43] R. D. Cortright and J. A. Dumesic, "Microcalorimetric, Spectroscopic, and Kinetic Studies of Silica Supported Pt and Pt/Sn Catalysts for Isobutane Dehydrogenation," *J. Catal.*, vol. 148, no. 2, pp. 771–778, Aug. 1994.

[44] M. L. Yang, Y. A. Zhu, X. G. Zhou, Z. J. Sui, and D. Chen, "First-principles calculations of propane dehydrogenation over PtSn catalysts," *ACS Catal.*, vol. 2, no. 6, pp. 1247–1258, 2012.

[45] L. Nykänen and K. Honkala, "Density functional theory study on propane and propene adsorption on Pt(111) and PtSn alloy surfaces," *J. Phys. Chem. C*, vol. 115, no. 19, pp. 9578–9586, 2011.

[46] L. Nykänen and K. Honkala, "Selectivity in Propene Dehydrogenation on Pt and Pt 3 Sn Surfaces from First Principles," *ACS Catal.*, vol. 3, no. 12, pp. 3026–3030, Dec. 2013.

[47] P. Biloen, F. M. Dautzenberg, and W. M. H. Sachtler, "Catalytic dehydrogenation of propane to propene over platinum and platinum-gold alloys," *J. Catal.*, vol. 50, no. 1, pp. 77–86, Oct. 1977.

[48] D. J. Childers, N. M. Schweitzer, S. M. K. Shahari, R. M. Rioux, J. T. Miller, and R. J. Meyer, "Modifying structure-sensitive reactions by addition of Zn to Pd," *J. Catal.*, vol. 318, pp. 75–84, Oct. 2014.

[49] B. K. Vu, M. B. Song, I. Y. Ahn, Y.-W. Suh, D. J. Suh, W.-I. Kim, H.-L. Koh, Y. G.

Choi, and E. W. Shin, “Pt–Sn alloy phases and coke mobility over Pt–Sn/Al2O3 and Pt–Sn/ZnAl2O4 catalysts for propane dehydrogenation,” *Appl. Catal. A Gen.*, vol. 400, no. 1–2, pp. 25–33, Jun. 2011.

[50] H. Okamoto, “In-Pt (Indium-Platinum),” *J. Phase Equilibria Diffus.*, vol. 26, no. 4, pp. 399–399, 2005.

[51] L. Deng, T. Shishido, K. Teramura, and T. Tanaka, “Effect of reduction method on the activity of Pt-Sn/SiO2for dehydrogenation of propane,” *Catal. Today*, vol. 232, pp. 33–39, 2014.

[52] H. Abe, F. Matsumoto, L. R. Alden, S. C. Warren, H. D. Abruña, and F. J. DiSalvo, “Electrocatalytic Performance of Fuel Oxidation by Pt 3 Ti Nanoparticles,” *J. Am. Chem. Soc.*, vol. 130, no. 16, pp. 5452–5458, Apr. 2008.

[53] T. Ghosh, B. M. Leonard, Q. Zhou, and F. J. DiSalvo, “Pt Alloy and Intermetallic Phases with V, Cr, Mn, Ni, and Cu: Synthesis As Nanomaterials and Possible Applications As Fuel Cell Catalysts,” *Chem. Mater.*, vol. 22, no. 7, pp. 2190–2202, Apr. 2010.

[54] Z. Cui, H. Chen, M. Zhao, D. Marshall, Y. Yu, H. Abruña, and F. J. DiSalvo, “Synthesis of Structurally Ordered Pt 3 Ti and Pt 3 V Nanoparticles as Methanol Oxidation Catalysts,” *J. Am. Chem. Soc.*, vol. 136, no. 29, pp. 10206–10209, Jul. 2014.

[55] B. S. Mun, M. Watanabe, M. Rossi, V. Stamenkovic, N. M. Markovic, and P. N. Ross, “A study of electronic structures of Pt3M (M=Ti,V,Cr,Fe,Co,Ni) polycrystalline alloys with valence-band photoemission spectroscopy,” *J. Chem. Phys.*, vol. 123, no. 20, p. 204717, Nov. 2005.

[56] R. M. Waterstrat, “The vanadium-platinum constitution diagram,” *Metall. Trans.*, vol. 4, no. 2, pp. 455–466, Feb. 1973.

[57] H. Okamoto, “Pt-V (Platinum-Vanadium),” *J. Phase Equilibria Diffus.*, vol. 30, no. 6, pp. 666–667, 2009.

[58] B. M. Weckhuysen and D. E. Keller, “Chemistry, spectroscopy and the role of supported vanadium oxides in heterogeneous catalysis,” *Catal. Today*, vol. 78, no. 1–4, pp. 25–46, Feb. 2003.

[59] C. A. Schneider, W. S. Rasband, and K. W. Eliceiri, “NIH Image to ImageJ: 25 years of image analysis,” *Nat. Methods*, vol. 9, no. 7, pp. 671–675, Jul. 2012.

[60] J. Benson and M. Boudart, “Hydrogen-Oxygen Titration Method for the Measurement Areas of Supported,” *J. Catal.*, vol. 4, pp. 704–710, 1965.

[61] T. B. Bolin, T. Wu, N. Schweitzer, R. Lobo-Lapidus, A. J. Kropf, H. Wang, Y. Hu, J. T. Miller, and S. M. Heald, “In situ intermediate-energy X-ray catalysis research at the advanced photon source beamline 9-BM,” *Catal. Today*, vol. 205, pp. 141–147, Apr. 2013.

[62] B. Ravel, A. J. Kropf, D. Yang, M. Wang, M. Topsakal, D. Lu, M. C. Stennett, and N. C. Hyatt, "Nonresonant valence-to-core x-ray emission spectroscopy of niobium," *Phys. Rev. B*, vol. 97, no. 12, pp. 1–7, 2018.

[63] A. P. Hammersley, "FIT2D: An Introduction and Overview," 1997.

[64] A. P. Hammersley, S. O. Svensson, M. Hanfland, A. N. Fitch, and D. Hausermann, "Two-dimensional detector software: From real detector to idealised image or two-theta scan," *High Press. Res.*, vol. 14, no. 4–6, pp. 235–248, 1996.

[65] L. Lutterotti, "Total pattern fitting for the combined size-strain-stress-texture determination in thin film diffraction," *Nucl. Instruments Methods Phys. Res. Sect. B Beam Interact. with Mater. Atoms*, vol. 268, no. 3–4, pp. 334–340, 2010.

[66] G. Kresse and J. Furthmüller, "Efficiency of ab-initio total energy calculations for metals and semiconductors using a plane-wave basis set," *Comput. Mater. Sci.*, vol. 6, no. 1, pp. 15–50, Jul. 1996.

[67] G. Kresse and J. Furthmüller, "Efficient iterative schemes for ab initio total-energy calculations using a plane-wave basis set," *Phys. Rev. B*, vol. 54, no. 16, pp. 11169–11186, Oct. 1996.

[68] G. Kresse and J. Hafner, "Ab initio molecular dynamics for liquid metals," *Phys. Rev. B*, vol. 47, no. 1, pp. 558–561, Jan. 1993.

[69] G. Kresse and J. Hafner, "Ab initio molecular-dynamics simulation of the liquid-metal–amorphous-semiconductor transition in germanium," *Phys. Rev. B*, vol. 49, no. 20, pp. 14251–14269, May 1994.

[70] J. P. Perdew, K. Burke, and M. Ernzerhof, "Generalized Gradient Approximation Made Simple," *Phys. Rev. Lett.*, vol. 77, no. 18, pp. 3865–3868, Oct. 1996.

[71] P. E. Blöchl, "Projector augmented-wave method," *Phys. Rev. B*, vol. 50, no. 24, pp. 17953–17979, Dec. 1994.

[72] H. J. Monkhorst and J. D. Pack, "Special points for Brillouin-zone integrations," *Phys. Rev. B*, vol. 13, no. 12, pp. 5188–5192, Jun. 1976.

[73] M. Methfessel and A. T. Paxton, "High-precision sampling for Brillouin-zone integration in metals," *Phys. Rev. B*, vol. 40, no. 6, pp. 3616–3621, Aug. 1989.

[74] G. Henkelman, B. P. Uberuaga, and H. Jónsson, "A climbing image nudged elastic band method for finding saddle points and minimum energy paths," *J. Chem. Phys.*, vol. 113, no. 22, pp. 9901–9904, Dec. 2000.

[75] A. Larsen, M. Jens, B. Jakob, C. Ivano, C. Rune, D. Marcin, F. Jesper, G. Michael, H. Bjork, and H. Cory, "The Atomic Simulation Environment - A Python library for working with atoms," *J. Phys. Condens. Matter*, vol. 29, p. 27, 2017.

[76] A. Stukowski, “Visualization and analysis of atomistic simulation data with OVITO-the Open Visualization Tool,” *Model. Simul. Mater. Sci. Eng.*, vol. 18, no. 1, 2010.

[77] S. B. Simonsen, I. Chorkendorff, S. Dahl, M. Skoglundh, J. Sehested, and S. Helveg, “Direct Observations of Oxygen-induced Platinum Nanoparticle Ripening Studied by In Situ TEM RID C-7282-2008 RID A-4898-2011,” *J. Am. Chem. Soc.*, vol. 132, no. 23, pp. 7968–7975, 2010.

[78] J. T. Miller, A. J. Kropf, Y. Zha, J. R. Regalbuto, L. Delannoy, C. Louis, E. Bus, and J. A. van Bokhoven, “The effect of gold particle size on AuAu bond length and reactivity toward oxygen in supported catalysts,” *J. Catal.*, vol. 240, no. 2, pp. 222–234, Jun. 2006.

[79] E. Bus and J. A. Van Bokhoven, “Electronic and geometric structures of supported platinum, gold, and platinum-gold catalysts,” *J. Phys. Chem. C*, vol. 111, no. 27, pp. 9761–9768, 2007.

[80] J. R. Gallagher, T. Li, H. Zhao, J. Liu, Y. Lei, X. Zhang, Y. Ren, J. W. Elam, R. J. Meyer, R. E. Winans, and J. T. Miller, “In situ diffraction of highly dispersed supported platinum nanoparticles,” *Catal. Sci. Technol.*, vol. 4, no. 9, pp. 3053–3063, 2014.

[81] I. N. Leontyev, A. B. Kuriganova, N. G. Leontyev, L. Hennet, A. Rakhmatullin, N. V Smirnova, and V. Dmitriev, “Size dependence of the lattice parameters of carbon supported platinum nanoparticles: X-ray diffraction analysis and theoretical considerations,” *RSC Adv.*, vol. 4, no. 68, pp. 35959–35965, 2014.

[82] J. Miller, M. Schreier, A. J. Kropf, and J. R. Regalbuto, “A fundamental study of platinum tetraammine impregnation of silica2. The effect of method of preparation, loading, and calcination temperature on (reduced) particle size,” *J. Catal.*, vol. 225, no. 1, pp. 203–212, Jul. 2004.

[83] B. Olthof, A. Khodakov, A. T. Bell, and E. Iglesia, “Effects of Support Composition and Pretreatment Conditions on the Structure of Vanadia Dispersed on \ce{SiO2}, \ce{Al2O3}, \ce{TiO2}, \ce{ZrO2}, and \ce{HfO2},” *J. Phys. Chem. B*, vol. 104, no. 7, pp. 1516–1528, 2000.

[84] K. D. Sabnis, M. C. Akatay, Y. Cui, F. G. Sollberger, E. A. Stach, J. T. Miller, W. N. Delgass, and F. H. Ribeiro, “Probing the active sites for water-gas shift over Pt/molybdenum carbide using multi-walled carbon nanotubes,” *J. Catal.*, vol. 330, pp. 442–451, 2015.

[85] A. L. Ankudinov, J. J. Rehr, J. J. Low, and S. R. Bare, “Sensitivity of Pt x-ray absorption near edge structure to the morphology of small Pt clusters,” *J. Chem. Phys.*, vol. 116, no. 5, pp. 1911–1919, 2002.

[86] Y. Lei, J. Jelic, L. C. Nitsche, R. Meyer, and J. Miller, “Effect of particle size and adsorbates on the L3, L2 and L1 X-ray absorption near edge structure of supported Pt nanoparticles,” *Top. Catal.*, vol. 54, no. 5–7, pp. 334–348, 2011.

[87] J. F. Moulder, W. F. Stickle, P. E. Sobol, and K. D. Bomben, *Handbook of X-ray Photoelectron Spectroscopy*. Eden Prairie, MN: Physical Electronics, Inc., 1995.

[88] F. H. Ribeiro, A. E. Schach Von Wittenau, C. H. Bartholomew, and G. A. Somorjai, "Reproducibility of Turnover Rates in Heterogeneous Metal Catalysis: Compilation of Data and Guidelines for Data Analysis," *Catal. Rev.*, vol. 39, no. 1–2, pp. 49–76, Feb. 1997.

[89] C. P. Wang, A. Q. Zheng, and X. J. Liu, "Thermodynamic assessments of the V-Ge and V-Pt systems," *Intermetallics*, vol. 16, no. 4, pp. 544–549, 2008.

[90] N. J. LiBretto, C. Yang, Y. Ren, G. Zhang, and J. T. Miller, "Identification of Surface Structures in Pt3Cr Intermetallic Nanocatalysts," *Chem. Mater.*, p. acs.chemmater.8b04774, 2019.

[91] I. E. Wachs and B. M. Weckhuysen, "Structure and reactivity of surface vanadium oxide species on oxide supports," *Appl. Catal. A Gen.*, vol. 157, no. 1–2, pp. 67–90, 1997.

[92] M. C. Román-Martínez, J. A. Maciá-Agulló, I. M. J. Vilella, D. Cazorla-Amorós, and H. Yamashita, "State of Pt in dried and reduced PtIn and PtSn catalysts supported on carbon," *J. Phys. Chem. C*, vol. 111, no. 12, pp. 4710–4716, 2007.

[93] J. M. Ramallo-López, G. F. Santori, L. Giovanetti, M. L. Casella, O. a. Ferretti, and F. G. Requejo, "XPS and XAFS Pt L 2,3 -Edge Studies of Dispersed Metallic Pt and PtSn Clusters on SiO 2 Obtained by Organometallic Synthesis: Structural and Electronic Characteristics," *J. Phys. Chem. B*, vol. 107, no. 41, pp. 11441–11451, Oct. 2003.

[94] J. K. Nørskov, "Covalent effects in the effective-medium theory of chemical binding: Hydrogen heats of solution in the 3d metals," *Phys. Rev. B*, vol. 26, no. 6, pp. 2875–2885, Sep. 1982.

[95] N. F. Mott and H. Jones, *The Theory of the Properties of Metals and Alloys*. Oxford at the Clarendon Press, 1936.

[96] E. A. Stern, "Rigid-Band Model of Alloys," *Phys. Rev.*, vol. 157, no. 3, pp. 544–551, May 1967.

[97] F. Behafarid, L. K. Ono, S. Mostafa, J. R. Croy, G. Shafai, S. Hong, T. S. Rahman, S. R. Bare, and B. Roldan Cuenya, "Electronic properties and charge transfer phenomena in Pt nanoparticles on γ-Al2O3: size, shape, support, and adsorbate effects," *Phys. Chem. Chem. Phys.*, vol. 14, no. 33, p. 11766, 2012.

[98] M. G. Mason, "Electronic structure of supported small metal clusters," *Phys. Rev. B*, vol. 27, no. 2, pp. 748–762, Jan. 1983.

[99] U. Gelius, "Binding energies and chemical shifts in ESCA," *Phys. Scr.*, vol. 9, no. 3, pp. 133–147, 1974.

[100] A. N. Mansour, J. W. Cook, and D. E. Sayers, “Quantitative technique for the determination of the number of unoccupied d-electron states in a platinum catalyst using the L2,3 x-ray absorption edge spectra,” *J. Phys. Chem.*, vol. 88, no. 11, pp. 2330–2334, 1984.

[101] D. E. Ramaker, B. L. Mojet, M. T. Garriga Oostenbrink, J. T. Miller, and D. C. Koningsberger, “Contribution of shape resonance and Pt–H EXAFS in the Pt L2,3 X-ray absorption edges of supported Pt particles: Application and consequences for catalyst characterization,” *Phys. Chem. Chem. Phys.*, vol. 1, no. 9, pp. 2293–2302, 1999.

[102] C. Goyhenex and G. Tréglia, “Unified picture of d -band and core-level shifts in transition metal alloys,” *Phys. Rev. B*, vol. 83, no. 7, p. 075101, 2011.

[103] I. A. Abrikosov, W. Olovsson, and B. Johansson, “Valence-band hybridization and core level shifts in random ag-pd alloys,” *Phys. Rev. Lett.*, vol. 87, no. 17, pp. 2–5, 2001.

[104] M. Weinert and R. E. Watson, “Core-level shifts in bulk alloys and surface adlayers,” *Phys. Rev. B*, vol. 51, no. 23, pp. 17168–17180, 1995.

[105] W. Olovsson, C. Göransson, L. V. Pourovskii, B. Johansson, and I. A. Abrikosov, “Core-level shifts in fcc random alloys: A first-principles approach,” *Phys. Rev. B - Condens. Matter Mater. Phys.*, vol. 72, no. 6, pp. 1–12, 2005.

[106] Y. S. Lee, K. Y. Lim, Y. D. Chung, C. N. Whang, and Y. Jeon, “XPS core-level shifts and XANES studies of Cu-Pt and Co-Pt alloys,” *Surf. Interface Anal.*, vol. 30, no. 1, pp. 475–478, 2000.

[107] D. Wang, X. Cui, Q. Xiao, Y. Hu, Z. Wang, Y. M. Yiu, and T. K. Sham, “Electronic behaviour of Au-Pt alloys and the 4f binding energy shift anomaly in Au bimetallics- X-ray spectroscopy studies,” *AIP Adv.*, vol. 8, no. 6, 2018.

[108] S. L. Yohe, H. J. Choudhari, D. D. Mehta, P. J. Dietrich, M. D. Detwiler, C. M. Akatay, E. A. Stach, J. T. Miller, W. N. Delgass, R. Agrawal, and F. H. Ribeiro, “High-pressure vapor-phase hydrodeoxygenation of lignin-derived oxygenates to hydrocarbons by a PtMo bimetallic catalyst: Product selectivity, reaction pathway, and structural characterization,” *J. Catal.*, vol. 344, pp. 535–552, 2016.

[109] G. A. Martin, “The kinetics of the catalytic hydrogenolysis of ethane over Ni/SiO2,” *J. Catal.*, vol. 60, no. 3, pp. 345–355, 1979.

[110] S. A. Goddard, M. D. Amiridis, J. E. Rekoske, N. Cardona-Martinez, and J. A. Dumesic, “Kinetic simulation of heterogeneous catalytic processes: Ethane hydrogenolysis over supported group VIII metals,” *J. Catal.*, vol. 117, no. 1, pp. 155–169, 1989.

[111] A. Almithn and D. Hibbitts, “Effects of Catalyst Model and High Adsorbate Coverages in ab initio Studies of Alkane Hydrogenolysis,” *ACS Catal.*, vol. 8, pp. 6375–6387, 2018.

[112] J. H. Sinfelt, “Specificity in Catalytic Hydrogenolysis by Metals,” *Adv. Catal.*, vol. 23, pp.

91–119, 1973.

[113] A. Hook, J. D. Massa, and F. E. Celik, “Effect of Tin Coverage on Selectivity for Ethane Dehydrogenation over Platinum-Tin Alloys,” *J. Phys. Chem. C*, vol. 120, no. 48, pp. 27307–27318, 2016.

[114] Z. Wu, B. C. Bukowski, Z. Li, C. Milligan, L. Zhou, T. Ma, Y. Wu, Y. Ren, F. H. Ribeiro, W. N. Delgass, J. P. Greeley, G. Zhang, J. T. Miller, Z. Wu, B. C. Bukowski, Z. Li, C. Milligan, L. Zhou, T. Ma, and Y. Wu, “Changes in Catalytic and Adsorptive Properties of 2 nm Pt3Mn Nanoparticles by Subsurface Atoms,” *J. Am. Chem. Soc.*, 2018.

[115] X. Huang, A. J. Shumski, X. Zhang, and C. W. Li, “Systematic Control of Redox Properties and Oxygen Reduction Reactivity through Colloidal Ligand-Exchange Deposition of Pd on Au,” *J. Am. Chem. Soc.*, vol. 140, no. 28, pp. 8918–8923, 2018.

[116] H. H. Hwu, J. Eng, and J. G. Chen, “Ni/Pt(111) bimetallic surfaces: Unique chemistry at monolayer Ni coverage,” *J. Am. Chem. Soc.*, vol. 124, no. 4, pp. 702–709, 2002.

[117] J. N. Armor, “Emerging importance of shale gas to both the energy & chemicals landscape,” *J. Energy Chem.*, vol. 22, no. 1, pp. 21–26, 2013.

[118] J. J. Siirola, “The impact of shale gas in the chemical industry,” *AIChE J.*, vol. 60, no. 3, pp. 810–819, Mar. 2014.

[119] B. V. Vora, “Development of dehydrogenation catalysts and processes,” *Top. Catal.*, vol. 55, no. 19–20, pp. 1297–1308, 2012.

[120] J. H. Sinfelt, “Catalytic hydrogenolysis on metals,” *Catal. Letters*, vol. 9, no. 3–4, pp. 159–171, 1991.

[121] R. D. Cortright, S. A. Goddard, J. E. Rekoske, and J. A. Dumesic, “Kinetic study of ethylene hydrogenation,” *J. Catal.*, vol. 127, no. 1, pp. 342–353, 1991.

[122] S. Furukawa and T. Komatsu, “Intermetallic Compounds: Promising Inorganic Materials for Well-Structured and Electronically Modified Reaction Environments for Efficient Catalysis,” *ACS Catal.*, vol. 7, no. 1, pp. 735–765, 2017.

[123] J. Singh, R. C. Nelson, B. C. Vicente, S. L. Scott, and J. A. van Bokhoven, “Electronic structure of alumina-supported monometallic Pt and bimetallic PtSn catalysts under hydrogen and carbon monoxide environment,” *Phys. Chem. Chem. Phys.*, vol. 12, no. 21, p. 5668, 2010.

[124] A. Elsen, U. Jung, F. Vila, Y. Li, O. V. Safonova, R. Thomas, M. Tromp, J. J. Rehr, R. G. Nuzzo, and A. I. Frenkel, “Intracluster Atomic and Electronic Structural Heterogeneities in Supported Nanoscale Metal Catalysts,” *J. Phys. Chem. C*, vol. 119, no. 45, pp. 25615–25627, 2015.

[125] Y. Chen and D. G. Vlachos, “Hydrogenation of Ethylene and Dehydrogenation and

Hydrogenolysis of Ethane on Pt(111) and Pt(211): A Density Functional Theory Study," *J. Phys. Chem. C*, vol. 114, no. 11, pp. 4973–4982, Mar. 2010.

[126] A. M. Goda, M. A. Barteau, and J. G. Chen, "Correlating electronic properties of bimetallic surfaces with reaction pathways of C2 hydrocarbons," *J. Phys. Chem. B*, vol. 110, no. 24, pp. 11823–11831, 2006.

[127] A. Hook and F. E. Celik, "Predicting Selectivity for Ethane Dehydrogenation and Coke Formation Pathways over Model Pt-M Surface Alloys with ab Initio and Scaling Methods," *J. Phys. Chem. C*, vol. 121, no. 33, pp. 17882–17892, 2017.

[128] S. Zha, G. Sun, T. Wu, J. Zhao, Z. J. Zhao, and J. Gong, "Identification of Pt-based catalysts for propane dehydrogenation: Via a probability analysis," *Chem. Sci.*, vol. 9, no. 16, pp. 3925–3931, 2018.

[129] C. Yang, Z. Wu, G. Zhang, H. Sheng, J. Tian, Z. Duan, H. Sohn, A. J. Kropf, T. Wu, T. R. Krause, and J. T. Miller, "Promotion of Pd nanoparticles by Fe and formation of a Pd 3 Fe intermetallic alloy for propane dehydrogenation," *Catal. Today*, no. January, pp. 1–6, 2018.

[130] M.-L. Yang, Y.-A. Zhu, C. Fan, Z.-J. Sui, D. Chen, and X.-G. Zhou, "DFT study of propane dehydrogenation on Pt catalyst: effects of step sites," *Phys. Chem. Chem. Phys.*, vol. 13, no. 8, p. 3257, 2011.

[131] L. Nykänen and K. Honkala, "Selectivity in propene dehydrogenation on Pt and Pt3Sn surfaces from first principles," *ACS Catal.*, vol. 3, no. 12, pp. 3026–3030, 2013.

[132] O. Levenspiel, *Chemical Reaction Engineering*, 3rd ed. New York: John Wiley & Sons, 1999.

[133] J. Schindelin, I. Arganda-Carreras, E. Frise, V. Kaynig, M. Longair, T. Pietzsch, S. Preibisch, C. Rueden, S. Saalfeld, B. Schmid, J. Tinevez, D. J. White, V. Hartenstein, K. Eliceiri, P. Tomancak, and A. Cardona, "Fiji: an open-source platform for biological-image analysis," *Nat. Methods*, vol. 9, no. 7, pp. 676–682, Jul. 2012.

[134] J. P. Perdew, K. Burke, and M. Ernzerhof, "Generalized Gradient Approximation Made Simple [Phys. Rev. Lett. 77, 3865 (1996)]," *Phys. Rev. Lett.*, vol. 78, no. 7, pp. 1396–1396, 1996.

[135] D. Sheppard, R. Terrell, and G. Henkelman, "Optimization methods for finding minimum energy paths," *J. Chem. Phys.*, vol. 128, no. 13, pp. 1–10, 2008.

[136] J. Boes, "CatKit." .

[137] H. Nowotny and H. Bittner, "Die Kristallstruktur von PdZn," *Monatshefte fuer Chemie*, vol. 81, no. 5, pp. 679–680, 1950.

[138] M. Krajčí and J. Hafner, "Semihydrogenation of acetylene on the (010) surface of GaPd2:

Ga enrichment improves selectivity," *J. Phys. Chem. C*, vol. 118, no. 23, pp. 12285–12301, 2014.

[139] S. Saerens, M. K. Sabbe, V. V. Galvita, E. A. Redekop, M. F. Reyniers, and G. B. Marin, "The Positive Role of Hydrogen on the Dehydrogenation of Propane on Pt(111)," *ACS Catal.*, vol. 7, no. 11, pp. 7495–7508, 2017.

[140] A. Ota, E. L. Kunkes, I. Kasatkin, E. Groppo, D. Ferri, B. Poceiro, R. M. Navarro Yerga, and M. Behrens, "Comparative study of hydrotalcite-derived supported Pd 2Ga and PdZn intermetallic nanoparticles as methanol synthesis and methanol steam reforming catalysts," *J. Catal.*, vol. 293, pp. 27–38, 2012.

[141] J. Zhu Chen, Z. Wu, X. Zhang, S. Choi, Y. Xiao, A. Varma, W. Liu, G. Zhang, and J. T. Miller, "Identification of the structure of the Bi promoted Pt non-oxidative coupling of methane catalyst: a nanoscale Pt 3 Bi intermetallic alloy," *Catal. Sci. Technol.*, 2019.

[142] C. Ye, Z. Wu, W. Liu, Y. Ren, G. Zhang, and J. T. Miller, "Structure Determination of a Surface Tetragonal Pt 1 Sb 1 Phase on Pt Nanoparticles," *Chem. Mater.*, vol. 30, no. 14, pp. 4503–4507, Jul. 2018.

[143] R. D. Cortright, R. M. Watwe, B. E. Spiewak, and J. A. Dumesic, "Kinetics of ethane hydrogenolysis over supported platinum catalysts," *Catal. Today*, vol. 53, no. 3, pp. 395–406, 1999.

[144] A. Almithn and D. Hibbitts, "Comparing Rate and Mechanism of Ethane Hydrogenolysis on Transition-Metal Catalysts," *J. Phys. Chem. C*, p. acs.jpcc.8b11070, Feb. 2019.

[145] A. M. Goda, M. A. Barteau, and J. G. Chen, "Correlating electronic properties of bimetallic surfaces with reaction pathways of C2 hydrocarbons," *J. Phys. Chem. B*, vol. 110, no. 24, pp. 11823–11831, 2006.

[146] M. P. Latusek, B. P. Spigarelli, R. M. Heimerl, and J. H. Holles, "Correlation of H2heat of adsorption and ethylene hydrogenation activity for supported Re@Pd overlayer catalysts," *J. Catal.*, vol. 263, no. 2, pp. 306–314, 2009.

[147] J. K. Nørskov, T. Bligaard, J. Rossmeisl, and C. H. Christensen, "Towards the computational design of solid catalysts," *Nat. Chem.*, vol. 1, no. 1, pp. 37–46, 2009.

[148] T. Anniyev, H. Ogasawara, M. P. Ljungberg, K. T. Wikfeldt, J. B. MacNaughton, L.-Å. Näslund, U. Bergmann, S. Koh, P. Strasser, L. G. M. Pettersson, and A. Nilsson, "Complementarity between high-energy photoelectron and L-edge spectroscopy for probing the electronic structure of 5d transition metal catalysts," *Phys. Chem. Chem. Phys.*, vol. 12, no. 21, p. 5694, 2010.

[149] A. P. Hammersley, S. O. Svensson, M. Hanfland, A. N. Fitch, and D. Hausermann, "Two-dimensional detector software: From real detector to idealised image or two-theta scan," *High Press. Res.*, vol. 14, no. 4–6, pp. 235–248, 1996.

[150] S. Bhan and K. Schubert, “Zum Aufbau der Systeme Kobalt-Germanium, Rhodium-Silizium sowie einiger verwandter Legierungen,” *Zeitschrift fuer Met.*, vol. 51, pp. 327–339, 1960.

[151] S. C. Purdy, P. Ghanekar, G. Mitchell, A. J. Kropf, D. Y. Zemlyanov, Y. Ren, F. Ribeiro, W. N. Delgass, J. Greeley, and J. T. Miller, “The Origin of Electronic Modification of Platinum in a Pt3V Alloy and Their Consequences for Propane Dehydrogenation Catalysis,” *(submitted)*.

PUBLICATIONS

1. Purdy, Stephen C. Ghanekar, Pushkar, Mitchell, Garrett, Kropf, A. Jeremy, Zemlyanov, Dmitry Y., Ren, Yang, Ribeiro, Fabio, Delgass, W. Nicholas, Greeley, and Jeff, Miller, Jeffrey T., "The Role of Structure and the Origin of Electronic Modification of Platinum in a Pt_3V Alloy and Their Consequences for Propane Dehydrogenation Catalysis," (submitted)

2. Purdy, Stephen C., Seemakurthi, Ranga R., Vila-Vega, Juan Carlos, Mitchell Garrett M., Davidson, Mark, Lauderbach, Brooke, Wu, Zhenwei, Wegener, Evan, Wu, Tianpin, Gounder, Rajmani, Greeley, Jeff, and Miller, Jeffrey T. "Testing the predictive power of a dehydrogenation selectivity descriptor in palladium alloy catalysts with different structures" (in preparation)

3. Bukowski, Brandon, Purdy, Stephen C., Wegener, Evan, Wu, Zhenwei, Zhang, Guanghui, Miller, Jeffrey T., Greeley, "Insight into electronic structure of platinum alloys by resonant inelastic X-ray scattering" (in preparation)

4. Xie, Pengfei, Pu, Tiancheng, Nie, Anmin, Hwang, Sooyeon, Purdy, Stephen C., Yu, Wenjian, Su, Dong, Miller, Jeffrey T., and Wang, Chao, "Nanoceria-Supported Single-Atom Platinum Catalysts for Direct Methane Conversion," *ACS Catal.*, vol. 8, pp. 4044-4048, 2018.

5. Sun, Guodong, Zhao, Zhi-Jian, Mu, Rentao, Zha, Shenjun, Li, Lulu, Chen, Sai, Zang, Ketao, Luo, Jun, Li Zhenglong, Purdy, Stephen C., Kropf, A. Jeremy, Miller, Jeffrey T., Zeng, Liang and Gong, Jinlong, "Breaking the scaling relationship via thermally stable Pt/Cu single atom alloys for catalytic dehydrogenation," *Nat. Comms.*, vol. 9, no. 1, pp. 1-9.

6. Kunwar, Deepak, Zhou, Shulan, De La Riva, Andrew, Peterson, Eric, Xiong, Haifeng, Pereira Hernandez, Xavier Isidro, Purdy, Stephen C., ter Veen, Rik, Brongersma, Hidde H., Miller, Jeffrey T., Hashiguchi, Hiroki, Kovarik, Libor, Lin, Sen, Guo, Hua, Wang, Yong, and Datye, Abhaya "Stabilizing High Metal Loadings of Thermally Stable Platinum Single Atoms on an Industrial Catalyst Support," *ACS Catal.*, (accepted)